Redesign of a Hybrid Electric General Aviation Aircraft

A case study

T.C.W.M. Koopman
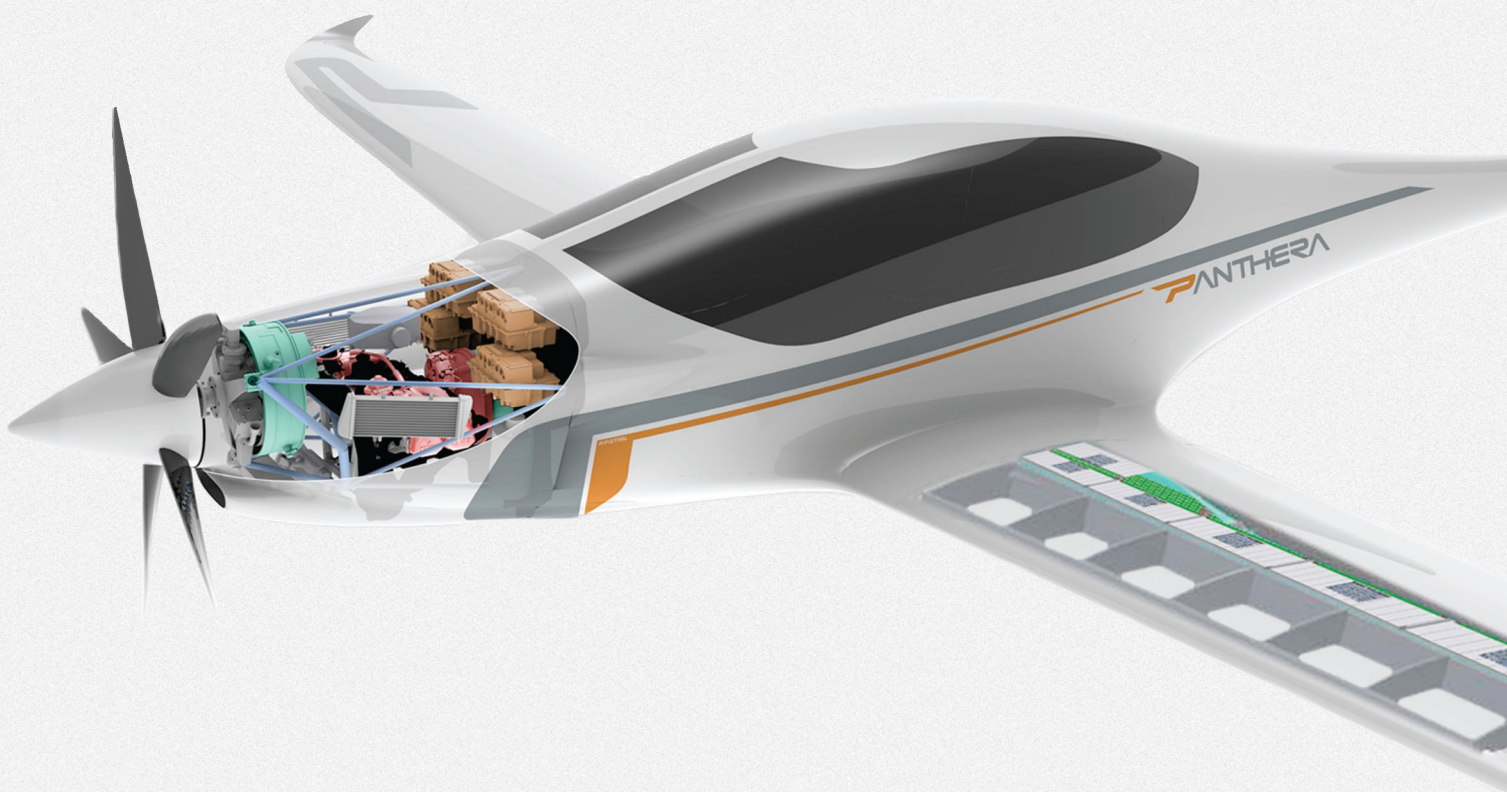
TUDelft

Redesign of a Hybrid Electric General Aviation Aircraft

A case study

by

T.C.W.M. Koopman

to obtain the degree of Master of Science
at the Delft University of Technology,
to be defended publicly on Thursday September 20, 2018 at 14:30.

Student number:	4017412	
Thesis committee:	Dr. F. Oliviero,	TU Delft, supervisor
	Prof. dr. ir. L.L.M. Veldhuis,	TU Delft
	Ir. H. Mulder,	TU Delft

An electronic version of this thesis is available at `http://repository.tudelft.nl/`.

TUDelft

Acknowledgments

In this report, the final research that I performed to complete the Aerospace Engineering at the Technical University of Delft is presented. I am very grateful to the people who supported me during this challenging time!

First of all, I would like to thank my supervisor, Fabrizio Oliviero. He supported and motivated me during the entire project and provided valuable feedback during the many meetings we had. Also, I would like to thank the exam committee, Leo Veldhuis and Hans Mulder, for their flexibility and time to assess my work. Moreover, I would like to thank Roelof Vos for his advice and critical view during my green light meeting.

I would like to thank Pipistrel for providing me useful performance data of the Panthera. Besides my thesis project I also got the opportunity to participate at a hackathon they organized in Slovenia, which I am very grateful for.

Next to these people, I want to thank the guys in room 1.05 for the laughter, support and motivation. Last but not least, I'd like to thank my brothers, parents, and friends for their support over the past years. Your support really made a difference!

<div style="text-align: right">

T.C.W.M. Koopman
Delft, September 2018

</div>

Abstract

The aviation sector and its associated activities contribute to climate change, damage to the environment, community noise, and local air pollution. As a consequence it affects the health and quality of life of citizens that live close to airports, and through climate change every person on earth. To reduce the impact of air travel and thereby accelerate growth, new technologies are being investigated. One area of research looks into the opportunities of using batteries and electric motors as additional energy source and power converter. Besides solving some of the current problems, these new technologies could enable radical new forms of aviation and create new business models such as on-demand personalized air travel.

Because the design rules of novel hybrid-electric aircraft differ significantly compared to that of conventional aircraft, new methods must be developed tailored for this new technology. Due to the additional variables introduced by using hybrid-electric propulsion systems, a simple sizing study quickly becomes a multi-disciplinary optimization problem. Furthermore, these new propulsion systems should not be benchmarked in an isolated way due to synergistic benefits with other disciplines. To close the gap between clean sheet designs and retrofits, it has been concluded that research focusing on feasible concepts in the near future is required.

The objective of this research is to define the implications of using hybrid electric propulsion systems in general aviation aircraft. The influence of design, operational and mission choices on optimal performance are identified through optimization studies. The design space includes the geometry of the main wing and the operational variables of the propulsion system. The performance is either measured in terms of fuel or total energy consumption per kilometer for design ranges between 50 and 1000 km.

To perform the quantitative analyses, a conceptual design framework has been developed. Models of all propulsion systems have been developed that simulate their performance. Every part of the tool is either verified with experimental data or has already been verified in literature. A quasi-three-dimensional aerodynamic solver has been modified to determine the aerodynamic characteristics with minimal computational time. The battery performance is modeled as function of time and rapidly sized such that the required power can be delivered by the smallest battery possible. A multi-disciplinary optimization approach has been used to integrate all modules and converge to an optimal design as quickly as possible.

First of all, a difference is found in terms of optimal configuration and operation of an aircraft when designed specifically for minimal fuel or for minimal total energy, leading to a maximum difference of 5% in terms of energy consumption. A trade-off between designing for aerodynamic efficiency versus the ability to carry batteries is part of the optimization routine. It has been shown that aircraft optimized for fuel consumption carry systematically more batteries compared to aircraft optimized for total energy consumption, always leading to a heavier aircraft with larger wings. Regardless of objective, the aerodynamic efficiency becomes more important for an increasing range while the ability to carry batteries decreases.

Three variables have been defined that determine the amount of hybridization in terms of power and energy without the need for constraint functions, as any combination of these variables lead an inherently feasible design: a climb coefficient that determines the rate of climb as a fraction of the maximum rate of climb, the fraction of the cruise that needs to be performed full electric, and a hybridization factor that determines the throttle of the internal combustion engine.

Given a certain required power at the power management system, there exist one specific throttle that leads to the maximum effective efficiency of the internal combustion engine. This throttle depends on the round trip efficiency of the battery charge-discharge cycle. When the internal combustion engine is scalable, the optimizer always makes sure that the most efficient throttle matches the power requirements during cruise, i.e. it avoids recharging.

The maximum possible range is highly determined by the required cruise velocity, given a fixed internal combustion engine. By scaling the internal combustion engine such that it is powerful enough to deliver the required power for cruise, the maximum range can be significantly increased. Furthermore, the optimal cruise altitude is found to be increasing with range and cruise velocity. At a cruise speed of 60 m/s the optimal cruise altitude coincides with the lower bound of 2 km whereas the optimal altitude at a cruise speed of 90 m/s increases from

2 km to 4 km for design ranges from 350 km to 700 km. In the latter case, the cruise altitude settles at 4 km for longer ranges.

The maximum range at which full electric cruise is possible is found to be the most efficient range in terms of energy consumption. This range increases linearly with the battery specific energy, providing designers a good initial estimation tool.

This research adds to the scientific body of knowledge as it presents a method that solves the multi-disciplinary optimization problem associated with the design of hybrid electric aircraft. Furthermore, through multiple optimization studies it provides insight in the influence of the design choices, operational choices, constraints, and mission profiles on the optimal performance of general aviation hybrid electric aircraft.

Contents

Nomenclature

Abbreviations

AAO	All-At-Once
AC	Alternating Current
AVL	Athena Vortex Lattice
BFGS	Broyden-Fletcher-Goldfarb-Shanno
CST	Class-Shape Transfer
DC	Direct Current
DSM	Design Structure Matrix
EM	Electric Motor
ESAR	Energy Specific Air Range
FD	Finite Difference
ICE	Internal Combustion Engine
IDF	Individual Discipline Feasible
IPCC	Intergovernmental Panel on Climate Change
KKT	Karush-Kuhn-Tucker
LE	Leading Edge
MDF	Multidisciplinary Feasible
PMAD	Power Management And Distribution
Q3D	Quasi Three Dimensional
Q3DM	Quasi Three Dimensional Module
QP	Quadratic Programming
SOC	State Of Charge
SQP	Sequential Quadratic Programming
UNFCCC	United Nations Climate Change secretary
VLM	Vortex Lattice Method

Greek symbols

α	Angle of attack
α	Constant
α	Step length
β	Constant
δ	Flap deflection angle
δ_T	Throttle of the internal combustion engine $\delta_T = \frac{P_{ICE}}{P_{ICE_{max}}}$
ϵ	Electrification $\epsilon = \frac{d_e}{R}$
η	Efficiency
η	Ratio of the drag of a finite cylinder to the drag of an infinite cylinder
Γ	Dihedral angle

κ_i	Interference factor
Λ	Sweep angle
λ	Lagrange multiplier
λ	Taper ratio
μ	Ground friction coefficient
ω	Rotational speed
ρ	Density

Latin symbols

$\Delta Y/c$	Leading edge sharpness parameter
a	Acceleration
AR	Aspect ratio
B	Magnetic field
b	Wing span
C	Chordlength
C	Constant
C	Continuity of a function
C_P	Power coefficient
C_T	Thrust coefficient
C_{climb}	Climb coefficient $C_{climb} = \frac{RoC}{RoC_{max}}$
c_{d_c}	Experimental steady state cross-flow drag coefficient of a circular cylinder
$C_{D_{L,fus}}$	Fuselage drag coefficient due to lift
C_{D_P}	Profile drag coefficient
C_D	Drag coefficient (3D)
C_d	Drag coefficient (2D)
C_f	Skin friction coefficient
C_{L_α}	Lift curve slope $C_{L_\alpha} = \frac{\partial C_L}{\partial \alpha}$
C_L	Lift coefficient (3D)
C_l	Lift coefficient (2D)
C_m	Pitching moment coefficient (2D)
D	Drag
d_e	Distance travelled full-electric
d_f	Fuselage equivalent maximum diameter
D_P	Propeller diameter
E	Energy
e^n	Amplification ratio
E_g	Gravimetric energy density . . . . Whr/kg
$ESAR$	Energy Specific Air Range . . . . kWh/km
F	Force

f	Fineness ratio	
f	Function	
g	Inequality constraint function	
H	Altitude	
h	Altitude	
h	Equality constraint function	
I	Current	
J	Advance ratio	
J	Current densit	
J	Objective	
K	Constant	
k	Constant	
K_Δ	Planform correction factor	
L	Auxiliary lagrangian function	
L	Lift	
l_f	Fuselage length	
M	Mach number	
m	Mass	
n	Rounds per minute	
n_{ult}	Ultimate loading factor	
P	Power	
p	Search direction	
P_g	Gravimetric power density	W/kg
Q	Battery capacity	
Q	Torque	
q	Charge	
q	Dynamic pressure	
R	Range	
R	Resistance	
Re	Reynolds number	
RoC	Rate of climb	
S	Surface area	
S_w	Wetted area	
$S_{plf_{fus}}$	Fuselage planform area	
S_{ref}	Reference surface area of the main wing	
S_{wet}	Wetted area	
S_{wf}	Flapped wing area	
SF	Shape factor	
T	Thrust	
t/c	Thickness to chord ratio	

U	Voltage
V	Velocity
V	Volume
v	Velocity
W	Weight
WS	Wing loading
x	Design variables
x	x-Coordinate
x/c	Normalized chordwise position
y	y-Coordinate
z	z-Coordinate

Subscripts

$c/4$	Quarter-chord
$conv$	Converter
des	Design
$e-cruise$	Full electric cruise phase
$elec$	Electrical
f	Flap
f	Fuselage
$fuselage$	Fuselage
FW	Fuel weight
g	Inequality constraint function
gen	Generator
h	Equality constraint function
$h-cruise$	Hybrid cruise phase
i	Index
i	Induced
k	Iteration
MAC	Mean aerodynamic chord
MTO	Maximum takeoff
OC	Open-Circuit
$prof$	Profile
r	Root
s	Structural
t	Tip
TO	Takeoff
W	Wing
w	Wing
$wing$	Main wing
x	Design variables

1

Introduction

The aviation sector brings without doubt significant economic and social benefits to society. However, the associated activities also contribute to climate change, damage to the environment, and noise and local air pollution. As a consequence it affects the health and quality of life of citizens that live close to airports, and through climate change it affects every person on earth. As the aviation sector is expected to grow tremendously due to upcoming economies, the effect it has on the environment will grow accordingly. To reduce the impact of air travel, new technologies are being investigated. One area of research looks into the opportunities of using batteries as additional energy source. Besides solving some of the problems introduced by current air travel, hybrid-electric aircraft could enable radical new forms of aviation and thereby create new business models.

This chapter is dedicated to presenting the framework of this thesis. First, the main problems related to current aviation, and the opportunities and threats of using hybrid electric technology will be elaborated. Furthermore, an overview of the existing research will be presented which will lead to a conclusion on the shortcomings, i.e. the gap in scientific literature that this thesis aims to fill. Subsequently the research objective, and the associated research questions are drawn up. This will be followed by a description of the research method. Lastly, an overview of the document structure of this thesis work will be given.

1.1. Background

Climate change is one of the driving forces behind innovation in the aviation industry. A substantial number of scientists believe that this change in climate is accelerating beyond what is naturally expected. One of the mechanisms that can change the climate is the so called greenhouse effect, which is the natural process that warms the Earth by absorbing and re-radiating the energy that is radiated by the Earth its surface. As a result of the emission of greenhouse gases, this effect is enhanced contributing to the warming of the earth. The impact of global warming could be so intense, that some governments treat it as a national security issue according to the United Nations Climate Change secretary (UNFCCC) [48]. Examples of greenhouse gases are water vapor, carbon dioxide (CO_2), and methane. To put in perspective: the Intergovernmental Panel on Climate Change (IPCC) [20] has estimated that aviation was responsible for around 3.5% of the anthropogenic climate change in 1992. This figure includes both CO_2 and non-CO_2 induced effects. It is estimated that the aviation its contribution could grow between 5%, and 15% in the worst case scenario, of the total contribution by 2050 if no action

is taken to reduce the emissions. In conclusion, a cleaner alternative is desired to reduce the negative impact of the sector while still growing.

Besides CO_2, the emission of nitrogen oxides (NO_x), volatile organic compounds (VOCs), carbon monoxide (CO), and particulate matter (PM) are usually considered as the most important contributers to local air quality concerns. Exposure to these emissions can result in serious health effects. Additionally, these emissions harm local ecosystems. Due to the increasing amount of residential development surrounding airports and the growth of air travel, local air quality has become a significant concern. Additionally, the emission of noise limits the growth of aviation. Especially near densely populated areas. By reducing air and noise pollution growth can be accelerated.

Thanks to companies such as UBER and Amazon, people are more than ever used to having everything on-demand. For the aviation sector, this leads to dreams about a new class of air traffic: on-demand personalized air travel. When realized, this could lead to an increased life radius, dramatically increasing the possibilities of everyday life [46]. In UBER's white-paper about on-demand urban air transportation a detailed description of the current market feasibility barriers is given. Next to a reduction in air and noise pollution, new technologies are required that increase the vehicle performance and reliability, affordability, and safety.

In combining conventional combustion engines with electric engines and batteries lie some great opportunities for the future of aviation. First of all, batteries do not emit any exhaust gases when converting its energy to power. Therefore, the local emissions can be reduced. When using renewable energy sources to generate the electric energy for the batteries, the total emissions can be reduced as well. Furthermore, the noise and vibrations from electric engines are virtually zero, reducing the noise pollution, increasing the cabin comfort, reducing the maintenance cost of the engines, and increasing the safety. Because the specific power of electric engines is much higher compared to internal combustion engines, revolutionary new designs can be achieved that were before unthinkable. As a result, new mission profiles and business cases can be investigated.

Unfortunately, hybrid-electric propulsion systems come with several downsides that form a potential risk for its success. The foremost downside is that the gravimetric energy density of batteries is in the order of 60 to 100 times lower compared to conventional fuel, leading to more required weight for energy storage. Practically, this puts serious limits on the range and takeoff weight of hybrid-electric aircraft. Even if the specific energy keeps growing with the historic 8% each year, it takes at least 50 years before it catches up with the energy density of fossil fuels. Furthermore, the acquisition-cost of batteries are relatively high, requiring new business models to justify the cost per aircraft.

Existing Literature

A lot of research has been performed on hybrid-electric aircraft. An extensive overview of this research has been made in a literature study prior to this current research thesis. Moore et al. from NASA experiences a lot of misconceptions regarding electric propulsion and suggests an attitude shift towards this novel technology: One should be mainly focusing on how (hybrid-) electric aircraft can compete with conventional propulsion, even though they are energy constrained, what new types of architectures it enables, and what evaluation metrics need to be used. Some researchers, such as Antcliff, Guynn, Marien, Wells, Schneider, and Tong [1], Pornet and Isikveren [36], and Perullo, Trawick, and Mavris [34] focus on the radically new clean sheet designs, generally based on rough assumptions and extrapolations of technology levels. To better understand the characteristics of hybrid-electric propulsion systems, some of the researchers are focussed more on retrofit designs. They study the detailed characteristics of each component and, for example, trying to find new control laws of the power

management unit. Examples are Friedrich and Robertson [15], Perullo and Mavris [33], Cinar, Mavris, Emeneth, Schneegans, Riediger, Fefermann, and Isikveren [4], and Pornet, Gologan, Vratny, Seitz, Schmitz, Isikveren, and Hornung [37]. The latter group concluded that the full potential of hybrid-electric propulsion cannot be predicted without doing a clean sheet design.

Shortcomings in Existing Knowledge

Because the design of novel hybrid-electric aircraft differ significantly from the design of conventional aircraft, new methods should be developed tailored for this new technology. Furthermore, it is not fair to compare the two propulsion systems in an isolated way due to the synergistic benefits of components in a hybrid-electric design and its fundamental differences. Therefore, it is concluded that new research should focus on concepts that are feasible in the near future, closing the gap between retrofits and clean sheet designs and providing valuable DNA for new ideas and design methods.

According to Raymer [38], a good conceptual design "seems to miraculously glide through subsequent evaluations by specialists without major changes being required". Besides meeting all the requirements, the proposed design resulting from the conceptual design phase should be best design in terms of the predefined objectives such as cost, fuel economy, weight, time to market, etc. For conventional aircraft, this process of conceptual design is fairly straightforward because the design rules have been fully developed over the past decades. A lot of data has been gathered over the years to build accurate empirical relations and the sizing rules are matured due to the sheer amount of experience with all components. For hybrid-electric aircraft, however, the translation from what the aircraft should do to how it will look like and how it will perform is not so clear. Due to the additional variables, such as the fraction of power that needs to be delivered by the batteries, a simple sizing study quickly becomes a multi-disciplinary optimization problem. Furthermore, the influence of the design constraints and different mission profiles on the optimal performance and the actual design is not fully understood yet.

1.2. Research Objective

The research presented in this document is an attempt to close the knowledge gap presented in Section 1.1. The importance of adding to the scientific body of knowledge has been stressed in this sections as well. As result of an extensive literature review, the research objective of this work has been formulated as follows;

> **Define the implications of using hybrid electric propulsion systems in general aviation aircraft, by performing optimization studies of such aircraft and identifying what design and mission changes lead to better performance.**

Aircraft design and mission requirements are inevitably tied together; Changes in the mission requirements will influence the optimal design. However, the magnitude of this mutual influence is not fully understood. On a more conceptual level, the implications of these new propulsion architectures on simulation and analysis architectures is not yet matured. To work systematically towards the objective of this thesis work, the research questions presented below have been drawn up.

1. What are the implications of using hybrid-electric propulsion systems in general aviation aircraft *on its design* when designing for optimal performance.

   (a) What is the influence of range on the optimal amount of batteries and size of the main wing?

   (b) What is the influence of objective on the optimal design?

(c) What is the influence of power control laws and recharge strategies on the performance and design?

2. What are the sensitivities regarding performance of hybrid-electric aircraft to changing:

(a) Cruise speed and altitude

(b) Battery technology level

3. What are the implications of using hybrid-electric propulsion systems in general aviation aircraft on the simulation and analysis architecture.

Since this work is focused on the general aviation market, from here onwards in this document when referring to aircraft, general aviation type of aircraft are implied. The road map on how to generate new knowledge through these questions, how to start and why, will be presented below.

Research Method

One of the conclusions from the literature study is that new research should be focused on feasible concepts in the near future. Because the development costs are much lower and the ease of certification higher with general aviation aircraft, this category is thought to be ideal for the first application of hybrid electric propulsion technologies. Therefore, this research will focus on general aviation aircraft. By generating and comparing various configurations designed for different objectives and requirements, the implications of hybrid-electric propulsion can be determined.

The Panthera, a test-bed aircraft used in a project focusing on a modular approach in hybrid-electric propulsion architectures, has been selected as reference aircraft. The fact that this aircraft is currently part of a research project contributes to the relevance of this thesis. Furthermore, the availability of essential performance data such as lift-drag polars, several component weights, the battery type, and the performance maps of the propeller, the electric motor, and the internal combustion engine is really useful for the verification and calibration of component models.

The use of computer simulations, i.e. running computer programs to model reality, have been chosen as research method to analyze various modifications of the baseline aircraft for the following reasons: the need for quantified data on the performance, the need to compare a multitude of different configurations, and — since one of the goals is to define implications for conceptual design— the fact that computer simulations are a integral part of conceptual design. As explained in Section 1.1, a relatively simple sizing study becomes a multi-disciplinary optimization problem due to the additional degrees of freedom introduced by hybrid-electric systems. Conceptual design programs make use of various discipline-analysis modules that are interconnected within the overall design routine. Part of this thesis work will be finding strategies on how the new discipline-analysis modules should be wired together to accelerate conceptual design programs.

One can generate the various configurations by manually determining the parameters of a new configuration, however, finding an optimal configuration this way quickly becomes impractical when trying to include many design variables. Simply because the design space is rapidly increases with every extra design variable that is included. For this reason, an automatic optimization routine needs to be used to find an optimal performing configuration within a feasible design space for each different study, e.g. different mission requirements etc.

Following Isikveren, Pornet, Vratny, and Schmidt [21], the energy consumption in relation to the traveled distance will be used as measure of performance. In this thesis the optimization objective is defined as the energy required to fly one kilometer during cruise. For each optimization, a certain design will be sought that minimizes this objective. Since this thesis is concerned with hybrid-electric aircraft, two different objectives are

used: one where only the fuel energy is taken into account, and another where the total energy is taken into account. When only taking fuel energy into account, the battery energy is basically considered to be *free*. It is expected that any design optimized for fuel consumption gives more priority to carrying batteries, since this does not add to the objective as would be the case when optimizing for total energy.

This research will focus on a limited amount of aspects of the aircraft. The first major area of interest is the redesign of the main wing its planform in terms of size and shape, because it enables changes in the maximum takeoff weight, and thereby changes in the propulsion systems. It has been found that the surface area, aspect ratio and taper ratio are the three most important variables to include in the optimizations. Secondly, the amount of batteries will be subject to change. By varying the battery capacity, the influence of hybridization in terms of energy can be investigated. Furthermore, the electric motor and internal combustion engine need to be rubberized, i.e. their performance models need to be scalable, to facilitate the comparison of different missions. The models that need to be developed mainly concerns aerodynamics, flight mechanics, propulsion and performance, and weight estimation. Major assumptions that have been made will be presented throughout the report.

As mentioned earlier, by comparing various configurations designed for different objectives and requirements, the implications of using hybrid-electric propulsion can be determined. Fuel consumption, range, and cruise speed are of utmost importance for potential customers when considering a new aircraft. Since the energy balance is significantly different for hybrid-electric aircraft, multiple ranges between 50 km and 1000 km will be investigated as part of each study. First, a study will be performed in which the two proposed objectives, i.e. minimal fuel or total energy, will be compared. This will be followed by a study that compares different power distribution strategies. Then, a study will be performed into the influence of cruise speed on the optimal design. Part of the intended result of this will be the ideal cruise altitude corresponding to each design cruise speed and range. Finally a study will be performed that investigates the influence of battery technology level on aircraft performance.

When all optimization studies have been performed, the sheer amount of data produced need to be processed. The most important parameters and differences will be quantified and analyzed, leading to insight regarding hybrid-electric aircraft. The translation from data to insight is done by reasoning about the causal relationship of the observed phenomena. Since all observations are based on te developed model, the *construct* of this research, it is of great importance that every module of it is validated. As final step, the insights will be generalized to another context as far as possible; e.g. different planforms, mission requirements, and propulsion system architectures and types.

1.3. Report Structure

Up till this very section the introduction, motivation, and objective of this research is provided. A detailed description of the methodology will be presented in Chapter 2. Part of the methodology is a description of the optimization and simulation approach, the aerodynamics, and all the propulsion systems. This will be followed by Chapter 3 in which the results of the optimization studies will be presented, accompanied by the observations of these results. The report ends in Chapter 4 with the conclusions drawn from this research and recommendations for further research.

2

Methodology

In this chapter, the methodology of this research will be presented. In Section 2.1 the optimization approach will be presented where the objectives will be formalized. Furthermore, the algorithm that will be used to solve the optimization problem will be presented together with implications on the simulation approach. Next, the the simulation approach will be discussed in Section 2.2. Here, an overview of all the modules will be presented including the way the modules will be connected and the reasoning behind this selection. Continuing in this chapter from Section 2.3 onwards, the theory and setup of the modules will be presented. Most attention will be given to the propulsion system models, then the flight and mission analysis followed by the aerodynamic models.

2.1. Optimization Approach

In the context of this research, optimization can be interpreted as finding an aircraft design that, for example, consumes the least amount of fuel while satisfying all mission and constraint requirements. There is much litera-ture available on the (mathematical) theory of optimization, different practical techniques to solve optimization problems, and surveys of the newest developments. Nocedal and Wright [32] for example, discusses the basis of various numerical optimization techniques and presents an extensive amount of fundamental mathematical theorems. More closely related to the design of multidisciplinary engineering systems, Martins and Lambe [25] presents a survey of multidisciplinary design optimization architectures. Both these resources have been used as reference for the optimization setup.

The general problem formulation consists of one objective function (Equation 2.1) and two sets of constraint functions (Equations 2.2 and 2.3). In this formulation, the linear bounds on the design variables have been included in the inequality constraint functions.

$$\min_{\mathbf{x}} f(\mathbf{x}) \tag{2.1}$$

$$\mathbf{g}(\mathbf{x}) \leqslant \mathbf{0} \tag{2.2}$$

$$\mathbf{h}(\mathbf{x}) = \mathbf{0} \tag{2.3}$$

The design vector ($\mathbf{x}$) consist of all the design variables. The selection of design variables and constraint functions are presented in Section 2.2, where the sub-modules and their interconnections are elaborated. All

the design variables are divided by the normalization factor to ensure a well-scaled problem.

The function f from the general problem formulation produces the objective value. In this research, the objective is the minimization of energy required to fly one kilometer of the specified range: the energy specific air range ($ESAR$) (Equation 2.4). When assuming that the battery energy comes from *clean* sources, it makes sense to optimize for fuel energy only ($ESAR_{fuel}$); Hence setting $\beta = 0$. However, as electrical energy is not *free*, it can be included in the objective function by setting β to a non-zero value. A total energy optimization ($ESAR_{total}$) corresponds with $\beta = 1$. The concept of optimizing energy, taking into account a scaling factor between the two sources, can be approached from a different angle as well. Say that the fuel (AVGAS) cost are around €2.22 per liter, then the energy cost is 0.25 €/kWh. In the European union, the average cost of electricity from the grid is around 0.22 €/kWh. Therefore, optimizing eq. 2.4 with $\beta \approx 1$ can also be interpreted as energy cost optimization. In this research, the fuel energy and total energy will be mainly the objective of the optimizations.

$$f(x) = ESAR(x) = \frac{E_{fuel}(x) + \beta \cdot E_{batt}(x)}{R} \tag{2.4}$$

2.1.1. The Search Towards and Optimum: Sequential Quadratic Programming

The search towards an optimum set of design variables is always iterative; The starting point is an initial guess of the optimal values in the design vector. Next, various intermediate sets of design variables are being produced until the solution is reached. The strategy used to move from one iteration to the next distinguishes one algoritm from another. All strategies, however different in approach, should perform well on three aspects:

- **Robustness**: It should perform well under a variety of conditions.
- **Efficiency**: It should not require to much computational time or storage.
- **Accuracy**: It should be able to produce the right results for all possible input.

Instead of building an optimization algorithm from scratch, it has been decided to use a matured and proven optimization algorithm. Within the programming environment used by the author (MATLAB), an optimization toolbox is available with various algorithms. It has been decided to use the sequential quadratic programming (SQP) method as solver algorithm. In Schittkowski [42], a comparison study has been performed in which SQP excelled in terms of execution time, number of function calls, number of gradient calls, and percentage of succesfull solutions.

In the case of an unconstrained optimization with one design variable, the condition for an local minimum is that the gradient must be zero. In constrained optimization, the meaning of this first-order optimality is more complex. The definition used in SQP is based on the Karush-Kuhn-Tucker (KKT) conditions, shown in Equations 2.6 till 2.8, which is a modification that enables first-order optimality for constrained problems. The auxiliary Lagrangian function required for this condition is shown in Equation 2.5.

$$\mathbf{L}(\mathbf{x}, \boldsymbol{\lambda}) = \mathbf{f}(\mathbf{x}) + \sum \boldsymbol{\lambda}_{g,i} \mathbf{g}_i(\mathbf{x}) + \sum \boldsymbol{\lambda}_{h,i} \mathbf{h}_i(\mathbf{x}) \tag{2.5}$$

$$\nabla_{\mathbf{x}} \mathbf{L}(\mathbf{x}, \boldsymbol{\lambda}) = 0 \tag{2.6}$$

$$\boldsymbol{\lambda}_{g,i} \mathbf{g}_i(\mathbf{x}) = 0 \qquad \forall i \tag{2.7}$$

$$\boldsymbol{\lambda}_{g,i} \geq 0 \tag{2.8}$$

The strategy used in the SQP method to move from one iteration to the next, is based on a quadratic programming (QP) subproblem. At each major iteration, the Hessian of the Lagrangian function is approximated using a quasi-Newton updating method following Broyden, Fletcher, Goldfarb and Shanno (*BFGS*). Additionally,

the Jacobian of the constraint functions is determined. This is then used to generate a QP subproblem whose solution is used to form a search direction, p_k in Equation 2.9, for a line search procedure. The search direction is determined such that a step-length α_k of 1 leads to the best improvement within the feasible QP subproblem. The step-length parameter α_k is chosen to be the largest value in the range between 0 and 1, such that there is maximum improvement in terms of a so-called merit function. This merit function determines the improvement of new points in terms of either the constraint of the objective function, unless the sub-problem is infeasible in which case only a reduction in the maximum constraint is tolerated.

$$x_{k+1} = x_k + \alpha_k p_k \tag{2.9}$$

The first evaluation in the line-search procedure uses the largest step-length possible, i.e. $\alpha_k = 1$. If the merit function at this new point shows improvement, the line search is finished and the new point is accepted as baseline for a new iteration in the SQP algorithm. However, if this new point does not show improvement, the analysis is repeated using smaller steps until acceptance of a design vector.

In the context of this thesis, it is important to understand the principles behind the *SQP* algorithm since it influences certain approaches to the optimization setup. To increase the acceptance rate of new points, it is important that the search direction —which is entirely based on the solution of the *QP*— is limited to the feasible region as much as possible. The latter can sometimes be achieved by using more constraint functions than strictly needed, so that the QP subproblem has more information regarding the feasible area. An example of when this is beneficial is when the maximum lift coefficient needs to be determined, as the optimizer can demarcate the feasible region best when it 'knows' where the maximum local lift coefficient is.

2.1.2. Termination Criteria: Optimality Measure and Step Size Tolerance

As important as knowing in which direction to go when optimizing an aircraft, is knowing when to stop. There are four criteria that control the termination of the optimizer. The first and foremost criteria is the so-called first order optimality and can be interpreted as the change in objective value from one iteration to another. It is formally defined as the maximum of the values calculated using Equations 2.10 and 2.11. The first order optimality threshold has been set to $2.5 \cdot 10^{-3}$. Furthermore, making changes in the order of squared nanometers is not so relevant when optimizing the wing surface area. For this reason, the smallest step size between iterations (Equation 2.12) is used as a criteria to define changes between two designs to be irrelevant. This threshold has been set to $5 \cdot 10^{-4}$. The last two are very straight forward, and meant as a last resort in case the optimization does not converge: the optimization should stop after a certain number of function calls, or after a number of iterations.

$$\|\nabla_{\mathbf{x}}\mathbf{L}(\mathbf{x}, \lambda)\| = \left\|\nabla\mathbf{f}(\mathbf{x}) + \sum \lambda_{\mathbf{g},i} \nabla\mathbf{g}_i(\mathbf{x}) + \sum \lambda_{\mathbf{h},i} \nabla\mathbf{h}_{\mathbf{h},i}(\mathbf{x})\right\| \tag{2.10}$$

$$\left\|\overrightarrow{\lambda_{\mathbf{g}}\mathbf{g}(\mathbf{x})}\right\| \tag{2.11}$$

$$\min\|x_i - x_{i+1}\| \tag{2.12}$$

Besides finding an optimum, the second responsibility of the optimizer is finding a feasible design. The measure for feasibility is defined as the largest magnitude of the constraint functions. If this is smaller than the constraint tolerance, the design returned by the optimizer is considered feasible. All optimizations throughout this thesis that returned infeasible points are discarded from the results.

2.1.3. Optimization Architectures: The Influence of Constraint Variables

Regardless of the configuration, an aircraft can only be accepted as an optimal solution if the feasibility constraints are satisfied. For example, the battery has enough capacity to deliver the required power at each moment during the mission. Or the aircraft mass used to calculate the drag corresponds with the actual aircraft mass, including batteries and fuel required for thrust generation. In other words, disciplines that are coupled need to match to each other. A fundamental distinction between optimization architectures can be made in terms of how the feasibility constraints are approached. In Martins and Lambe [25], the exact differences between all the state-of-the-art architectures are explained in detail. At the heart of their survey is the so-called all-at-once (AAO) approach. The simplifications made to the general problem determines the type of architecture.

By eliminating the discipline-analysis constraints from the problem, one obtains the so-called Individual Discipline Feasible (IDF) approach. As a result of this elimination, the discipline analysis equations are being solved exactly at each iteration, e.g. the vortex lattice equations which are solved inside AVL. Hereby, the problem size is substantially reduced. Furthermore, external software —such as aerodynamic solvers— can be used for the discipline analyses within the optimization problem without or with minimal modification to the existing analysis. However, the size of the problem can still be problematic.

To further reduce the size of the optimization problem, i.e. from the perspective of the optimizer, the consistency constraints can be removed from the problem. The resulting architecture is referred to as multidisciplinary feasible (MDF), also known as nested analysis and design. Within the function that is called by the optimizer, a multi-disciplinary analysis coordinator is placed that manages the consistency of all disciplines, arriving at a consistent design. Another benefit, besides the reduction of the problem size, is that every iteration a feasible design is returned by the optimizer. In a context where an early termination of the optimization occurs, for example when time is limited, this is particularly advantageous.

Feasible algorithms, such as MDF, are usually slower and more expensive than algorithms that allow the iterates to be infeasible, since they cannot follow shortcuts to the solution that cross infeasible territory. As a result, expensive functions calls are performed to converge to a feasible point in a region which is sub-optimal, within one function call of the optimizer. A mix between *IDF* and *MDF* has been implemented in the optimization setup of this thesis work.

2.1.4. Parallel Architecture

The total computational time per optimization is reduced by making the computation of the gradient work in parallel. By doing so, the maximum amount of computer power available in multi-core processors can be leveraged. If the number of cores exceeds the number of variables, this no longer holds. Therefore, when upscaling the proposed optimization to a high-performance cluster computer in for example the cloud, new distributed approaches need to be found.

2.1.5. Caching Results

Not all discipline analysis are influenced by all the design variables. For example, the aerodynamic analysis is a function of wing shape but does not depend on operation variables like electrification or rate of climb. Therefore, it would be a waste of computational resources if the aerodynamic characteristics are re-calculated every function call, even when the wing shape is not changed, during the optimization.

To solve this problem, a function has been developed by the author that caches the in- and output of these computationally heavy modules and distributes this on all external workers for the parallel computation of the gradient. Right after each function call made by the optimizer, the new design vector is compared with the stored

design vectors that are stored in the database. If a design vector can be found that shares the exact values of all variables that influence a certain discipline, e.g. surface area, aspect ratio, and taper ratio, the discipline analysis can be skipped and the results can be loaded from the cache. When the values of more than one entry in the new vector is different compared to previous vectors, it means that a line-search is performed that could form the basis of a new iteration. In the case of a potential new baseline, the design vector is stored together with the discipline analyses results.

2.2. Simulation Approach

One of conclusions that emerged from the literature study prior to this research is that there are a lot of different possibilities when it comes to modeling and optimizing aircraft performance. In this section, the rationale behind the choices that have been made during the research work regarding the interconnection of the submodels. First, the most important findings from the literature study on model choice will be discussed.

There are three main levels of optimization, according to Harmon, Frank, and Chattot [18]. The most general level, called *structural* optimization, is mainly concerned with the optimization of an aircraft its planform or the choice between various propulsion system architectures. Next is *parametric* optimization, which focuses on the sizing of given fixed discipline types. Lastly there is *control system optimization*, which, when applied to this research, would focus on the control laws of the propulsion systems, given a fixed aircraft configuration and propulsion systems in terms of type and size. Given the scope of this current research work, the proposed optimization lies between between structural and parametric optimization; For a given propulsion system architecture and aircraft planform type, an optimum is found between planform size, component sizes and operating points of components.

Once decided what aspects to include in the optimization, the appropriate modeling tools need to be selected. Based on the specific requirements of the overall modeling, the fidelity of the tools can be determined. Perullo and Mavris [33] set forth three different modeling types, each with their advantages and drawbacks. Mainly, the fidelity needs to be weighed against computational cost, ease of implementation, and suitability for radically new designs. To make a well-argued choice for the required type of models in the simulation, a brief overview of what currently has been done in literature will be presented. Most of this summary is based on a short literature survey given in Perullo and Mavris.

Bradley and Droney [2] performed a study on a hybrid-electric configuration using an electric motor attached to the shaft of a conventional turbofan engine. For their study they used detailed proprietary performance analysis tools. As part of their work, a set of performance estimation tools have been developed for the public domain. On of the disadvantages of using these tools, is the need for manual iterations between the aircraft and engine analysis making a proper optimization routine very difficult.

In Nam, Soban, and Mavris [31], the energy profiles are broken down into different mission segments, e.g. takeoff, climb and cruise, each with specific preconditions. Furthermore, the drivetrain is represented as a series of power conversion elements, where every element has constant efficiencies and specific weights and powers. Similarly, Harmon et al. [18] introduced the concept of different operating phases for which an optimiser determines what the best constant power demand will be per segment. Schoemann and Hornung [43] make use of efficiency performance maps to analyse the mission segments. However, since all of their methods use simple first-order equations —which cannot capture detailed effects on the lift-drag polar for example— to model the aircraft performance, it is merely useful as pre-sizing tools.

When assuming state-independent efficiencies of the propulsion systems, using segments with constant power and a predefined efficiency (as in Reynolds [39]) can work very well. However, since the battery usage in the past affects future performance, a more detailed flight analysis approach is required when higher accuracy is desired.

The sizing process of an aircraft is, according to Nam [29], a balance of energy and power; i.e. using the wing-loading and power-loading graphs to converge to a certain design point. Since the specific energy density of fuel is relatively low, adding range to the mission does not affect the aircraft design very much. The specific energy density of batteries however is between 60 and 100 times lower compared to fuel. Therefore, when changing the mission requirements by for example increasing the range, the aircraft weight will change drastically as well. A heavier aircraft influences the wing- and power-loading, and through this the total surface area and/or maximum lift coefficient.

In this work, the tools that are used are either freely available (AVL, XFOIL) or developed by the author (battery analysis, etc.). The complete mission is broken down into mission segments that are either constant (cruise), or varying within the segment (optimal operation during climb varies with altitude). Furthermore, the efficiencies of the disciplines are non-linear as they are modeled for each operating condition.

2.2.1. Modules of the Simulation and Their Requirements

The required modules that need to be included in the aircraft simulation are very similar to those presented in the legacy aircraft design books such as those of Raymer [38], Roskam [40] and Torenbeek [45]. Traditionally, aircraft sizing and synthesis consists of a constraint and mission analysis, resulting in a feasible region of power/thrust and wing loadings. Over the years, these rules have been matured for conventional aircraft. For aircraft with unconventional types of energy however, a great deal of modification is required according to Nam, Soban, and Mavris [30], Nam et al. [31]. As this thesis concerns the redesign of a case-study, the starting point of each design is the Panthera. From there, the optimizer will search for a better design tailored for a particular design mission. Below here, an overview is given of the required modules.

- **Geometry** — The shape and size of the main wing needs to be parameterized here. The resulting geometry needs to be used in the aerodynamic analysis for the generation of lift-drag polars and in the weight estimation module. Furthermore, the wing geometry is used to determine the volumetric feasibility of storing all the batteries in the wing. Lastly, the tail is resized such that the same tail volume coefficients are maintained. In Section 2.3 more details will be presented regarding the geometry module.

- **Aerodynamics** — This module is responsible for the generation of the lift-drag polars of the entire aircraft. These polars will form the basis of the mission analysis module, as they dictate the amount of drag produced for the various flight conditions encountered during the mission. Furthermore, the high-lift characteristics need to be calculated here. In the simulation, high-lift performance is calculated using a surrogate guess of the maximum lift coefficient. To ensure feasibility, the difference between the actual $C_{l_{max}}$ and the $C_{l_{max}}$ corresponding to the surrogate guess at each station is used in the inequality constraints.

- **Mission and Flight Mechanics** — The flight dynamics equations for the whole mission profile will be solved here, translating the aerodynamic characteristics into propulsion system requirements such as the amount of thrust required, the airspeed, and density at each moment in time. The optimal airspeed during the climb phase depends on both aerodynamic and propulsion characteristics, as the airspeed influences

Table 2.1: Design variables

	Design Variable	**Symbol**	**Units**	**Norm.**	**Lower B.**	**Upper B.**	**Initial Value**
Surrogate	Max. takeoff mass	m_{MTO}	kg	1500	900	2500	1300
	Max. lift coefficient	$C_{L_{max}}$	-	1.8	1.3	2.3	1.91
	Battery capacity	Q	kWh	30	1	inf	20
	Fuel weight	m_{fuel}	kg	20	0	inf	20
Operational	Throttle ICE: climb	δT_{climb}	-	1	0	1	1
	Climb coefficient	C_{climb}	-	1	0	1	0.7
	Electrification	ϵ	-	1	0.0001	1	1
	Throttle ICE: h-cruise	$\delta T_{h-cruise}$	-	1	0	1	1
	Throttle ICE: e-cruise	$\delta T_{e-cruise}$	-	1	0	1	0
Geometrical	Surface area	S_{ref}	m^2	11	5	30	11.3
	Aspect ratio	AR	-	10	5	40	10.4
	Taper ratio	λ	-	0.5	0.2	1	0.44

the advance ratio of the propeller and thus the optimal rotational speed of the propeller and electric motor. Due to this mutual influence, a small feedback loop is introduced between the two modules, as will be further elaborated on in Section 2.8.1.

- **Propulsion Systems** — Here, the performance of the propulsion systems will be computed. Based on the amount of thrust that need to be produced at each moment in time, the total battery capacity and fuel consumption need to be computed. It is important that these power-profiles are processed accurately throughout the whole power conversion chain, since the required battery capacity has a large impact on the total aircraft weight. Furthermore, the performance of the electric motor and internal combustion engine are scaled here if their maximum power output is added to the design variables.

- **Weight Estimation** — In the weight estimation the mass of all the components will be computed and summed, resulting in the maximum take-off weight.

The design variables that have been chosen are presented in Table 2.1. They are split into three groups: surrogate variables that enable the decoupling between modules, operational variables that determine the control laws of the power management system, and lastly the geometrical variables that manipulate the main wing its planform. Furthermore, the constraints presented in Table 2.2 need to be implemented to ensure a feasible design.

2.2.2. Interconnection of Modules: Design Structure Matrix

To give a clear overview of the interconnection of all modules, a Design Structure Matrix (DSM) has been produced and presented in Figure 2.1. All modules are controlled by the optimizer. The first input of the optimizer is an initial design vector. From here, it will try to move towards an optimum following the procedures presented in Section 2.1. The objective and constraint functions have been merged into one function, as most of the calculations for the objective values need to be performed for the constraint functions as well. In the DSM, variables labeled with a '*' are surrogate variables used to decouple modules. As can be seen, there is a small feedback loop between the mission analysis and propulsion system analysis. This loop is introduced to couple the mission analysis with part of the propulsion analysis. As the mission analysis equations and the performance equations

Table 2.2: Design constraints

Type	Constraint	Notes
Inequality	Bounds	Linear bounds on design variables
	Stallspeed	Stallspeed should be lower than 65 kts
	Takeoff	Minimal takeoff field length should be lower 400 m
	Climb	Climb angle should be higher than 4.7 deg
	$C_{l_{max}}$	At each semi-spanwise section, the difference between the actual local $C_{l_{max}}$ and the local C_l corresponding to the surrogate $C_{L_{max}}$
	Battery	Battery volume should fit in the wings
Equality	Surrogates	The difference between actual and surrogate variable should be zero

of the propeller are very computationally inexpensive, it is beneficial to reduce the optimization problem size. By doing so, the chosen architecture is a hybrid IDF/MDF, but mostly IDF.
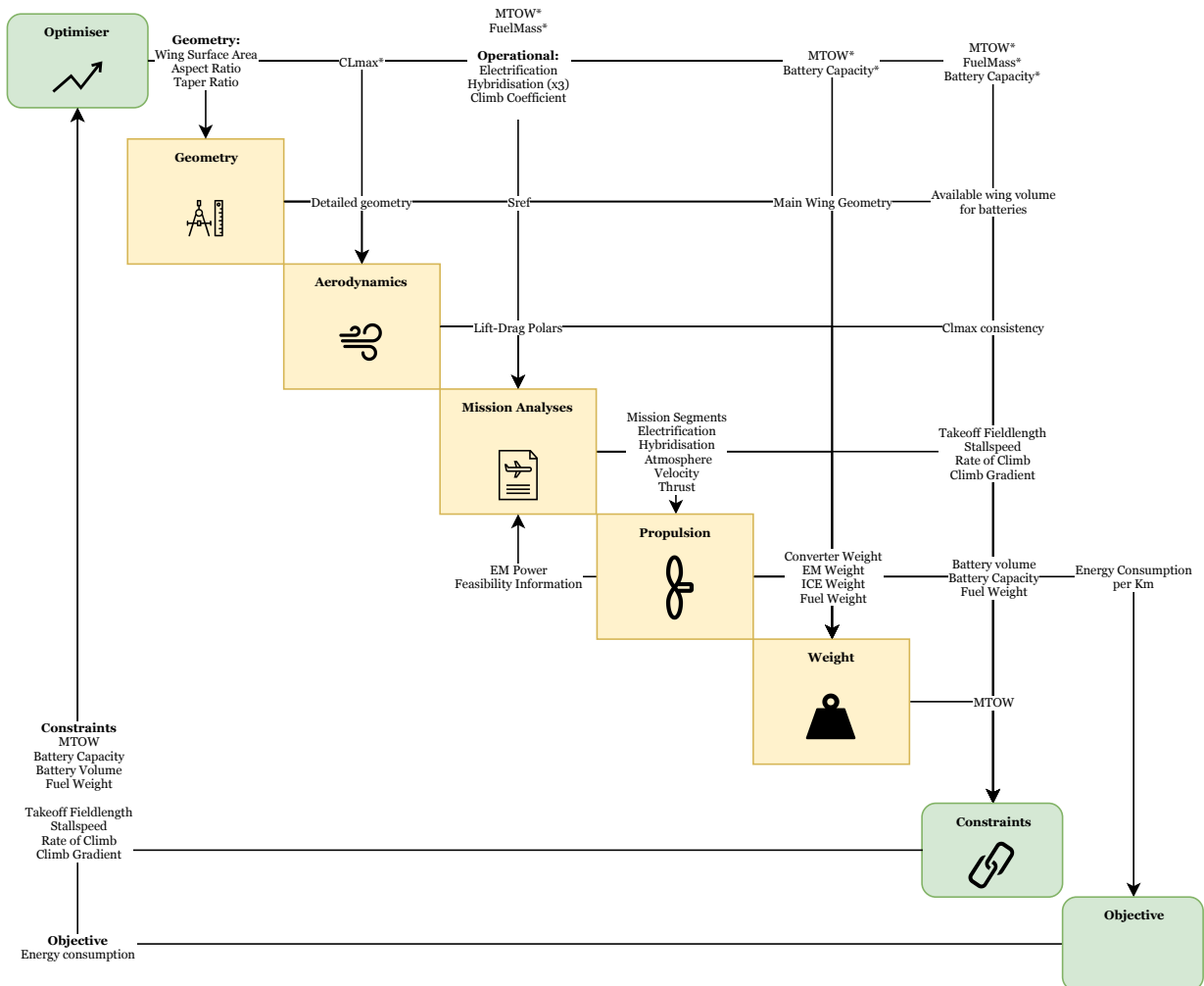
Figure 2.1: Design Structure Matrix: an overview of the required sub-modules and their interconnection.

2.2.3. Assumptions on the Influence of Batteries on Wing Weight and C&S

To ensure the research can be completed within the predefined time, certain assumptions needed to be made. An overview of the most important assumptions on a simulation-module level is presented below.

Wing Weight Due to Battery Placement

There are two factors that should be considered when analyzing the influence of batteries on the wing weight: load relief during flight and load intensification during touchdown and while being stationary on the ground. The ultimate load-factor of 6.6 roughly equates to an effective lift vector equivalent to $9,500\ kg$, distributed over the wing. Batteries of around $500\ kg$, for example, relieve this load by approximately 5%. In contrast to fuel, the battery weight does not reduce during flight, hence the load relief stays constant throughout the mission.

On the other hand, due to the rapid vertical deceleration during touchdown, the wing is subjected to larger forces in the gravity-direction; i.e. the inertia effect of the relatively heavy wing with batteries is larger compared to an empty wing. The additional structure required to ensure wing structural integrity adds to the total wing weight. The complexity of the models required to capture this effect in a meaningful way poses a serious threat to the feasibility of developing such a module. Both for this and the aforementioned argument, the influence of battery weight on the wing its structural weight has been taken into account.

Stability and Control

Several problems due to the placement of batteries could arise in the field of stability and control. The weight of the batteries could shift the center of gravity forwards, diminishing the stability and control characteristics; e.g. increasing the effectiveness of the horizontal stabilizer and thereby affecting the short period and phugoid performance, introducing more trim-drag and even reducing the controllability of the aircraft.

Additionally, by placing the batteries in the wings, the aircraft its roll inertia will be increased. As a result, the acceleration in roll-rate will be lower. When designing for roll performance, this could mean an increase in aileron effectiveness is required to meet certification regulations. Other areas of effect will be on the dutch roll, spiral and a-periodic roll performance.

Working out the aforementioned effects requires a detailed analysis of the stability derivatives, including the careful resizing of the tail, repositioning of the main wing, resizing of the control surfaces and a detailed analysis of the eigenmotions. Since this research is mainly focused on the synergistic benefits of the main wing and the propulsion systems, these effects on stability and control are not taken into account.

2.3. Geometry

To ensure that the calculated lift and drag characteristics are as close as possible to the characteristics of the actual Panthera, it is important that the geometry is modeled accurately. A three-dimensional CAD-model has been converted to a point-cloud with a little over 2 million data points, as can be seen in Figure 2.2. These points are formated in such a way that a triangulated surface representation using vertices and faces can be made. The top and side views of the baseline aircraft are shown in Figures 2.3 and 2.4 respectively. Using the method of Moller [28], the intersection between two surface representations can be calculated. A plane is moved from the root to the tip of the wings, and at 120 locations the intersection-points between the triangles of the point-cloud and the plane are calculated.

At each cross-section, the calculated points are used to determine the CST coefficients; see Kulfan [23] for more information about the CST representation. By changing the CST coefficients, the airfoil shape can be easily and optimizer-friendly manipulated. Furthermore, the generated points are used to determine the local
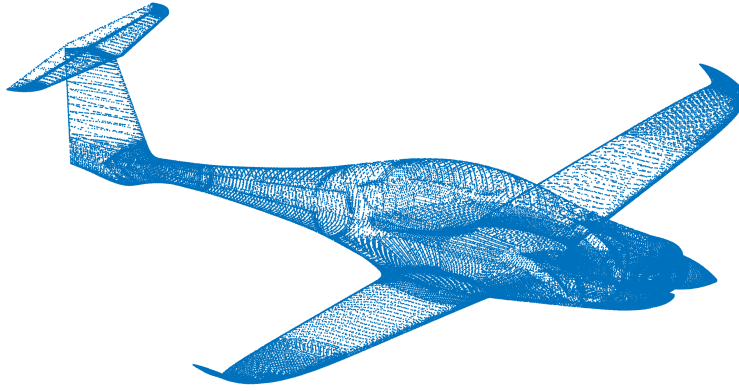
Figure 2.2: Point cloud representation of the baseline Panthera using $1/10^{th}$ of the total number of points
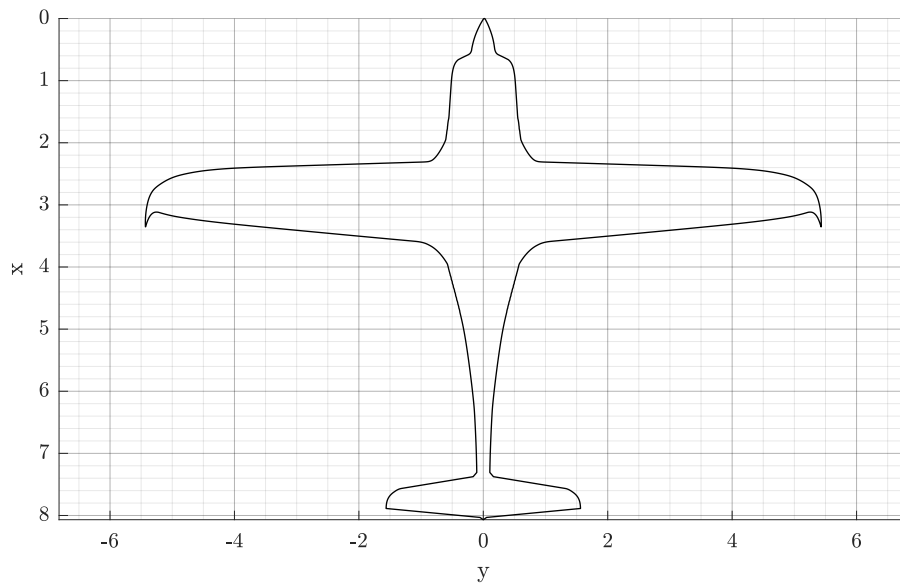
Figure 2.3: Top view of baseline aircraft
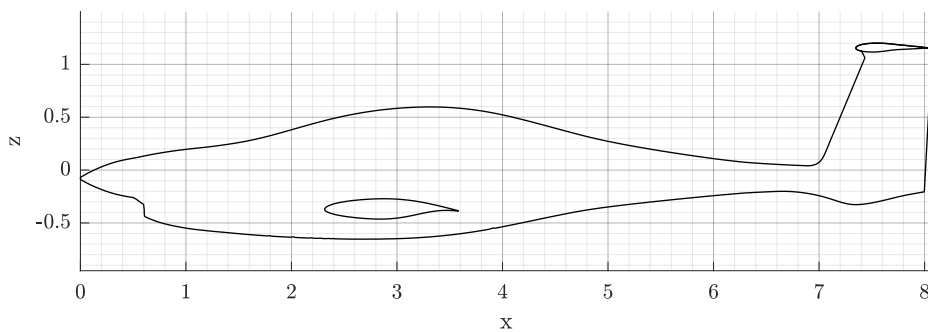
Figure 2.4: Side view of baseline aircraft

sweep, dihedral, chord length, twist, and quarter-chord point of the sections. The mean aerodynamic chord of the main wing is shown in Figure 2.5. Since the representation needs to both accurately describe the current shape and at the same time be flexible and simple enough to be used by an optimizer, the reference geometry is

Table 2.3: Geometrical properties of the baseline wing of the Panthera

	Symbol	Value	Unit
Surface Area	S	11.3	m^2
Aspect Ratio	AR	10.4	-
Taper Ratio	λ	0.44	-
Sweep Angle (c/4)	$\Lambda_{c/4}$	0	deg
Dihedral Angle	Γ	4.2	deg
Span	b	10.8	m
Rootchord	C_r	1.44	m
Mean Aerodynamic Chord	C_{MAC}	1.12	m
Winglet Tip Chord	$C_{t,winglet}$	0.17	m
Wetted Area	S_{wet}	23.3	m^2
Maximum thickness to chord	t/c_{max}	15	%
Location max. t/c	$x/c_{t/c_{max}}$	44	%
LE sharpness parameter	$\Delta Y/c$	3.4	%

used as a starting point and will be manipulated. Table 2.3 shows the baseline properties. The parameters used to change the baseline geometry will be described next.
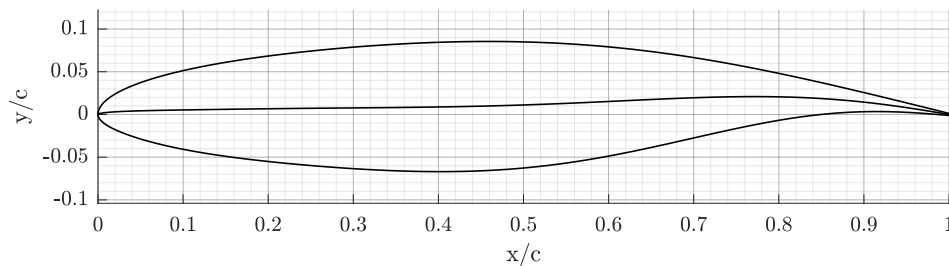
Figure 2.5: Airfoil shape at the mean aerodynamic chord

Firstly, the wing surface area should be manipulated. In conceptual design, the wing-loading is one of the most powerful parameters one can play around with and is one of the main drivers behind the wing planform. Being able to simply change the surface area to either keep the wing loading constant when the mass is changing or to change the wing loading for a constant mass is very important in this stage of the design. Furthermore, the aerodynamic performance of the wing is closely tied to the wing aspect ratio. The lift-induced drag of lifting surfaces decreases with increasing aspect ratios. For this reason, glider planes for example have very long wings with a high aspect ratio. Lastly, the taper ratio is added as geometry parameter. Highly tapered wings have a small tip deflection ratio, due to its inherent stiffness, allowing for a larger span and a potentially lower induced drag. One of the drawbacks of highly tapered wings is the high local c_l near the tip which can lead to tip stall during flight. The small chord Reynolds numbers near the tip aggravate the tip stall problem even more. The effect of these three variables on the geometry is shown in Figures 2.6, 2.7, and 2.8. In these figures, the solid lines (——) represent the baseline wing shape.

Next to the aforementioned parameters, the geometry can be manipulated by some other parameters. The chord length of the winglet and the speed of transition from main wing to winglet can be changed by two parameters. The x- and z-location of the winglet tip quarter-chord, along with the sweep and dihedral angle of the main wing can be changed. Lastly, the twist distribution is defined using an incidence angle, a washout an-

— · — · - S = 8.7 m^2
———— S = 11.3 m^2
— — S = 14.7 m^2

— · — · - AR = 8.0
———— AR = 10.4
— — AR = 13.5

— · — · - λ = 0.21
———— λ = 0.45
— — λ = 0.71
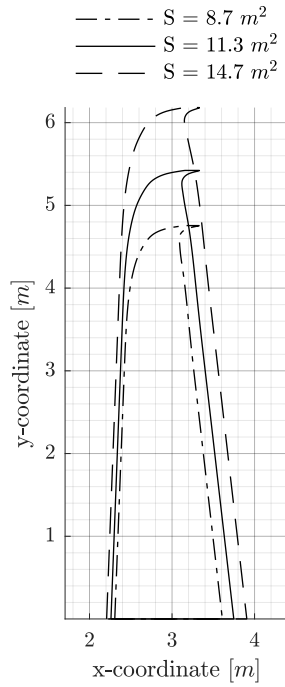
Figure 2.6: Influence of surface area on the wing geometry
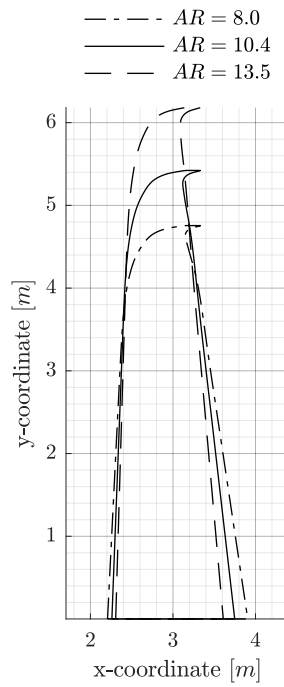
Figure 2.7: Influence of aspect ratio on the wing geometry
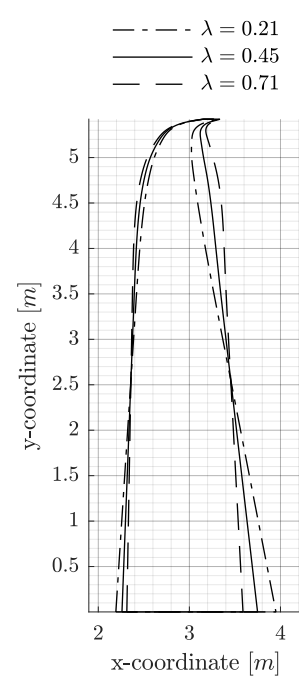
Figure 2.8: Influence of taper on the wing geometry

gle, and two CST-coefficients that determine the transition in terms of twist from root to tip. It has been found that the effect of these additional geometrical parameters are insignificantly small compared to the surface area, aspect ratio and taper ratio. For that reason, they will not be focused on in this study.

When determining airplane drag, it is important to accurately know the wetted area. This is because the friction drag has a large contribution to the total drag of the aircraft. By using the cross-product between two legs of each triangle, the total wetted area can be calculated. Since the point-cloud of the fuselage is triangulated, its wetted area can be calculated directly. Using the three-dimensional airfoil coordinates of all sections, a triangulated representation of the wing surface can be made, which in turn forms the basis for surface area and wetted area calculations.

2.4. Aerodynamic Analysis

The aerodynamics module is responsible for the generation of the lift-drag polars of the entire aircraft. These polars will from the basis of the mission analysis module, as they translate the the various flight conditions encountered during the mission to the amount of drag produced. Furthermore, the high-lift characteristics are calculated in this module to determine the stall characteristics of the aircraft. This is done by using a surrogate guess of the maximum lift coefficient and, to ensure feasibility, using the difference between the actual $C_{l_{max}}$ and the $C_{l_{max}}$ corresponding to the surrogate guess at each station in the inequality constraints. First, the aerodynamic drag breakdown and approach is discussed.

2.4.1. Drag Breakdown

The aerodynamic drag can be broken down using three different approaches, as presented in Figure 2.9; A energy breakdown, a computational breakdown, and a physical breakdown. Below, these three approaches will be discussed.
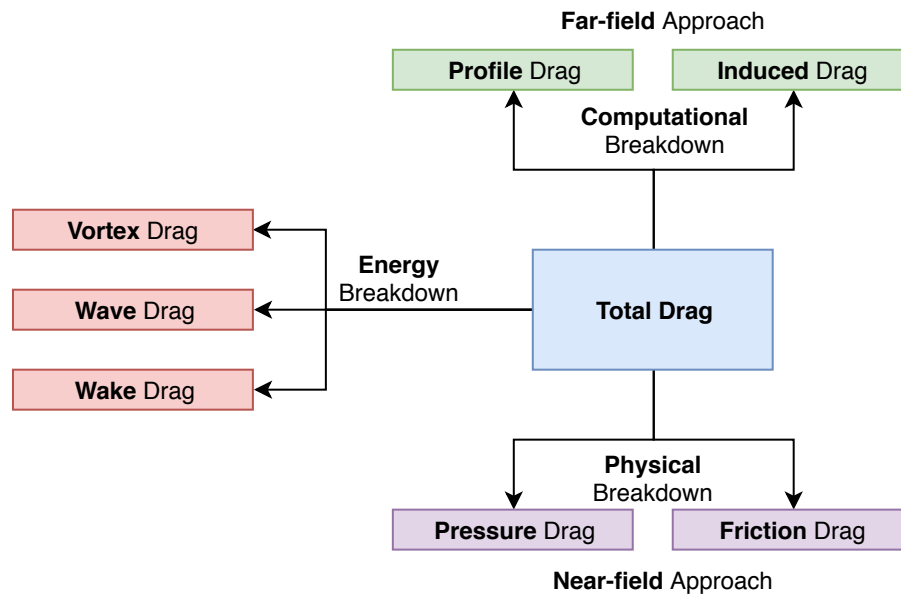
Figure 2.9: Three approaches to the drag breakdown, reproduction from Middel [27]

- **Physical** — One analyses the nature of the acting elementary forces. Two basic types of force can be identified: Pressure and shear forces. Pressure drag results from the normal force acting on the geometry whereas friction drag is due to the shear forces. Both forces are summed over the panels at the geometry surface resulting in lift, drag, and moments. To obtain an accurate analysis, a detailed paneling is required. As a consequence, the ease of modeling and amount of computational resources are compromised to gain a better understanding of local flow problems and accuracy of the solution. Generally, these methods are used only in later stages of the design for analysis rather than design. Since these basic forces act close to the surface, this approach can also be referred to as near-field approach.
- **Computational** — the drag is broken down into two sources: The lift-related induced drag, mainly coming from the aerodynamic surfaces, and the non-lift-related profile drag. Profile drag is a result of the shape of the geometry, including areas of seperation and boundary layer effects. This method derives its name from the fact that a combination of different computer programs can be used to very efficiently compute both the induced and profile drag. Basing the calculations on circulations rather than pressures has two significant advantages; The geometry detail required as well as the computational time is much lower compared to a near-field approach. By combining a method that calculates the global lift-induced characteristics with a method that estimates the profile drag, one is able to predict the lift curve, drag polar and moments reasonably well for the conceptual stage of the design. In constrast to a physical approach, this method can be seen as a far-field approach.
- **Energy** — The aircraft drag is equivalent to a transfer of energy to the flow. There are three major areas where energy dissipates: In the boundary layer and due to flow seperation. This is called wake drag. Vortex-induced drag is due to the kinetic energy transfered into the flow. Lastly there is wave drag, which is energy loss due to flow compressibility effects such as shock waves.

Table 2.4: Operating conditions of the original Panthera

	Velocity V [kts]	Altitude h [$10^2 \cdot ft$]	Reynolds Number** Re [10^6]
Stall (Clean)	65	0	2.5
Cruise (Hybrid)*	125	120	3.6
Economy	177	150	4.8
Cruise	193	120	5.6
Maximum	220	0	8.6

  * Chosen flight condition of hybrid operation
 ** Reynolds number depends on MAC, this is updated constantly in the aerodynamic tool

In view of the requirements dictated by conceptual design, namely little need for computational resources and the ability to give an accurate prediction based on limited geometric detail, the computational far-field approach to determine the aerodynamic characteristics of the aircraft has been chosen. The tool to predict lift, pitching moment, and lift-induced drag is Athena Vortex Lattice (AVL), a vortex lattice method (VLM). To overcome the lack of modelling any viscous effects, AVL is coupled with XFOIL, a two-dimensional viscous/inviscid interaction tool. For wings with conventional shapes, three dimensional viscous effects such as cross-flows or interference drag are usually negligible under the assumption of small angles of attack. Furthermore, the drag due to the fuselage, and the horizontal and vertical tails are calculated using a mixture of methods from the legacy design books. Lastly, since the propeller creates a wake in which the fuselage is situated, the additional drag due to this wake is calculated.

Operating Conditions

The original Panthera operates under a variety of conditions. The most important conditions are shown in Table 2.4. As can be seen, the Reynolds numbers vary by a factor 4 over the complete mission profile. To compare the lift-drag polar with the reference polar, the original cruise condition with a Reynolds number Re of $5.6 \cdot 10^6$ has been taken as a reference. During the mission analysis, the polar is adjusted for the specific operating conditions at which the aircraft flies. It is important to note that the Reynolds number is constantly changing in the analysis, as the mean aerodynamic chord changes with wing planform. In the aerodynamic tool, this change in Reynolds number is constantly taken into account.

2.4.2. 3D Inviscid Flow Analysis Using AVL

The computer code AVL, see Drela [7], is used to determine the three-dimensional aerodynamic behaviour of the aircraft configuration. AVL represents surfaces and their trailing wakes as single-layer vortex sheets, discretised into horseshoe filaments. All the filaments together form an aerodynamic influence coefficient matrix that can be used to determine aerodynamic properties such as lift, moments and lift-induced drag. It finds its basis in four fundamental theories.

- Biot-Savart Law: each vortex line of certain circulation induce a velocity field
- Kutta-Joukovsky theorem: a vortex of certain circulation moving with a velocity experiences a force
- Hermann von Helmholtz theory: describing the principles of vortex filament behaviour; It must form a closed path and the circulation along one vortex filament is constant.
- Prandtl lifting-line theory: a vortex loses strength along the whole wingspan.

Based on these theories and the way they are implemented in AVL, certain limitations of the code arises. The

most important limitations come from:

- Potential flow: No viscous effects such as turbulence, dissipation and boundary layer effects. It does not give any information about transition or stall. Also, only the induced drag component can be calculated.
- Incompressible: Only reliable for low Mach numbers. Compressibility is treated using the classical Prandtl-Glauert (PG) transformation.
- Cambered profiles can be modeled, however, no thickness effects can be taken into account.
- Trailing vortices are going in chord direction: The freestream must be at sufficiently small angles to the x-axis, so small angles of attack only.
- Flow is quasi-steady: meaning unsteady vorticity shedding is neglected. It is for virtually every expected flight manoeuvre true.

Besides the total lift and lift-induced drag, AVL computes the spanwise lift-distribution over the aerodynamic surfaces. This spanwise distribution of the main wing is used as input for XFOIL to determine the corresponding profile drag. The geometric input used for AVL is presented in Figure 2.10. The main wing is divided into 18 sections with a sine distribution concentrated towards the tip. For the horizontal stabiliser, 10 sections have been used with the same distribution. The vertical stabiliser is divided into 8 sections. In chord-wise direction, 8 vortex points have been used for all the surfaces.
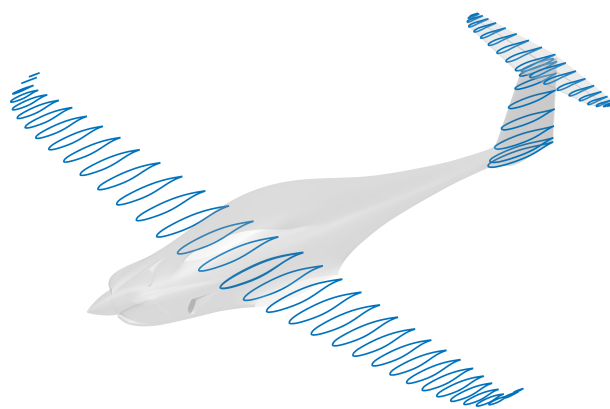
Figure 2.10: Airfoil sections used as input in AVL

2.4.3. Viscous/Inviscid Section Analysis Using *XFOIL*

To determine the two-dimensional aerodynamic characteristics of the wing sections, use have been made of the external computer program XFOIL, see Drela [6]. In several publications, the principles of XFOIL are presented in detail, Drela [8, 9, 10, 11], Drela and Giles [12]. It is best described as a fully-coupled viscous/inviscid interaction method that solves the two-dimensional flow over an airfoil. Below, the principles behind the methods will be briefly discussed.

The inviscid formulation is based on a simple linear-vorticity stream function panel method. To correct for compressibility, and thereby obtain a good prediction up to sonic conditions, a Karman-Tsien compressibility correction is incorporated. Due to the influence of viscosity, a boundary layer will be formed near the surface of the airfoil, which requires a viscous method to solve. In stead of taking viscosity into account for the complete flow, it is only considered in the area where the boundary layer is actually formed.

The boundary layers are described using empirical relations that are obtained as result of extensive research. More precisely, a two-equation lagged dissipation integral formulation is implemented. The transition point is

determined using the amplification ratio e^n criterion. To enforce interaction between the boundary layer development and the outer flow solution, a wall-transpiration model is implemented. The drag is determined from the wake momentum thickness far downstream. Using a full-Newton method the whole system of equations is solved resulting in excellent convergence speeds.

In total, 15 sections ranging from root to tip are analyzed for 6 different Reynolds numbers ranging from $0.2M$ to $14M$ from an angle of attack α of -4 to 22. The Reynolds numbers range from the lowest to the highest possible value that can occur during the flight. Figure 2.11 shows the result of the mean of aerodynamic chord of the original Panthera for two different Reynolds numbers. As can be seen, the maximum lift coefficient is reduced when decreasing the Reynolds number. Furthermore, the drag coefficient increases for a decreasing Reynolds number.
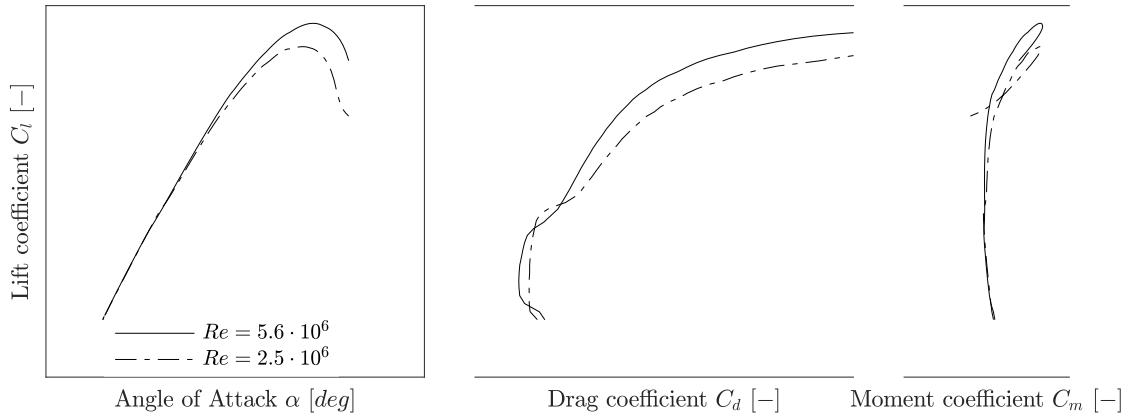
Figure 2.11: Lift, drag and pitch moment polars of the mean aerodynamic chord of the Panthera

To make sure complex boundary layer effects are modeled properly, enough panels need to be used in the analysis. However, when using to much panels, roundoff errors can occur and decrease the accuracy of XFOIL. Using 150 panels results in enough accuracy and the least amount of convergence failures. To reduce the number of failures when analyzing difficult shapes, Reynold numbers and angles of attack, a Hanning window filter function is used. This approach hardly changes the outcome of XFOIL but increases its performance significantly.

Unsurprisingly, not all angles of attack result in a converged solution. Therefore, the first step after obtaining the polars is to interpolate the missing angles of attack. When the interpolated polars from XFOIL are used directly in a three dimensional look-up table, undesired oscillations occur. For that reason, the polars are filtered and corrected with a smoothing spline.

2.4.4. Quasi Three Dimensional Coupling of *AVL* and *XFOIL*

In the quasi three dimensional coupling module (Q3DM), the two dimensional results from XFOIL are combined with the three dimensional results from AVL to accurately predict the total wing drag. The approach implemented in this research is entirely based on the quasi three dimensional aerodynamic solver presented in Mariens, Elham, and van Tooren [24]. However, there are some differences.

Firstly, the sweep theory has been removed from the method. This is justified since the mach numbers are below 0.4 resulting in an optimum wing which has, if any at all, a low sweep angle. Secondly, the way XFOIL is used in the modified tool is different. In the original Q3D tool, after the three dimensional VLM analysis has been performed for a certain wing lift coefficient, XFOIL is run iteratively to determine the actual two dimensional lift-

drag characteristics at certain spanwise sections. The modified Q3DM in this thesis determines the 2D airfoil performance by interpolating from a large database containing detailed lift-drag polars of various spanwise sections, each for different Reynolds numbers. As a result of this modification, Q3DM can be used to determine the complete wing lift-drag polar in a fraction of a second instead of tens of seconds to a few minutes.

Profile and Interference Drag of Fuselage, Horizontal and Vertical Stabilizers

The profile and interference drag of the fuselage, horizontal stabilizer, and vertical stabilizer can be calculated using Equation 2.13. This formula consists of 4 terms, each of which takes something different into account. At the basis there is the flat plate skin friction coefficient C_f, a dimensionless skin shear stress. The magnitude of this friction coefficient depends on Reynolds number Re, and whether the flow is laminar or turbulent. As suggested by Roskam, the fully turbulent skin friction coefficient is used. Furthermore, the surface area of the imaginary flat plane influences the amount of drag force, hence the presence of S_{wet} in the formula. A interference factor κ_i is introduced to account for interference drag. To correct the formula for shapes that actually do have curvature along the surface area, the friction coefficient is multiplied with a shape factor SF. The shape factor for the fuselage is shown in Equation 2.14 and that of the lifting surfaces is shown in Equation 2.15.

$$C_{D_P}S = \kappa_i SF \cdot C_f S_{wet} \tag{2.13}$$

$$SF_{fuselage} = 1 + \frac{60}{f^3} + \frac{f}{400} \qquad\qquad f = \frac{l_f}{d_f} \tag{2.14}$$

$$SF_{wing} = 1 + \left[\frac{0.6}{(x/c)_{(t/c),\max}} (t/c)_{\max} + 100 \, (t/c)_{max}^4 \right] 1.34 M^{0.18} \tag{2.15}$$

To be able to compare the drag coefficient numbers, the different attributes of the formulas are shown in Table 2.5. As can be seen, the Reynolds number of the fuselage is due to its length much higher compared to the other components. The skin friction coefficient decreases with increasing Reynolds number. The shape factor of the main wing is the lowest of the lifting surfaces. The shape factor of the fuselage is 0.19 higher compared to the vertical stabilizer. This seems reasonable when comparing the shape of the fuselage.

The calculated equivalent skin friction coefficient of the main wing is significantly lower compared to the friction coefficients of the stabilizers. This is because for the stabilizers it is assumed that the flow is fully turbulent. Using the combination of *AVL* and *XFOIL*, the transition point is actually calculated, leading to a much lower skin friction coefficient when a large part of the wing has laminar flow. During cruise conditions, about $40-50\%$ of the wing experiences laminar flow, hence the friction coefficient is considerably lower. It is possible to determine the actual skin friction coefficient of the stabilizers using the same method used for the main wing, however, since the scope is to redesign the wing and not the stabilizers it has been decided to only apply this to the main wing.

Lift Induced Drag Due to the Fuselage

The drag that is induced over the fuselage due to lift is calculated using the empirical relations of Roskam, as shown in Equation 2.16. It is based on the steady state cross-flow drag coefficient for a two-dimensional circular cylinder, which is determined experimentally. To account for the three-dimensional effects, the ratio of the drag of a finite cylinder to the drag of an infinite cylinder η is introduced. The experimental steady state cross-flow

Table 2.5: Parameters for calculation of profile drag C_{D_p}. *: using the result of $Q3D$, the average skin friction coefficient has been calculated that would lead to the same drag coefficient. (Laminar and turbulent flat plate friction for the wing are: $0.56 \cdot 10^{-3}$ and $3.3 \cdot 10^{-3}$)

	Re [10^6]	C_f [10^{-3}]	SF	κ_i	S_w [m^2]	$(t/c)_{max}$	$(x/c)_{(t/c)_{max}}$	C_{D_p} [10^{-3}]
Fuselage	29.9	2.5	1.73	1.04	23	-	-	9.1
Horizontal Stab.	2.6	3.7	1.40	1.08	3.0	0.12	0.26	1.5
Vertical Stab.	4.4	3.4	1.55	1.08	2.3	0.19	0.42	1.0
Main wing	5.6	1.7*	1.36	1.13	23.6	0.15	0.43	5.3

drag coefficient of a circular cylinder is c_{d_c}. Furthermore, the angle of attack α of the fuselage is the parameter that relates the drag of the fuselage to the lift. Lastly, the drag coefficient in this formula is normalized with respect to the planform area $S_{plf_{fus}}$ of the fuselage. Compared to the lift induced drag produced by the main wing at the same lift coefficients, the contribution of the fuselage is quite small.

$$C_{D_{L,fus}} \cdot S = \eta c_{d_c} \alpha^3 S_{plf_{fus}} \tag{2.16}$$

Lift and Drag Characteristics of High Lift Devices

The high lift characteristics of the aircraft are determined using the empirical relations presented in Roskam [40, Part VI, Chap. 8]. The flaps-down polar is obtained with the flaps-up polar in three steps, following Figure 2.12. First the change in lift coefficient of the linear part of the polar is calculated and added to the clean polar. Then, the change in lift slope is calculated. As last step, the polar is shifted to arrive at a certain change in maximum lift coefficient. For non-translating flap systems, such as plain flaps, the wing lift curve slope flaps-down is considered to be the same as the flaps-up slope according to Roskam. Since the lift coefficient versus angle of attack curve of the aircraft is obtained from *AVL*, there is no change in slope for higher angles of attack. This is because it assumes potential flow and cannot model flow separation. Furthermore, since the high-lift polar will be mainly used for the takeoff, landing, and stall analysis, the change in maximum lift coefficient due to the flap deflection will be calculated.
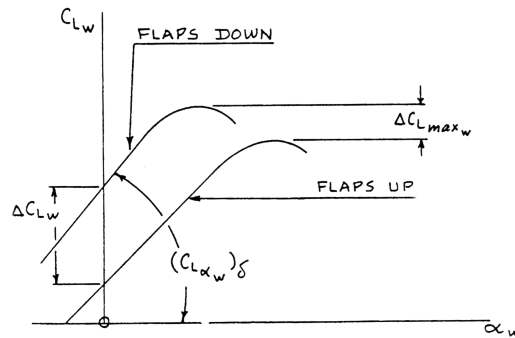
Figure 2.12: Lift polar aircraft with flaps. Image from Roskam [40, Part VI, Sec. 8.1.3.4]

The change in maximum lift coefficient departs from a base change in maximum 2D lift coefficient, as shown in Equation 2.17, which depends on the thickness to chord ratio of the mean flapped section. This base change is multiplied by the factors k_1 and k_2 to account for flap-chord to airfoil ratios different from 25 percent and for flap angles different from the reference flap angle. This change in maximum 2D lift coefficient is used in Equation 2.18 to calculate the change in maximum wing lift coefficient. The ratio between wing surface area

where flaps are attached and the total surface area is captured in S_{wf} and S. To correct for differences in the planform, the factor K_Δ introduced. Using the change in lift, the additional drag can be computed with two formulas, one for profile drag and one for induced drag.

$$\Delta c_{l_{max}} = k_1 k_2 k_3 \Delta c_{l_{max}}^{base} \tag{2.17}$$

$$\Delta C_{L_{max}}^{wing} \cdot S = \Delta c_{l_{max}} \cdot K_\Delta \cdot S_{wf} \tag{2.18}$$

The profile drag increment due to the flaps, Equation 2.19, follows from the two-dimensional profile drag increment due to flaps, the quarter-chord sweep angle, and the wetted area of the flapped region. The induced drag increment due to flaps, Equation 2.20, is a function of the incremental lift coefficient due to the flap, an empirical constant based on the spanwise position of the flaps, and the quarter-chord sweep angle.

$$\Delta C_{D_{prof_{flap}}} \cdot S = \Delta C_{D_{p,\Lambda_{c/4}=0}} \cos(\Lambda_{c/4}) \cdot S_{wf} \tag{2.19}$$

$$\Delta C_{D_{i_{flap}}} = K^2 \Delta C_{L_{flap}}^2 \cos(\Lambda_{c/4}) \tag{2.20}$$

2.4.5. Lift-Drag Polar in Clean Configuration

Using the aforementioned tools, the lift-drag polar can be produced for various different conditions. A reference lift-drag polar for a Reynolds Number Re of $5.6 \cdot 10^6$ has been provided by Pipistrel to validate the generated aerodynamic module. In Figure 2.13, the drag coefficients of the various components have been plotted against the lift coefficient, including the reference polar. To account for miscellaneous drag contributions, an offset is added with an equal magnitude as the difference in cruise condition of the reference Panthera at the cruise velocity. As can be seen, the actual polar is slightly under-predicted in the high-lift area. In the lower graph one can clearly see that the lift-induced drag (of the main wing and the horizontal stabilizer) is the most sensitive to lift. The main wing its profile drag increases with drag since the transition point moves towards the leading edge, which exposes a larger portion of the skin to turbulent airflow. The semi-cylindrical fuselage produces more drag because the complete aircraft is tilted under an angle of attack. The drag due to the propeller increases as well because when flying with higher lift coefficients the dynamic pressure change behind the propeller increases. As a consequence, the skin friction of the fuselage increases. In this model, the profile drag of the horizontal and vertical stabilizers are not a function of lift, hence the horizontal line in the graph.

2.4.6. Determining the Maximum Lift Coefficient of a Clean Wing

The change in maximum lift coefficient in a flapped configuration is based on the clean maximum lift coefficient. Potential flow codes such as AVL cannot predict any stall behavior. Therefore, other tools or formulas need to be used. As proposed in Roskam, the maximum clean wing lift coefficient can be determined by analyzing along the span-wise lift distribution where the two dimensional section would stall. The two dimensional analyses code XFOIL is capable of predicting the maximum section lift coefficient. By comparing the span-wise lift coefficients as determined by AVL with the maximum according to XFOIL, the maximum wing lift coefficient can be determined. Figure 2.14 shows this method. The surrogate $C_{L_{max}}$ line represents the span-wise lift distribution of AVL for a certain surrogate lift coefficient and the actual $C_{L_{max}}$ line represents the maximum lift coefficient of each section.

One method to implement the maximum lift coefficient, is by gradually increasing the lift coefficient of the aircraft and use the lift distribution output of AVL for comparison. The moment that any of the sections expe-
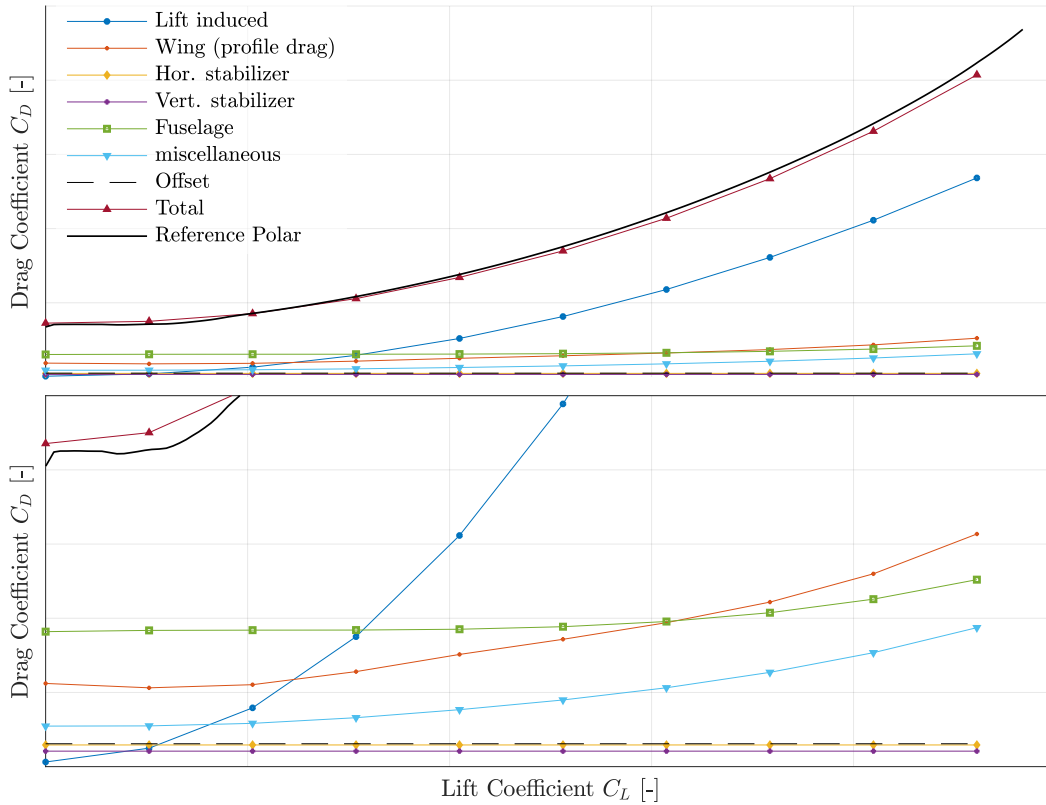
Figure 2.13: Lift-drag polar for a Reynolds Number Re of $5.6 \cdot 10^6$. The lower graph is a zoomed-in version of the upper graph.
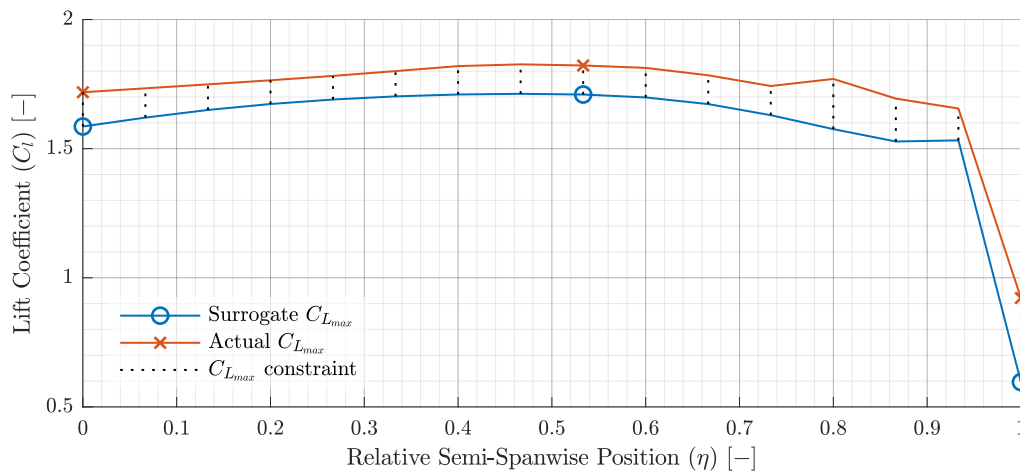
Figure 2.14: Lift distribution according to AVL at the surrogate maximum lift coefficient and actual local maximum lift coefficient as determined using XFOIL

rience stall determines the maximum lift coefficient of the clean wing. The advantage of this method is that within one simulation, hence for a fixed geometry, the maximum lift coefficient can be determined directly and can subsequently be used in other analysis modules. For example, it can be used to determine the stall velocity, which is one of the constraints.

Another possibility is to use a surrogate variable for the maximum lift coefficient and assume its feasibility

while using the constraint functions to actually ensure this feasibility. By adding the difference between the two lines from Figure 2.14 to the inequality constraints, the final aircraft configuration will be feasible.

Suppose a situation where the stall speed is an active constraint. In this senario, the maximum lift coefficient must be as high as possible to decrease the stall speed. Further assume that the actual maximum lift coefficient is constraint by a stalling tip section. If the method without the surrogate maximum lift coefficient is used, non of the changes made to the root distribution will have influence on the stall speed constraint, since it is determined by the tip section. However, during the finite difference analyses, it can be found that a higher root loading is favorable for the design. Hence, the solution to the quadratic sub-problem will suggest a search direction towards a higher root loading. It is quite possible that the root was already very close to stall. This would result in multiple failed line-searches and a slower convergence because the proposed geometries stall much earlier. However, this time at the root instead at the tip. When using the surrogate maximum lift coefficient, the influence of a higher maximum lift coefficient is communicated to the optimizer as well as a detailed demarcation of the feasible area resulting in a faster convergence.

2.4.7. Effect of Reynolds Number on Aircraft Drag and Maximum Lift

As indicated earlier, the Reynolds number influences the amount of drag and the maximum lift coefficient of the aircraft. To quantify this influence, a small study has been performed in which a variable Reynolds number polar is compared with a fixed polar. The results in terms of drag coefficient is shown in Figure 2.15. As can be seen, the maximum difference is approximately 7.5%. Furthermore, the result in terms of the maximum lift coefficient of a clean wing is shown in Figure 2.16. The difference in maximum lift coefficient is up to 10%. Given the magnitude of these errors, it is of added value to include the influence of Reynolds number on the drag coefficient and maximum lift coefficient.
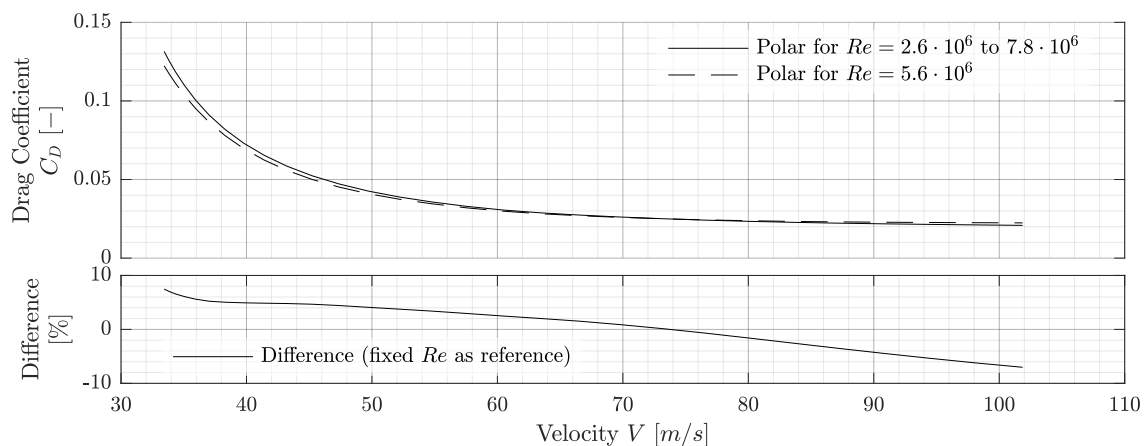
Figure 2.15: Influence of a variable Reynolds number polar on drag coefficient

2.5. Propulsion Systems

The analysis of the propulsion systems is one of the most important aspects of this thesis. The main function of the propulsion system is to convert energy, through a series of power conversion devices, into useful thrust. Ultimately, based on the amount of thrust that need to be produced at each moment in time, the total battery capacity and fuel consumption need to be computed. Since the required battery capacity has a large impact on the total aircraft weight, and thereby on the overall performance and design of the aircraft, it is of utmost
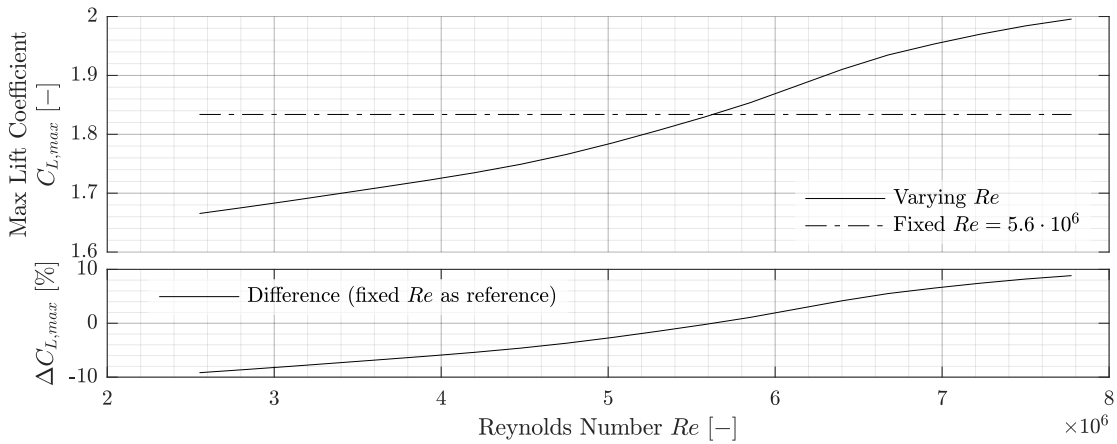
Figure 2.16: Influence of a variable Reynolds number polar on maximum clean wing lift coefficient

importance that it is modelled accurately. As will be elaborated on in Section 2.8.1, there is a need for a small feedback loop between the flight mechanics module and the propulsion systems module because the optimal flight speed is a function of rotational shaft speed of the propeller and electric motor.

First, an overview of the hybrid drivetrain will be given, after which each of the major components will be discussed.

Overview of the Hybrid Drivetrain

There are various different architectures possible that are hybrid-electric. Most schemes fall in the following categories: *series*, *parallel*, or *complex* propulsion system architectures. The Panthera is equipped with a series-hybrid propulsion drive train, as shown in Figure 2.17. Characteristic for this architecture is that the internal combustion engine generates shaft power which is in turn converted to electrical power. This is then combined with electrical power from batteries and delivered to the electric motor, which converts it to shaft power. Finally, the shaft power is converted in the propeller to thrust.
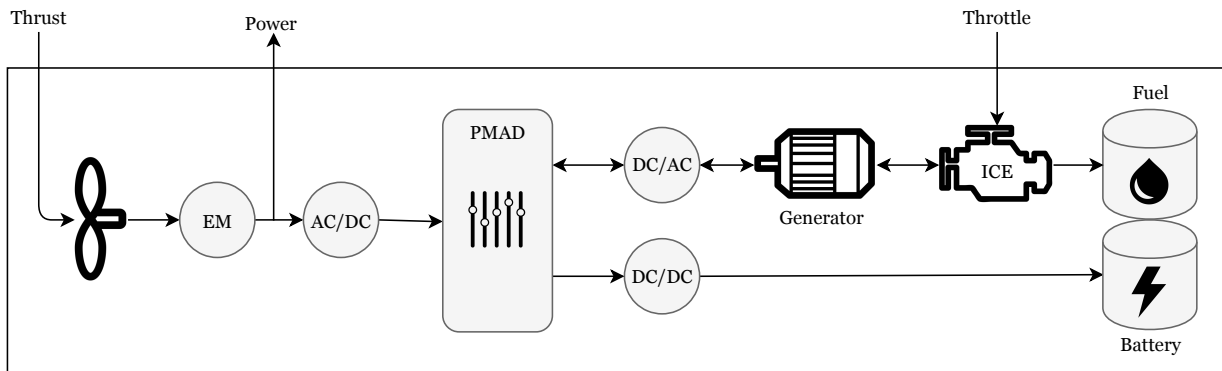
Figure 2.17: Overview of the hybrid-electric propulsion systems. The arrows indicate the propagation of information.

In a parallel architecture, the electric motor and the internal combustion engine are both connected to the same mechanical shaft. Optionally through the use of a gear-box. Both systems have some advantages and disadvantages. The advantages of a series system, according to Friedrich and Robertson [14], are the flexible location of the engine/generator combination, the simplicity of the drivetrain, and the suitability for short missions

profiles. Whereas the inherent disadvantages are the need for a generator and the design of the electric motor for maximum power. The advantages of a parallel architecture are that one can chose between a downscaled internal combustion engine or electric motor and that there is no need for a generator in this configuration. One of the main disadvantages of a parallel configuration is the need for much more complex controllers and mechanical coupling systems.

The way the propulsion system is approached in terms of modeling and information flows is the following: the flight mechanics module dictates the amount of thrust that is required for a certain flight mode and feeds that into the propulsion system module. Next, the thrust in combination with atmospheric parameters dictate the power required from the electric motor, converter and the finally the power management system. Before knowing the amount of battery power that is required, the throttle needs to be processed. This is in contrast with some of the approaches that can be found in the literature, since they make use of a hybridisation factor that is based on the power split at the power management unit. In principle, exactly the same physical result can be achieved, but the proposed approach has certain benefits in terms of modelling. The throttle is defined as a fraction of the maximum power output at a certain altitude, and is predefined in the mission. Therefore, at each moment in time, the fuel consumption can be calculated, the performance of the generator, and also the amount of power delivered to the power management system. The sum of this power and the power from the batteries need to equal the amount of power requested by the power management system.

In the next sections, the details of all individual components will be discussed.

2.5.1. Propeller

The main function of the propeller is converting rotational power from a shaft into a propulsive thrust force. It does so by creating a pressure difference between the forward and rear surface of an airfoil-shaped blade causing air to accelerate. The propulsive thrust force is required to be able to perform the mission, i.e. overcome drag, accelerate and gain altitude. Unfortunately, the process of creating the momentum change is not without its losses. Therefore, besides producing the required amount of thrust, it is of importance that the associated losses are minimized. To understand more about the propeller, and ways to model these losses, the most important aspects of the propeller are discussed:

- **Propulsive power**: the rate of useful work performed by the propeller.
- **Thrust**: the change in momentum due to the pressure difference created by the rotating airfoils.
- **Propulsive efficiency**: the fraction of power delivered by the shaft that is converted into useful propulsive power.

The propeller performance depend on many different factors, such as free stream velocity, rotational velocity, propeller diameter, number of blades, and more. To reduce the complexity of the performance maps, three different dimensionless coefficients are introduced, see Equation 2.21. The advance ratio (J) relates the rotational speed and propeller diameter to the free stream airspeed. Effectively, the angle of attack experienced by the rotor blades are made proportional to the advance ratio. The underlying assumption that makes the advance ratio such a powerful coefficient is that the propeller performance is mainly a function of angle of attack. Consequently, it is possible to create one performance map as function of advance ratio that can be used over a wide range of velocities and rotational speeds. It must be noted however, that the effect of a varying Reynolds number is neglected when using only one performance map.

Furthermore, the power (C_P) and thrust (C_T) coefficients relate the diameter, rotational speed, and density

to the amount of shaft power required and thrust produced. The three coefficients together can be used to determine the propeller efficiency, as shown in Equation 2.22. The thrust and power coefficients are a function of propeller design - e.g. chord length distribution along the blades, blade angles, airfoil shapes -, Reynolds number, Mach number, and advance ratio. Because the reference propeller uses a variable blade pitch mechanism, for each advance ratio, a whole range of power and thrust coefficients can be obtained. Once the power and thrust coefficients are determined for each operating point, the propeller performance is known and can be used in conceptual design. It is important to emphasize the dependency of efficiency on density, airspeed, and rotational velocity. In section 2.8.1, the interaction effects between the aerodynamics, the propeller, and the electric motor will be elaborated on.

$$ J = \frac{V_\infty}{nD_P} \qquad\qquad C_T = \frac{T}{\rho_\infty n^2 D_P^4} \qquad\qquad C_P = \frac{P_{shaft}}{\rho_\infty n^3 D_P^5} \qquad (2.21) $$

$$ \eta = \frac{P_{prop}}{P_{shaft}} = \frac{C_T}{C_P} J \qquad (2.22) $$

There are various analyses methods available to determine propeller performance. An overview of the most important methods are presented below.

- The **Integral Momentum Theorem** departs from the basic notion that thrust is generated as a result of accelerating mass flow. It places a control volume around the propeller and defines a uniform in- and outflow velocity. The resulting equations from this theorem represent the most ideal efficiency since it assumes an inviscid flow with a propeller that does not introduce any rotation in the slipstream. Although it can be useful for the initial sizing of a propeller, the performance estimation is to rough to be useful for later stages in the conceptual design.
- **Blade Element Methods** are based on the assumption that each element of a propeller blade can be considered as an airfoil segment, each with its own characteristics, and that all the segments are independent of the adjoining segments. The performance of the complete propeller is obtained by integrating al the sections along the radii of the blades. Blade element models use local induced velocities as an input for their calculations. therefore, an additional model is needed. Examples of these models are: full- and simplified-momentum, lifting-line, and vortex models. Gur and Rosen [17] conclude in their comparison study that detailed and complicated methods for calculating the induced velocities do not show advantages over a simple blade-element theory combined with the actuator disk theory.
- **Empirical relations** or **Experiments** provide actual measured performance of certain propeller designs, hence are the most accurate. On the other hand, these methods are the least flexible when designing a new propeller for a specific mission.

The propeller performance is based on data obtained from Pipistrel [35]. For 21 advance ratios and 38 power coefficients, the thrust coefficients are provided. Based on this data, the performance map shown in Figure 2.18 is generated. For the same advance ratio, two different power coefficients may result in the same thrust coefficient. Of the two, the lowest power coefficient always lead to the highest efficiency. Therefore, the upper left corner of the performance map has been removed from the data points before making an interpolation model of the data. The interpolation model translates an advance ratio and a thrust coefficient to a power coefficient. It is based on a two dimensional polynomial of the fifth order, resulting in a fit with a coefficient of determination (R^2) of 0.999.
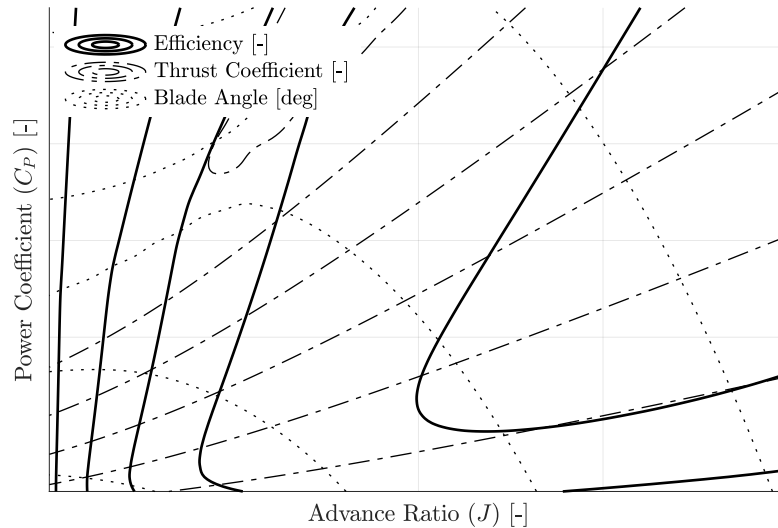
Figure 2.18: Propeller performance map, efficiency and thrust coefficient are plotted versus advance ratio and power coefficient. Both contour plots are based on 798 datapoints each, obtained from Pipistrel [35].

2.5.2. Electric Motor and Generator

The electric motor is a power transformation device which converts electrical power into rotational shaft power that is used to rotate the propeller. The operating principle of an electric motor lies in the interaction between one or more magnetic fields and/or currents going through these fields. The Lorentz Force law states that a particle of charge q moving with velocity $\mathbf{v}$ in the presence of an electric field $\mathbf{E}$ and a magnetic field $\mathbf{B}$ experiences a force $\mathbf{F}$. When placing a current-carrying wire in a magnetic field, each of the moving charges in the wire experiences this force which combined can create a substantial force in the wire. The general law can be rewritten for a wire specifically, resulting in Equation 2.23, where $\mathbf{J}$ is the current density.

$$\mathbf{F} = \mathbf{J} \times \mathbf{B} \tag{2.23}$$

The force produced in the wire is used to create torque, which rotates a rotor in the electric motor and thereby generating shaft power. The amount of shaft power can thus be manipulated in two ways: either by changing the current density through the wires or by changing the strength of the magnetic field.

Modeling of Losses in an Electric Motor

As always, there are losses associated with the power conversion in the electric motor. The general equation for the conversion of electrical power in the electric motor is shown in Equation (2.24).

$$P_{el} = P_{shaft} + P_{loss} \quad \rightarrow \quad UI = \omega Q + P_{loss} \tag{2.24}$$

First and foremost, a method must be found that models the power loss of the electric motor over its operating range. Secondly, a relation needs to be found that translates any combination of current and voltage to rotational speed and torque. Based on the operating principles, the main categories of losses have been identified:

- **Friction losses** are attributed to the force that it takes to overcome the drag associated with rotating the motor's rotor. For example, the friction of bearings, bushings or brushes. In general, the frictional losses

are proportional to the rotor speed.

- **Windage losses** are caused by turbulence in air-cooled motors. They are linked to the rotor speed.
- **Iron losses** are associated with the magnetic paths of the motor.
- **Ohmic losses** are due to the resistance in conductors through which the currents are flowing. These losses are equal to the square of the current times the resistance of the path through which the current flows.

One can model the performance of electric motors with various fidelities; For example by using simple one dimensional relations between power and efficiency, or detailed models in which all the individual loss effects are taken into account as function of design parameters such as the number of windings in a coil. Models that describe the losses as function of design parameters require, unsurprisingly, a lot of design details. In Schoemann and Hornung [43], this approach is followed for a brushed motor using a simplified circuit model. Each simplification sacrifices model accuracy. For the current motor, the required design details are not known, making it impossible to take this approach. The opposite is done by Hung and Gonzalez [19]; They use a look-up table to interpolate between measurement data of an existing motor.

In the current thesis work, the model presented by McDonald [26] will be used. It describes the power loss as a function of the rotational speed and torque, as can be seen in equation 2.25. The coefficients C_i are determined using Equation 2.26 where, k_0 is a constant to tune the model for a better fit, $\hat{\omega}$ the rotational speed at maximum efficiency, $\hat{Q}$ the torque at maximum efficiency, and $\hat{\eta}$ the maximum efficiency. This approach is more generic compared to a look-up table since the complete efficiency map is determined by three parameters.

$$P_{loss} = C_0 + C_1\omega + C_2\omega^3 + C_3Q^2 \tag{2.25}$$

$$C_0 = k_0 \frac{\hat{\omega}\hat{Q}\left(1-\hat{\eta}\right)}{6\hat{\eta}} \qquad C_1 = \frac{-3C_0}{2\hat{\omega}} + \frac{\hat{Q}\left(1-\hat{\eta}\right)}{4\hat{\eta}} \qquad C_2 = \frac{C_0}{2\hat{\omega}^3} + \frac{\hat{Q}\left(1-\hat{\eta}\right)}{4\hat{\eta}\hat{\omega}^2} \qquad C_3 = \frac{\hat{\omega}\left(1-\hat{\eta}\right)}{2\hat{Q}\hat{\eta}} \tag{2.26}$$

One of the limitations of the proposed model compared to a detailed model that takes design changes into account, is that the effect of changes in optimal rotational velocity on the maximum efficiency cannot be predicted. Also, the influence of scaling effects on the maximum efficiency and its point in the performance map cannot be modeled. Therefore, when performing a study including the influence of scaling effects on the electric motor performance, these effects should be predicted using different methods.

Performance of Current Electric Motor

The current electric motor that is installed in the Panthera is a motor specifically designed by Siemens, with a maximum power output of 200 kW. The main characteristics are presented in Table 2.6. In total, 16 data points describing the performance of the electric motor used in the Panthera are made available. The data point with the highest efficiency has been used to calibrate the model and calculate the appropriate coefficients. Both the data points and the contour lines of the model are shown in Figure 2.19. In the region where data points are available, $\omega > 500$ and $Q > 100$, the coefficient of determination (R^2) is 0.75 and the root mean square error $RMSE$ is 1.3 %. At this level, the error is deemed reasonable. Furthermore, it is logical that the efficiency goes to zero when either the torque or rotational speed goes to zero as no useful power is produced.

Using the aforementioned performance model, it is possible to map the desired output power via the efficiency to the required input power. However, by only using Equation 2.25, it is not possible to find which input combination of current and voltage leads to a certain torque and rpm. The relation between input current and output torque is determined by the torque-coefficient. Using the data-points, it has been determined that

Table 2.6: Main characteristics of the electric motor

	Symbol	Value	Unit
Maximum power output	P_{max}	200	kW
Maximum rotational speed	ω_{max}	2250	RPM
Maximum torque	Q_{max}	850	Nm
Maximum efficiency	η_{max}	96	%
Rotational speed @ η_{max}	$\omega_{\eta_{max}}$	2250	RPM
Torque @ η_{max}	$Q_{\eta_{max}}$	400	Nm
Total mass	m_{EM}	43.31	kg

$I = 0.72Q$ with a $RMSE$ of 6 Nm.
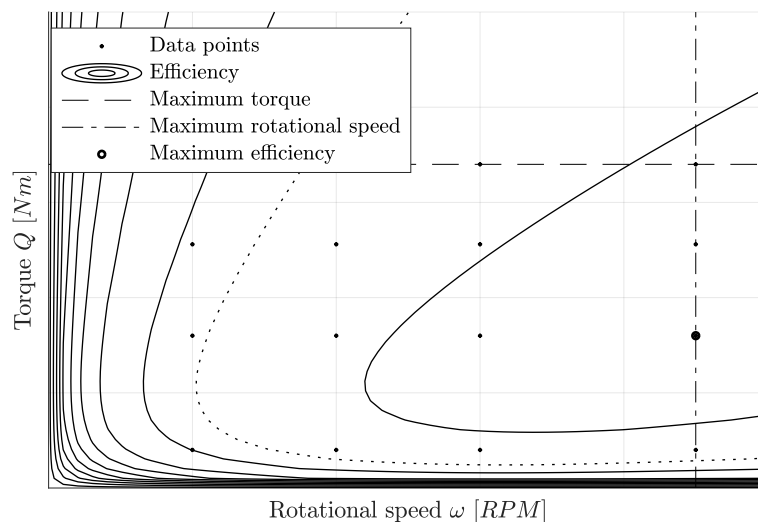
Figure 2.19: Electric motor performance map

Generator

The generator to which the internal combustion engine is connected, is in principle an electric motor. Instead of converting electric power to shaft power the opposite takes place: shaft power is converted to electric power. Based on a certain torque and rotational speed, using the aforementioned electric motor model, the electric output power can be determined. In constrast to the electric motor, the shaft power is always higher than the electrical power. The generator used in the Panthera is developed by Siemens [44], and has a maximum efficiency of 95 % at a rotational shaft speed of 5500 RPM and a torque of 250 Nm.

Scaling the Electric Motor

To enable a fully flexible power loading in the design routine, it is desired to add the maximum output power of the electric to the design variables. By doing so, the maximum takeoff weight can be increased to carry more batteries for example, or it can be decreased when a lighter aircraft is desired that has no problem satisfying the takeoff requirements. In this thesis work, the assumption has been made that any increase in maximum power is the result of a design change that allows for higher currents and consequently higher torques. Also, it is

assumed that the efficiency map remains unchanged as a result of this modification. When scaling the electric motor this way, it is assumed that the specific power remains constant at 4.6 kW/kg, hence the weight of the motor is affected.

2.5.3. Internal Combustion Engine

The internal combustion engine in the current Panthera is the *OM914* Rotax engine, Rotax [41]. This is a turbo-charged engine delivering up to 84 kW at 5800 RPM for a maximum of 5 minutes and up to 73 kW at 5500 RPM continuously. With a dry weight of approximately 78 kg, it has a specific power of 1.08 kW/kg. This is significantly lower compared to the electric motor that is installed. The performance data recorded of the *OM914* relates the rotational shaft speed and fuel consumption to the output power for continuous and takeoff operation. Furthermore, the power lapse as a function of altitude and temperature difference is given. The *OM914* runs on Avgas, which has a density of 720 kg/m^3 and a lower heating value of 44 MJ/kg. The performance for continuous operation is shown in Figure 2.20.
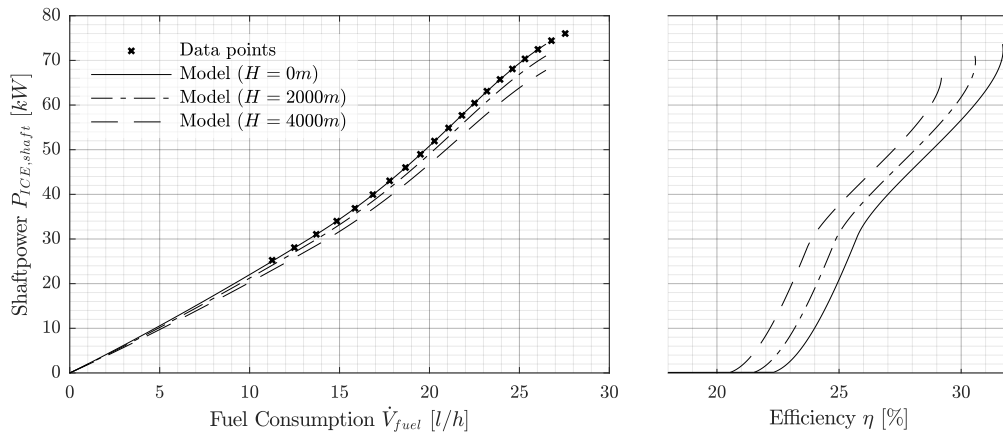
Figure 2.20: Performance data of the *OM914* Rotax engine, including power lapse effect. Data points are obtained by interpolating between two sets of data from Rotax [41]: one RPM - power, and one RPM - fuel flow.

It is assumed that the power lapse decreases the amount of power at every point of operation equally. Therefore, the complete shaft power curve can be shifted downwards over the given range of rotational speeds or fuel consumption. As can be seen, the efficiency is affected consequently.

When scaling the internal combustion engine, it is assumed that the efficiency relative to the throttle setting remains constant. This way the complete performance of a resized internal combustion engine can be calculated after multiplying the shaft power with a simple scaling factor. Again, a constant specific power of 1.08 kW/kg is assumed for the weight estimation.

2.5.4. Battery Module

One of the key components in hybrid-electric aircraft is the battery. Its function is to store energy in chemicals and convert this into electrical power when demanded. When connected to an electrical device, energy is released through a chemical reaction. Engineers who are mainly concerned with the early stages of conceptual design are not necessarily interested in the detailed characteristics of a battery. The first question of interest is: how much will the batteries weigh when capable of delivering a certain power profile? Secondly: how much volume will those batteries occupy? Since the performance of a battery depends on the discharge power profile,

one cannot simply translate amount of energy required to battery capacity. Therefore, in later stages of the design, a model needs to be found to model the battery performance with good accuracy. In this section, the model to determine the point-performance of batteries will be presented. Section 2.8.2 will use this model to analyse the complete power profile and determine the minimal required capacity. But first, the operating principles of batteries will be presented.

Background and Modeling

Batteries operate on the principle of reduction-oxidation reactions (REDOX), see Equation 2.27, which cause the oxidation state of atoms to be changed. By connecting two separate terminals by a conductor, a flow of electrons is induced as a result of these REDOX reactions. The conversion of chemical energy to useful electrical energy is not without its losses. According to Chen and Rincon-Mora [3], the available battery models can be divided into three major categories: electro-chemical, mathematical, and electrical-equivalent models. Each model has its advantages, disadvantages, level of accuracy, and ability to capture certain behaviour for specific purposes.

$$a\mathbf{A} + ne \rightleftarrows b\mathbf{B} \qquad\qquad c\mathbf{C} - ne \rightleftarrows d\mathbf{D} \qquad\qquad (2.27)$$

- **Electro-chemical models** are mainly used to optimize the physical design aspects of batteries and relate the macroscopic parameters (voltage and current) with the microscopic aspects (distribution and choice of chemicals). These models are very time-consuming since they involve a lot of physics-based time-dependent equations and they require very detailed battery information which are difficult to obtain. Therefore, they are not very useful for a conceptual aircraft designer.
- **Mathematical models** are too abstract to embody any practical meaning and mostly useful for system designers. Also, they cannot provide any I-V information which is essential for circuit simulation and optimization. Most mathematical models work for specific applications and can provide results with an error in the order of $5-10$ %. The maximum error of Peukert's law can be more than 100 % for time-variant loads. Furthermore, Doerffel and Sharkh [5] concluded in their critical review of using the Peukert's equation for determining the remaining capacity of lithium-ion batteries that the Peukert's law can only be used under constant operating temperatures and discharge currents.
- **Electrical-equivalent models** make use of a combination of voltage sources, resistor and capacitors to model the behaviour of batteries. The accuracy of these electrical models lie between the previously mentioned 2 models and have an error of around $1-5\%$. Electrical models are more intuitive, useful and easy to handle, especially when using the battery model alongside other electrical systems.

Chosen Electrical-Equivalent Model

The electrical-equivalent models are best suited for modeling battery behavior in aircraft design. They are accurate, but not too complex. In Chen and Rincon-Mora [3], three well-known electrical-equivalent models are discussed: Thevenin, impedance, and runtime-based models. By adding different components, such as as capacitors and resistances, the accuracy of the model can be increased. At this level, however, no transient loads, temperature effects, or self-discharge effects are taken into account. Therefore, the three different electrical-equivalent models can be reduced to the model as shown in Figure 2.21.

The electrical potential difference, also referred to as open-circuit voltage U_{OC}, is a function of the difference in chemical potential of the two terminals. The open-circuit voltage varies with state-of-charge of the battery, but is assumed to be independent of discharge rate. The function for open-circuit voltage, see Equation 2.28, is
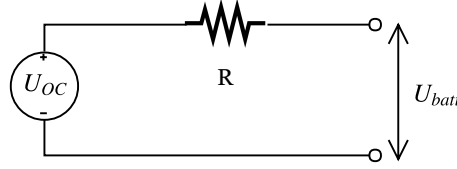
Figure 2.21: Electrical equivalent battery model using an open-current voltage source and a resistance to model the battery voltage. Based on Chen and Rincon-Mora [3]

taken from Weng, Sun, and Peng [49] for its ability to accurately fit lithium-polymer batteries. The influence of current flowing from one terminal to another on the actual useful battery voltage needs to be captured in the resistance. The formula to model the resistance, shown in Equation 2.29, is taken from Chen and Rincon-Mora [3].

$$U_{OC}(SOC) = K_0 + \frac{K_1}{1 + e^{\alpha_1(SOC-\beta_1)}} + \frac{K_2}{1 + e^{\alpha_2(SOC-\beta_2)}} + \frac{K_3}{1 + e^{\alpha_3(SOC-1)}} + \frac{K_4}{1 + e^{\alpha_4 SOC}} + K_5 SOC \quad (2.28)$$

$$R(SOC) = \frac{K_6 e^{K_7 \cdot SOC} + K_8}{Q} \quad (2.29)$$

There are in total 16 coefficients (K_{0-8}, α_{1-4}, β_{1-2} and the total ideal capacity) that determine the performance of a battery. When they are known, Equations 2.28 and 2.29 can be used to model the battery performance. The battery voltage follows from $U_{batt} = U_{OC} - I \cdot R$, the useful battery power from $U_{batt} \cdot I$, and the power loss from $I^2 R$. By integrating the battery performance over a state of charge range from one to zero, a battery discharge curve can be obtained. For most batteries, such a curve exist. By using a search algorithm, the error between the model and the measured battery performance can be minimised. The algorithm starts with a guess in terms of ideal capacity and the initial values for the 16 coefficients, after which the characteristic discharge curve is made. It changes the ideal capacity and the value of the coefficients such that the best fit, i.e. the lowest sum of errors, is obtained.

Actual Battery and Fitting the Model

In the hybrid Panthera, lithium-polymer battery cells with rated capacities of 110 Ah (0.407 kWh) and a specific energy of 180 Wh/kg from Kokam [22] are used. After packing the cells into a battery module, the specific energy is found to be 130 Wh/kg. In Figure 2.22, the measured battery cell data and the obtained model fit are presented. The data is provided for discharge rates of 0.5C, 1C, 2C, and 3C (where $1C = 100A$). As can be seen, the experimental discharge curves of 1-3C reach the same total drained capacity. When using the proposed model, without any temperature effects and with a one-parameter open circuit voltage and resistance model, it is not possible to obtain the same drained capacity for different discharge currents. A possible explanation could be that a rise in internal temperature during discharge changes the rate of the chemical reactions, and thereby changing the battery performance characteristics. The curves of the fitted model are shown in Figure 2.22 as well. The *RMS*-error in terms of relative capacity between the model and data from Table 2.7 is 2.3%, which is acceptable.

With the application in this thesis in mind, there are a number of advantages of using the presented battery model. Since the model is based on an electrical-equivalent model, it makes use of simple formulas for an accurate estimation. This means that only little computational resources are required to solve the equations. Also, the influence of discharge rate and state of charge are taken into account in the model when determining the efficiency, which is important for the high power demand during takeoff and the emergency climb with an
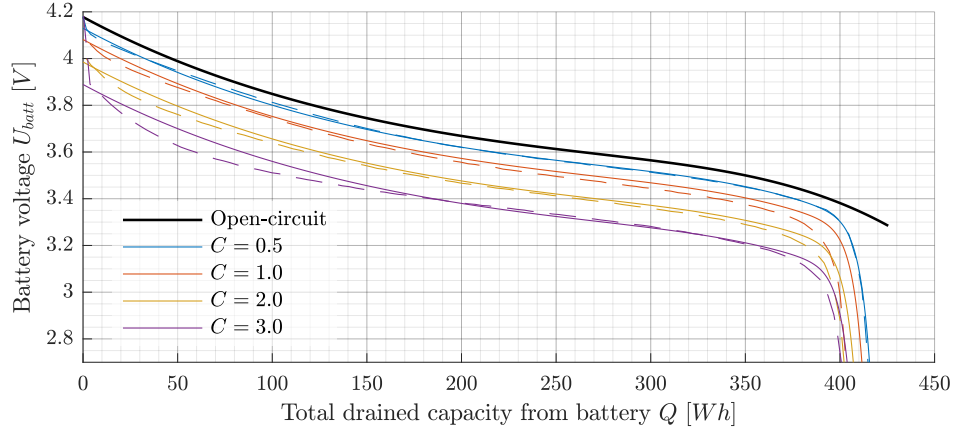
Figure 2.22: Battery discharge curves for various C-rates. The solid lines (——) represent the model and the dashed lines
(— — —) represent measured data of the Kokam battery. For battery details, see Kokam [22].

Table 2.7: Electrical performance of Kokam battery (model: SLPB70460330, Kokam [22]) versus fitted model at various discharge
rates

Discharge Rate $\frac{d}{dt}(SOC)\left[h^{-1}\right]$	0.5	1	2	3
Relative Capacity (Data)	100%	>95%	>90%	>85%
Relative Capacity (Model)	0.96%	94%	91%	87%

almost-empty battery. Furthermore, since the total capacity is included in the resistance formula, the battery
model scales with capacity. This is analog to performing calculations with C-rates only instead of actual cur-
rents. During the various optimization cases, the capacity varies between approximately 20 kWh and 70 kWh.
Consequently, a certain power demand from different batteries lead to different C-rates and thus to different
efficiencies with the same model.

The actual current that needs to be drawn from the battery to arrive at a certain power can be calculated by
solving Equation 2.30 using the quadratic formula. In case there is no real solution to the quadratic formula, the
demanded power cannot be delivered and the discriminant is set to zero.

$$R \cdot I^2 - U_{OC} I + P_{batt} = 0 \tag{2.30}$$

Regarding the point performance of the particular cell used in the Panthera, there are a few constraints. First
of all, the state of charge can never be lower than zero or higher than one. To prevent damage, the battery is
designed such that the state of charge at the end of the sizing mission is at least 15%. Furthermore, the battery
is sized such that the minimum battery voltage is always above the cutoff voltage of 2.7 V. Lastly, the battery
voltage can never be higher than the maximum cell voltage of 4.2 V. The sizing module will be elaborated on in
Section 2.8.2.

Battery Efficiency During Discharge
As battery efficiency depends on state of charge and discharge rate, it is impossible to create one simple formula
that translates power demand to efficiency irrespective of time. To gain more insight, the influence of discharge
rate and state of charge on battery efficiency is shown in Figure 2.23.

As can be seen, the battery efficiency drops with both an increasing discharge rate and a decreasing state
of charge. After a state of charge of around 10% the efficiency drops significantly. This area will never be used
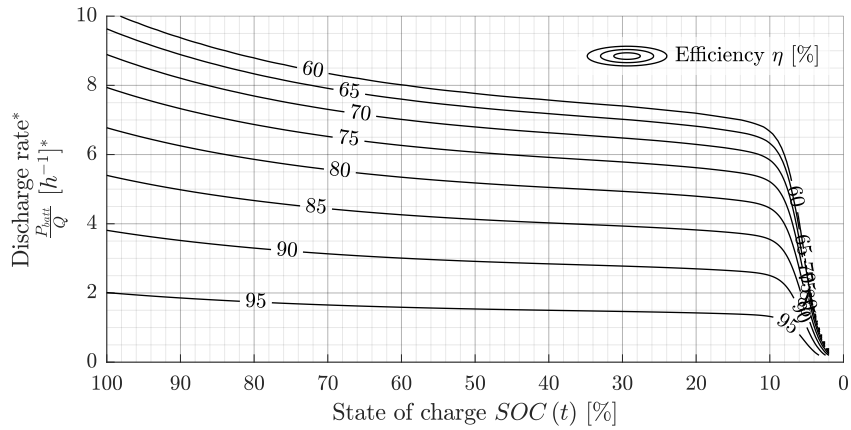
Figure 2.23: Battery efficiency for different discharge rates and states of charge
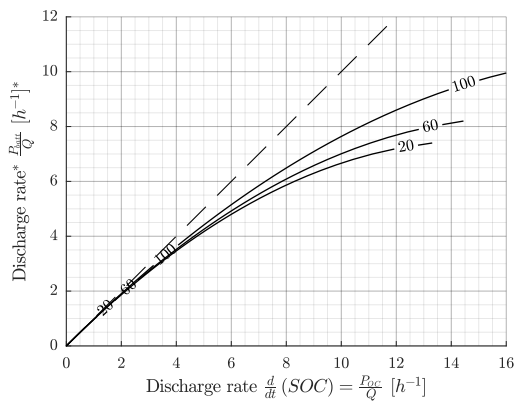
Figure 2.24: Comparison between two different interpretations of discharge rate, one using the open-circuit power P_{OC} and the other using the useful battery power P_{batt}. Each line is labeled with the corresponding state of charge SOC. The dashed line ($- - -$) indicates $y = x$.
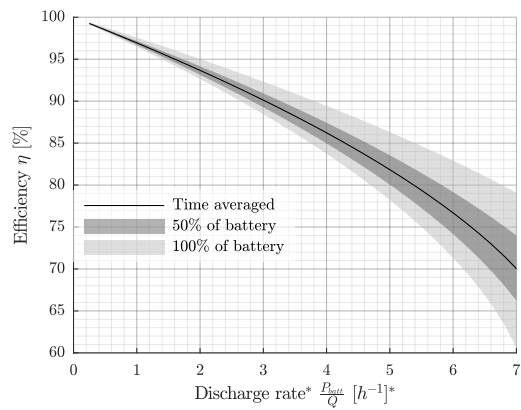
Figure 2.25: Efficiencies as a result of useful discharge rate

however as minimal state of charge is always higher than 15%. It must be noted that the discharge rate in this figure is defined as the useful power that can be extracted from the battery over the battery capacity. Due to internal losses the actual discharge rate is higher, as can be seen in Figure 2.24. Here, the actual discharge rate is shown on the x-axis.

When averaging the efficiency for certain discharge rates over the states of charge from 100% to 15% a time-averaged efficiency is obtained, as shown in Figure 2.25. The time-averaged relation as function of discharge rate is non-linear in nature due to the internal power losses. Furthermore, the areas of efficiencies in which 50% and 100% of the battery operates are indicated. As can be seen, the error in battery efficiency is relatively small for low discharge rates but increases significantly with discharge rate. The area above the time-averaged corresponds to states of charge larger than the average and vise versa. As the power demand from the batteries during the mission profile is not constant, errors are bound to be made.

Effect of Maximum Discharge Rate on Gravimetric Energy Density

Discharging batteries at high rates leads to, among other things, significant heat generation in the cell. Batteries capable of high discharge rates are due to extra required materials generally heavier. Therefore, besides the gravimetric energy density, the maximum specific power is a useful metric to compare batteries. By dividing the specific power by the energy density the discharge rate of a cell can be calculated. In Figure 2.26 the maximum discharge rates of various battery cells are shown against their gravimetric energy density. The marker sizes are relative to the cell capacity. Furthermore, data from a Ragone plot from *SAFT* [47] is used to create the trend lines for different battery chemistries, focusing on either high power or high energy. As can be seen, the high power cells from Kokam are generally capable of higher discharge rates but have a lower energy density. The trend lines that are obtained from the Ragone plot show good resemblance with the data points.
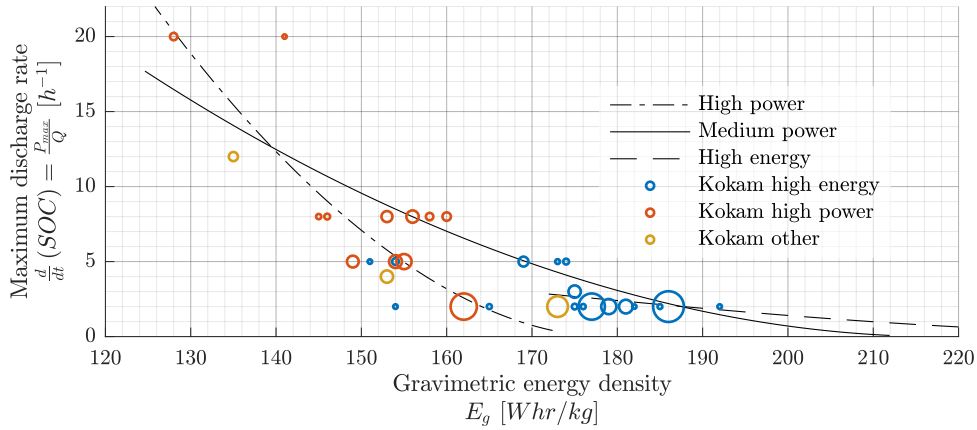
Figure 2.26: Comparison of various batteries in terms of maximum discharge rate and gravimetric energy density. The marker sizes are relative to the cell capacity. The trend lines are obtained from a Ragone plot from *SAFT* [47], and adjusted with the historical rate of battery improvement of 8% per year.

As can be seen, around an energy density of 160 Whr/kg, there is a wide range of maximum discharge rates possible. Therefore, for this thesis, a fixed energy density is assumed. For further research however, it is recommended to include the effect of maximum discharge rate on energy density. Also, the effect of different cell chemistries on life-cycle cost should be included.

2.5.5. Recharging During Flight

One of the variables that one can play with to change the hybridization in terms of power is the throttle of the internal combustion engine. The batteries are being recharged when the internal combustion engine, in combination with the generator and converter, produce more power than required for flight by the power management and distribution system. Logically, some of the this excess power gets lost due to inefficiencies along the path of the charge/discharge round trip. To measure whether or not it is beneficial to recharge the batteries, the definition from Equation 2.31 has been produced. In this equation, η_{ICE^*} is the efficiency of the power conversion from fuel power to PMAD, P_{ICE^*} is the power that is delivered from fuel to the PMAD, P_{PMAD} is the power that is required by the PMAD for flight, and lastly η_{batt^*} is the efficiency of the charge/discharge round trip of the excess power.

$$\eta_{eff} = \eta_{ICE^*} \frac{P_{PMAD}\left(1 - \eta_{batt^*}\right) + P_{ICE^*}\eta_{batt^*}}{P_{ICE^*}} \tag{2.31}$$

Since η_{ICE^*} depends on P_{ICE^*}, it is difficult to visualize the implications for this particular engine. Therefore,

the effective efficiency of the power conversion from fuel to useful power is shown in Figure 2.27 for a wide range of required powers P_{PMAD} and delivered powers P_{ICE^*}, assuming a battery round trip efficiency η_{batt^*} of 85%.
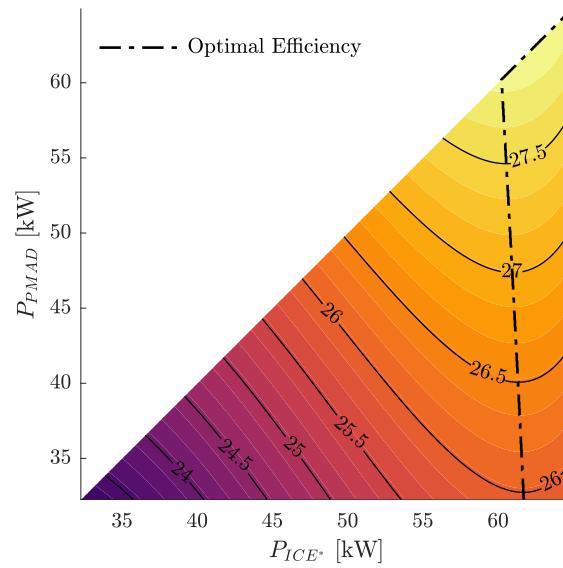
Figure 2.27: Effective efficiency of the power conversion from fuel to the power management system, including the charge/discharge cycle. A constant charge/discharge round trip efficiency of 85% is assumed.

As indicated in said figure, for every required power there is, a certain amount of power that should be delivered via the internal combustion engine to ensure maximum effective efficiency. Hypothetically, if the round trip efficiency of the battery is 100%, it is always most efficient to operate the internal combustion engine at its optimal throttle: 97.2% for the OM914. On the other hand, if this efficiency is 0%, then all the excess power gets lost and consequently the best strategy is to produce just the required amount of power. To investigate this, the optimal excess power, optimal throttle of the internal combustion engine, and corresponding effective efficiency is plotted in Figure 2.28 versus the actual power demand for batteries with a charge/discharge round trip efficiency of 75%, 85%, and 95%.

As can be seen, the round trip efficiency of the batteries has a large influence on the optimal throttle setting of the internal combustion engine. The optimal throttle of batteries with a round trip efficiency of 95% lies very close to the most optimal throttle of the internal combustion engine. The optimal throttle at a given required power decreases when the round trip efficiency decreases. Furthermore, there is certain point at which it is not beneficial to produce more power than required. The power region where no excess power should be generated increases for decreasing round trip efficiency. For required powers that fall outside this region, the optimal throttle for a given round trip efficiency increases with an decreasing amount of required power.

In conclusion, a strategy in which batteries are charged with excess power has the potential to increase the effective efficiency of the power conversion chain from fuel to useful power. The round trip efficiency of the batteries highly influences the optimal throttle setting of the internal combustion engine. If the round trip efficiency is 95% and the required throttle during cruise is only 50%, the increase in effective efficiency is 4%. However, if the required throttle during cruise is 80%, this increase in effective efficiency drops to about 0.9%. It must be noted that this corresponds to an internal combustion engine that is able to produce 20% more power than required. Another opportunity to increase the overall efficiency of aircraft lies in the downsizing of the internal combustion engine in such cases. It could be that the benefits of a 20% less powerful, and hence lighter,
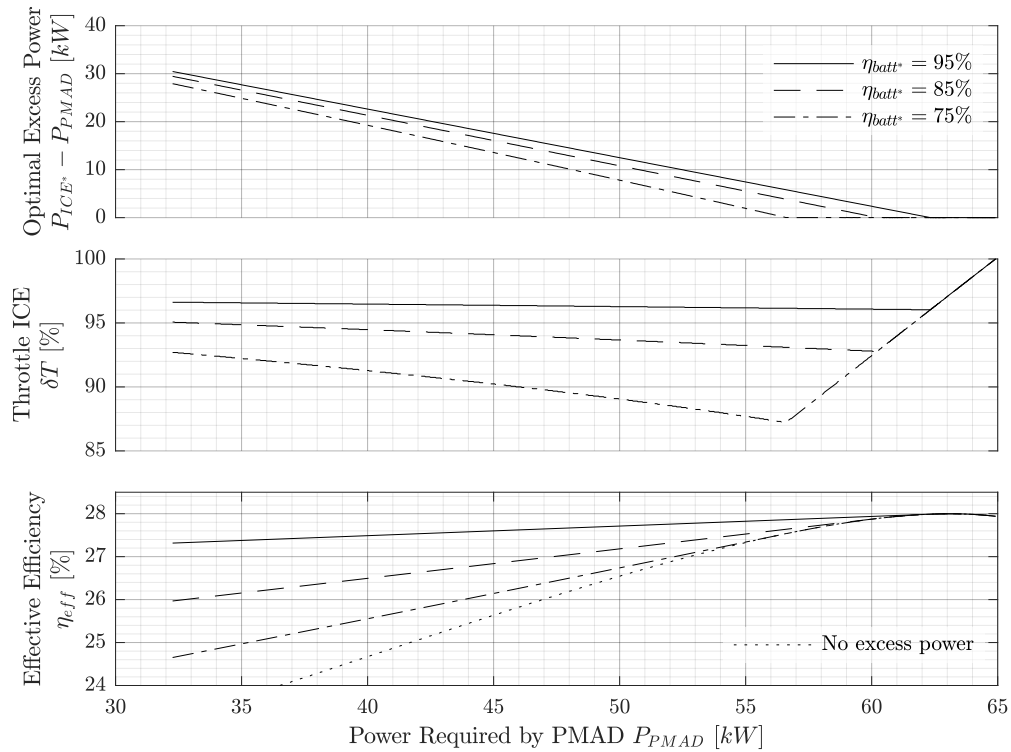
Figure 2.28: Comparison of optimal excess power, optimal throttle of the internal combustion engine, and corresponding effective efficiency between three batteries with different assumed charge/discharge round trip efficiencies for various actual power demands

engine outweigh the effect a smaller engine has on its overall efficiency.

2.6. Flight and Mission Analysis

In this section, it is explained how the flight mechanics equations are solved for the whole mission, resulting in thrust requirements for the propulsion system. The magnitude of the determined thrust at each moment during the mission is important since it determines the size of the propulsion components and the amount of energy required for flight.

Mission Segments

Depending on the purpose of an aircraft, and the intended certification specifications, a mission profile needs to be selected. This mission should be representative for the envisioned use of the aircraft, since it strongly determines the aircraft design. Because the objective of this thesis is not necessarily flight path optimisation, a mission profile has been build up using relatively simple flight segments, as shown in Figure 2.29.

Each segment is represented by an array of data points containing the required information to perform a detailed analysis; E.g. the duration of the particular segment, airspeed, altitude, rate of climb, configuration information such as landing gear deployment and flap deflection, aircraft weight, a flag indicating whether the segment should be included in the performance analysis or not, and a segment ID. All the segments sharing the same ID need to be continuously connected to each other, and hence the various properties interpolated. By concatenating all the arrays of data points, the complete mission profile is obtained. Figure 2.30 shows the
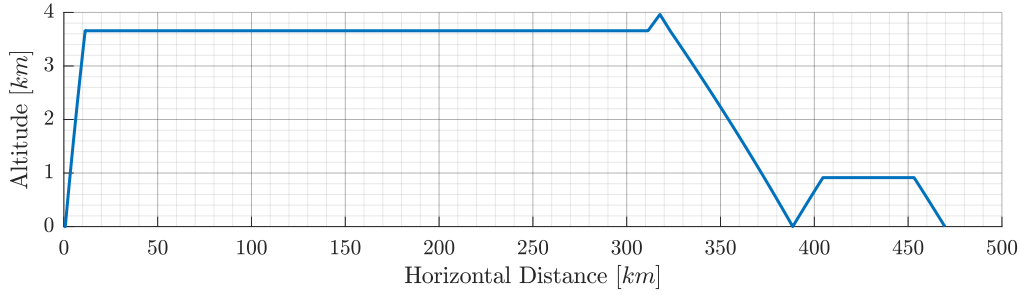
Figure 2.29: Mission profile for a range of 300 km, including the safety segments.
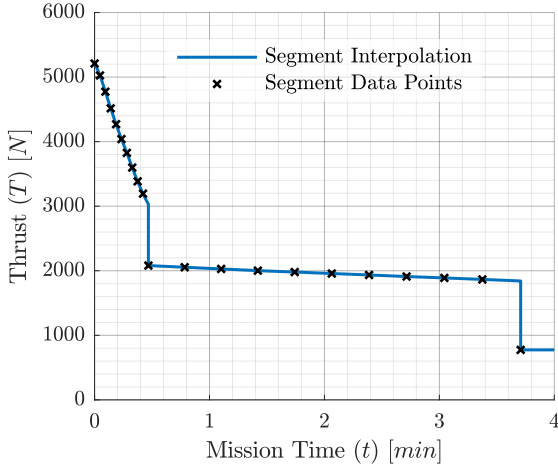
Figure 2.30: Segment data points of the takeoff, climb, and the beginning of cruise with segment interpolation.
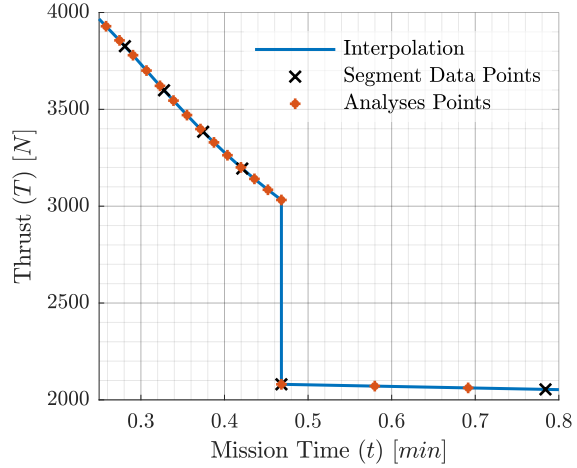
Figure 2.31: Coarse segment data points and finer analyses points.

thrust values of the data points and their interpolation. In Figure 2.31 an even smaller part of the mission is shown including the analyses points, which are used to for example determine the amount of fuel that is used.

Mission Analysis

The amount of thrust required at any moment in the mission is the sum of three terms: The drag, a term related to the change in potential energy, and a term related to the change in kinetic energy, as shown in Equation 2.32. In this section, the specific details of all segments are presented.

$$T = D + \frac{RoC \cdot W}{V} + m \cdot a \tag{2.32}$$

Takeoff   During takeoff, the maximum power is used to be airborne as quick as possible. The starting point of the takeoff analysis is a stationary aircraft with zero velocity, zero lift, and maximum thrust. For velocities lower than the stall speed, the maximum lift coefficient and the corresponding drag coefficient is assumed. While the aircraft is in contact with the ground, the friction drag that is produced at the wheels need to be added to the aerodynamic drag. The formula for friction drag is shown in Equation 2.33. It is assumed that the surface type is wet grass, the worst case scenario following Gudmundsson [16, Sec. 17.2.1]. The corresponding ground friction coefficient μ is 0.08

A lookup table is generated that translates velocity into net force, not taking acceleration into account. Using this, the maximum acceleration can be calculated extremely quick for all velocities. This is numerically inte-

grated until the climb velocity is reached, resulting in a takeoff velocity, time, and distance profile.

$$F_{wheel} = \mu (W - L) \tag{2.33}$$

Climb The climb from takeoff to cruise has only one requirement: the flight-path angle needs to be larger than 4.7 degrees. Any combination of rate of climb and velocity that satisfies this constraint is a viable option. Because the variation in velocity during climb is very small, the contribution due to acceleration in Equation 2.32 is neglected. Hence, the energy during climb is either dissipated via the mechanism of drag, or converted into potential energy. Climbing at a maximum rate of climb reduces the time to climb, and thereby minimises the energy dissipation through drag.

Using the lift-drag polar and the propulsion performance relations, the maximum rate of climb can be calculated for any altitude. By expressing the desired rate of climb as a fraction of the maximum rate of climb, see Equation 2.34, no propulsion system constraints need to be introduced to ensure feasibility. However, the minimum flight-path angle constraint is still required.

$$C_{climb} = \frac{RoC}{RoC_{max}} \tag{2.34}$$

By minimising the aerodynamic drag itself, the energy dissipated during the climb can be reduced even more. However, it is not necessarily the case that the minimum drag airspeed and the most optimal airspeed are the same. A synergistic optimum needs to be found between the aerodynamics and the propulsion components. Because the performance of the electric motor and the propeller depend on the rotational speed of the shaft and the airspeed, it can be that the optimal airspeed in terms of energy consumption is different compared to the minimum drag airspeed. On average, the optimal airspeed during climb is 1.5 m/s higher than the minimum drag airspeed. This is expected since the propeller was designed for much higher airspeeds.

Cruise For the cruise analysis, Equation 2.32 reduces to $T = D$ since the rate of climb is zero and the velocity is constant. The required amount of thrust can be determined directly because the drag is a function of the cruise speed, which is a top-level requirement. Therefore, the only variable left is the hybridisation factor, which can be approached from different ways.

One approach is to define a constant power split for the cruise. By varying the power spilt, one can move from full electric, via hybrid to a full internal combustion engine power setting. The advantages of this approach are its simplicity and the fact that the internal combustion engine and the batteries are fully decoupled and do not need to exchange information with each other. However, there is one significant downside: not all power splits are necessarily feasible. For example, if the power required for cruise is higher than the maximum power that can be delivered by the internal combustion engine, a power split exists that results in an infeasible power demand.

Alternatively, the hybridisation of the cruise phase can be approached from the internal combustion engine: By varying the engine its throttle from 0 to 100 percent, all the feasible power splits from the first approach can obtained. This can be seen in Equation 2.35. Because the constraints are captured in the parametrisation, any hybridisation factor is inherently feasible. The power demand of the power management and distribution (PMAD) module is dictated by the required thrust and the performance of the propeller and electric motor combination. The maximum power that can be delivered to the PMAD via the combustion power path can be determined numerically since the performance of all the components in this chain are known. The power required from the electrical power path is known once a certain throttle has been selected. If there is excess power

from the combustion chain, power is supplied to the electrical power chain. In this case, the batteries are being charged.

$$P_{PMAD} = P_{elec} + \delta_T P_{ICE_{max}} \cdot \eta_{gen}\eta_{conv} \qquad \text{where} \quad \delta_T = \frac{P_{ICE}}{P_{ICE_{max}}} \qquad (2.35)$$

The two approaches solve exactly the same problem: the power split between the electrical and the combustion power path. Due to the inherent feasibility of the approach in which the engine its throttle is used, the second approach is preferable to the first one.

When the aforementioned hybridisation factor is applied to the entire cruise phase, the hybridisation in terms of energy is highly coupled to the hybridisation in terms of power. This means, prioritising battery usage can only be achieved by reducing the power delivered by the internal combustion engine. As a result, the combustion engine moves away from its most optimal operating point leading to a worse fuel economy. For this reason, a second type of hybridisation factor has been introduced: hybridisation in terms of energy.

By dividing the cruise segment into two parts, both having different hybridisation factors, the hybridisations in terms of power and energy can be decoupled. In the remainder of this thesis, hybridisation in terms of power and in terms of energy is referred to as *hybridisation* (δ_T) and *electrification* (ϵ) respectively. One of the possibilities introduced by using this electrification factor is having first a hybrid cruise segment in which the internal combustion engine runs at its most efficient operation point, followed by a full-electric phase. The larger the full-electric phase, the more battery energy is consumed during the mission. In Equation 2.36, the mathematical description of electrification is presented. Here, d_e is the distance travelled full-electric during one of the segments, and R is the total range of the cruise.

$$\varepsilon = \frac{d_e}{R} \qquad (2.36)$$

Descent   During the descent, the aircraft its potential energy can be converted into two different forms, i.e. converted to kinetic energy or dissipated through drag. When neglecting the acceleration in Equation (2.32), it leads to an apparent reduction in drag to overcome by the propeller. The approach to the descent is as follows: The airspeed, and hence the amount of drag, is determined at each altitude by the maximum L/D ratio. By setting the thrust to zero, the rate of descent is dictated by the drag.

Safety Segments   To account for potential changes to the mission profile that require more energy than ideally necessary, several safety mission segments have been included. Firstly, a short climb of 300 m is added at the end of the cruise. Secondly, a loiter segment of 15 minutes at 915 m altitude is added in case of a failed landing attempt. The airspeeds during climb and descent for the safety segments are determined by maximizing the lift-over-drag ratio. Note that in absolute terms this is changing with altitude. The rate of descent is chosen such that the propulsive power required is zero. The energy consumption during the safety segments will only be used to size the aircraft, and not taken into account in the energy consumption objective metric.

2.7. Weight Estimation
The starting point for the weight estimation is the basic empty weight of the currently existing Panthera. All the components of the aircraft that are influenced by the design variables, see Equation 2.37, need to be recalculated,

hence their initial mass is subtracted from the basic empty weight. In this section, the methods to recalculate this mass will be presented.

$$m_{MTO} = m_{basic} + m_{wing} + m_{batt} + m_{fuel} + m_{EM} + m_{ICE} + \sum_{i=1}^{3} m_{conv,i} \tag{2.37}$$

2.7.1. Wing Weight

In the literature, many empirical relations exist that estimate wing weight based on several key design parameters; e.g. Cessna, USAF, Torenbeek, Raymer, Sadraey, and Carreyette. The accuracy of the weight estimation becomes potentially higher when including more parameters, however, this is not necessarily the case. Furthermore, more information about the design is required.

Next to the purely empirical methods, one semi-analytical method has been explored: the Elham Modified Weight Estimation Technique (*EMWET*), see Elham, Rocca, and Tooren [13]. It makes use of elementary wing box sizing techniques to compute the distribution of required material to resist the applied loads, in combination with empirical methods to estimate all the other weight contributions. *EMWET* requires by far the most parameters to perform its wing weight estimation. As this method is primarily developed and validated for much larger aircraft, it cannot be assumed that its accuracy in determining the wing weight of general aviation aircraft is higher than empirical methods. In Table 2.8 the required parameters of each method that have been investigated are shown.

The wing weight of the baseline aircraft has been calculated using the aforementioned purely empirical methods, and using *EMWET*. The maximum operating condition is at $3.6 \, km$ altitude, with a velocity of $113 \, m/s$. Furthermore, the maximum loading factor is 4.4 and the ultimate loading safety-factor is 1.5. The results of the calculations using the different methods are presented in Table 2.9. Next to the wing weight, a so-called fudge factor has been calculated. When multiplying the calculated wing weight with this factor, the actual wing weight is obtained.

Torenbeek his extended method has been selected for the estimation of the wing weight for a number of reasons. The method has been developed for a wide range of aircraft, explicitly including the general aviation type. The method is based on a generalized expression for the material required to resist the root bending moment due to wing lift in a specified flight condition. By dividing the wing group weights by the span, it was found that the main controlling geometrical parameter for wing weight is the wing span. Furthermore, the standard error of prediction is 9.64%, which is found to be acceptable for this stage of the design. Raymer [38] suggests that when using carbon fiber material to construct the wing, a fudge factor of approximately 0.85 should be used, which is in good agreement with the found factor. The equations for the wing weight are shown in 2.38 and 2.39.

$$m_{wing_{basic}} = c \cdot k_{no} k_{\lambda} k_e k_{uc} k_{st} \cdot [k_b n_{ult} (W_{des} - 0.8 W_W)]^{0.55} \cdot b^{1.675} (t/c)_r^{-0.45} \cos(\Lambda_{c/2})^{-1.325} \tag{2.38}$$

$$m_{flap} = c \cdot k_f S_f (S_f b_{fs})^{3/16} \left[\left(\frac{V_{lf}}{100} \right)^2 \frac{\sin \delta_f \cos \Lambda_f}{(t/c)_f} \right]^{3/4} \tag{2.39}$$

2.7.2. Propulsion System Mass

To allow for changes in the size of the propulsion system components, the mass of the propulsion system components will be calculated each run. The size of the internal combustion engine and the electric motor are in

Table 2.8: Variable dependency of the various methods for the wing weight.

		Carreyette	Cessna	USAF	Torenbeek	Torenbeek Ext.[•]	Raymer	Sadraey	EMWET**
Maximum Takeoff Weight	W_{TO}		○	○	○	●	○		○
Fuel Weight	W_{FW}					●	○		○
Ultimate Loading Factor	n_{ult}		○	○	○	●	○	○	○
Aspect Ratio	A		○	○			○	○	○
Surface Area	S		○	○	○		○	○	○
Sweep Angle	Λ			○	○	●	○	○	○
Taper Ratio	λ			○		●	○	○	○
Maximum Wing Thickness	t/c_{max}		○	○		●	○	○	○
Velocity / Dynamic Pressure	V or q			○			○		○
Wing Span	b	○			○	●			○
Mean Aerodynamic Chord	C_{MAC}							○	○
Density	ρ_{mat}							○	○
Material Properties	K_ρ							○	○
High Lift Devices*						●			

* Multiple parameters are used to calculate this weight.
** EMWET uses more variables than presented in this table.
[•] Method of choice

Table 2.9: Results of the weight estimation

	Wing Weight $[kg]$	**Fudge Factor** [-]
Actual Wing	125	1
EMWET*	157	0.80
Cessna	328	0.38
USAF	133	0.94
Torenbeek	190	0.66
Torenbeek Ext.**	**147**	**0.85**
Raymer	145	0.86
Carreyette	240	0.52
Sadraey*	115	1.08

* Material property set to aluminum
** Method of choice

some of the runs design variables. The maximum power after scaling is multiplied with a constant gravimetric power density, as shown in Equation 2.40. The gravimetric power density of the internal combustion engine is 1.08 kW/kg and that of the electric motor is 4.63 kW/kg. Furthermore, the gravimetric power density of the converters is 12 kW/kg. The battery mass is calculated using a constant gravimetric energy density of 130 Whr/kg in Equation 2.41. The required fuel mass follows from the power requirements of the internal combustion engine, and has a gravimetric energy density of approximately 12,000 Whr/kg.

$$m_i = P_{max,i} \cdot P_{g,i} \tag{2.40}$$

$$m_{batt} = Q \cdot E_g \tag{2.41}$$

By using a constant specific energy of the battery and a constant specific power of the converter, the scale effects on the component its performance cannot be captured. For example, one would expect that the converter mass scales less than linear with the maximum power output. The same goes for the battery, however, since the actual numbers also highly depend on technology level it has been decided to fix these numbers and investigate its influence in the sensitivity study.

2.8. Sizing Module

In this section, the coupling between the electric motor, propeller, and flight mechanics will be elaborated. Furthermore, the battery sizing module is presented here.

2.8.1. Propeller, Electric Motor, and Flight Mechanics Coupling

During any given flight condition, the airplane its mass, configuration, altitude, airspeed, vertical speed, and acceleration determine the required amount of thrust that needs to be delivered by the propeller. For most of the mission, the flaps and the landing gear are retracted, hence in this section a clean configuration is assumed. For simplicity reasons, the acceleration and change in the aircraft its mass is neglected. Furthermore, the vertical speed during climb is controlled by the optimiser. Consequently, for a given altitude, the amount of thrust is fully determined by the airspeed. To determine the most efficient operation of the power train, the relations that influence the power demand are required. In Figure 2.5, the information flow of the power train up to the power management system is shown.
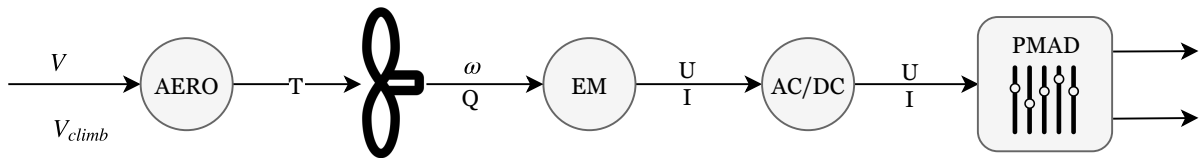
Figure 2.32

The efficiency of the *AC/DC* converter depends on the actual currents and voltages at its in- and outputs. To model this accurately, a lot of details are required about the design of the converter. Considering the scope of this thesis and the limitations in terms of resources, it has been decided to neglect this influence. It is assumed that the converter operates at a constant efficiency of 98%. Consequently, it is always preferable to minimise the amount of electrical power required by the electric motor, regardless of the optimization objective. The most important relations regarding the power demand of the drivetrain are presented in Equation 2.42. When substituting all the relations in the equation for input power for the electric motor ($P_{EM_{in}}$), it is found to be a

function of airspeed and rotational shaft speed, see Equation 2.43.

$$T = f(V) \qquad P_{req} = f(T, V) \qquad \eta_{prop} = f(V, \omega, T) \qquad \eta_{EM} = f(\omega, Q) \qquad (2.42)$$

$$P_{EM_{in}} = f(V, \omega) \qquad (2.43)$$

Because of the synergistic influence between the propeller and electric motor on the total electric power required, the most optimal operating point is the result of an optimization. To investigate these influences further, the drive train has been analyzed for a range of feasible airspeeds and rotational shaft speeds. The reference Panthera has been analyzed at sea level, with a rate of climb of 6 m/s. The rate of climb has been added since it amplifies the sought-after phenomenas. The result gives insight into the power requirements and operating efficiencies of the drive train components.

For every airspeed, there is a corresponding required thrust to overcome the drag and gain potential energy. This thrust is delivered at a range of rotational velocities, leading to various system component efficiencies. Figure 2.33 shows the efficiencies of the propeller and electric motor for a range of airspeeds. The shaded area includes the efficiencies of all feasible rotational speeds. As can be seen, the efficiency of the propeller is very sensitive to airspeed. The electric motor is almost independent of airspeed but more depending on rotational shaft speed. Furthermore, the overall efficiency of the electric motor is much higher compared to the propeller. The required input power for the electric motor is shown in Figure 2.34.
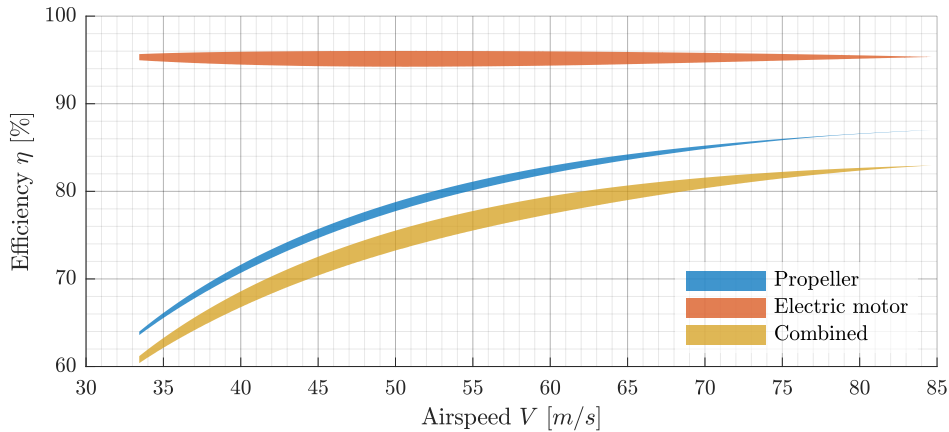
Figure 2.33: Efficiencies of propeller and electric motor for all feasible shaft speeds at various airspeeds.

The following three strategies to determine the desired operating point have been analyzed:

1. The *minimal required shaft power* has been determined, given $V@min(T \cdot V)$.

2. Next, the *minimal required shaft power* has been determined for any combination of airspeed and rotational speed.

3. Lastly, the *minimal required electric power* has been determined, again for any combination of airspeed and rotational speed.

The power required at the electric motor is 164.1 kW (100%), 152.7 kW (Δ-6.9%), and 152.5 kW (Δ-7.1%) for strategies 1 to 3 respectively. By fine tuning the shaft- and airspeed during climb specifically for minimal required power at the electric motor, a 7.1% improvement can be obtained. A big advantage of this strategy is
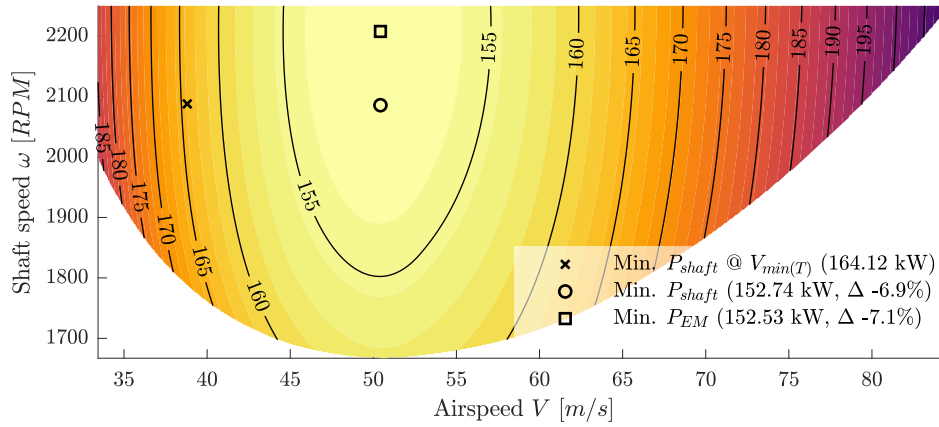
Figure 2.34: Power required by the electric motor (in kW) for various airspeeds and shaft speeds. No feasible combinations are possible outside the color map.

that only one design variable is required, namely the rate of climb. In Figure 2.35 a cruise situation at $h = 3660\ m$ is analyzed. The contour lines indicate the amount of energy that is required to fly one kilometer in percentages, the most optimal point (0.25 kWh/km) has been set to 100%. When this is minimized, the most optimal cruise speed is obtained for maximum range. As can be seen, the added value of including the feedback of the propeller and electric motor performance is significantly lower compared to the climb.
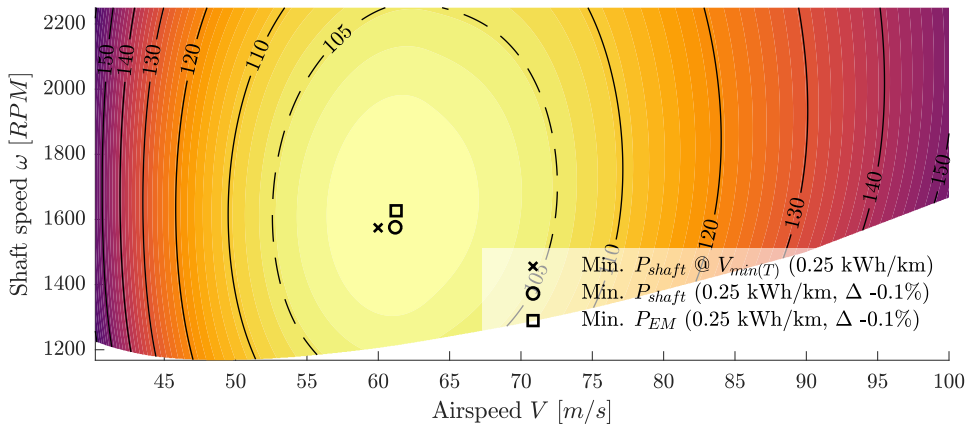
Figure 2.35: Energy that need to be delivered to the electric motor to travel a certain distance for various airspeeds and shaft speeds. The most optimal point (0.25 kWh/km) has been set to 100%. No feasible combinations are possible outside the color map.

2.8.2. Battery Sizing

As a result of the mission and propulsion analysis, a power profile is calculated that needs to be drawn from the battery; Figure 2.36 shows such a profile for the takeoff, climb and the beginning of the cruise phase. The battery needs to be sized in order to satisfy the constraints as presented in Section 2.5.4. Because the battery weight has a strong influence on the total aircraft weight, it is important that this sizing procedure is very accurate. Furthermore, since the optimization is gradient-based, it is important that any slight change in the mission profile result in a smooth change in battery weight and performance. The ultimate goal is to find the smallest battery in terms of capacity that satisfies all requirements.
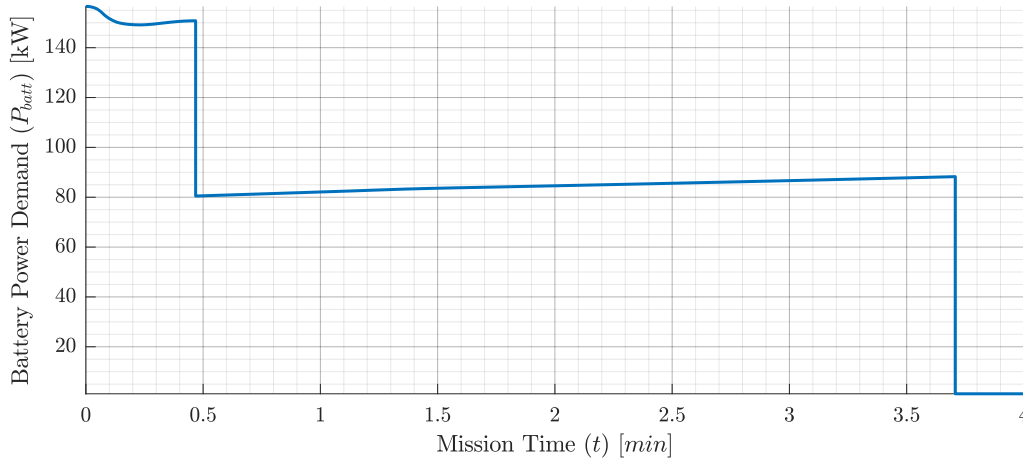
Figure 2.36: Power demand from battery for takeoff, climb and a short section of the cruise.

To be able to size the battery, the power demand for the complete mission needs to be analysed. The initial battery capacity used for the sizing is estimated such that the required energy is 85% of the total battery capacity using a constant efficiency of 95%. The required energy is determined using trapezoidal integration of the power demand curve. First, the analysis of the battery performance will be explained, after which the sizing routine will be explained.

The starting point of the battery analysis is the boundary condition at the beginning of the mission: At $t = 0$, the battery is full, hence its state of charge is 1. Furthermore, for every moment in time, the required power is known. The task of the battery analysis module is to translate this power demand of the battery to the performance of the battery. Since the internal efficiency depends on the state of charge, and the future states of charge are influenced by the efficiency, the battery analysis cannot be solved explicitly. Therefore, the differential equation shown in Equation 2.44 needs to be solved.

$$\frac{d}{dt}(SOC) = f(t, SOC) \tag{2.44}$$

A large amount of literature has been written about solving differential equations. One of the most straightforward method is the Euler method, which uses the slope at the last known point in time, to predict the function value of the next unknown point: $SOC_{n+1} = SOC_n + h \cdot f(t_n, SOC_n)$, where h is the step size. The error of Eulers method is roughly proportional to the step size h, meaning that many segments are required to obtain satisfying accuracy. By adding more function evaluations, higher accuracy and convergence characteristics can be obtained. For example, the mid-point method - which is basically a modified Euler method - uses the following scheme: $SOC_{n+1} = SOC_n + h \cdot f\left(t_n + \frac{1}{2}h, SOC_n + \frac{1}{2}h \cdot f(t_n, SOC_n)\right)$. Other examples are the family of Runge-Kutta (RK) methods, of which the classical RK-4, the RK-23, and the RK45 have been analysed. One of the attempts in this thesis was to approximate each segment by using a quadratic approximation based on the function values at $h = 0.01$ and 0.02. Based on the Δt values and the states of charge at these points, a quadratic curve is determined which is used to calculate the state of charge at the next point. Figure 2.37 shows the result of a comparison study between the methods.

As can be seen in the comparison study, each method shows it own convergence characteristics. The computational time per analysis has been determined by measuring the time it takes to run four consecutive analyses,
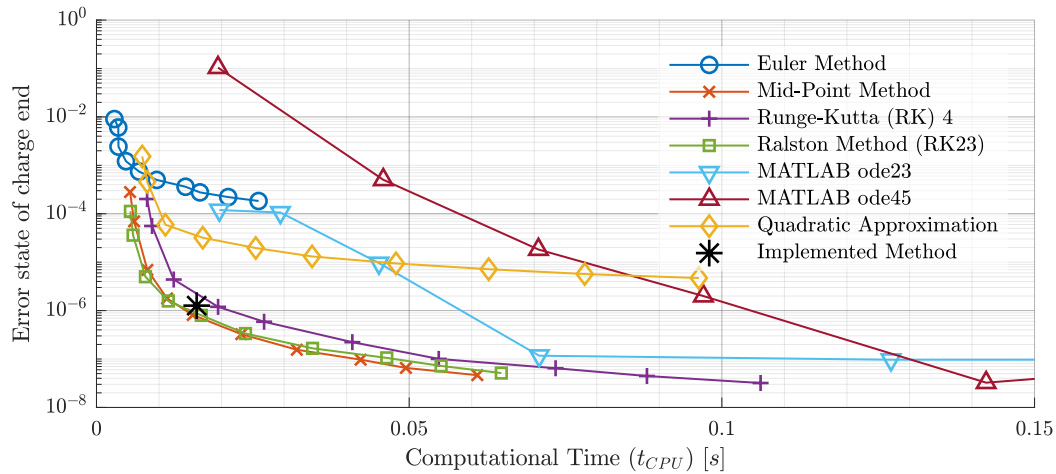
Figure 2.37

divided by four. The reference state of charge at the end of the mission has been determined by running MAT-LAB's ode23 with machine precision ($2 \cdot 10^{-14}$) as termination criteria. By increasing the amount of analyses segments per mission segment and the maximum time step between two points overall, the accuracy has been increased. Consequently, the time steps between points during takeoff are smaller compared to the cruise. This is beneficial since the power demand, and hence the non-linear behaviour of the battery performance, is much higher during takeoff compared to the cruise for example. For all the methods, except the MATLAB methods, the total amount of segments has been varied from 125 to 1800.

The Euler method, which is the simplest, shows the worst performance. The quadratic attempt is a little better, but definitely not the best. Between the Ralston method and the Mid-Point method there is very little difference, and they show the best performance in terms of error versus computational time. Interestingly, the more complex Runge-Kutta 4 method shows worse performance compared to the simpler Ralston method. The MATLAB methods converge with a high precision, however, they require more computational time to do so.

The bad performance of the build-in MATLAB differential solvers stems from the way the solver can be implemented in the existing code. Due to the overhead time of the build-in functions and the need for lots of sequential interpolations of the power demand curve, the computational time required is relatively high. However, when the obtained error versus the number of analysed segments and function calls are compared, the MATLAB solvers excels. The same logic goes for the Runge-Kutta 4 method. In terms of computational time, specific for the implementation in the rest of the code, it underperforms compared to the simpler methods such as Ralston and Mid-Point. When comparing RK4 with Ralston in terms of function calls, the RK4 performs slightly better.

In this thesis work, the Mid-Point method is implemented in the simulation. Hundred analyses segments are equally spaced over the whole mission, with a minimum of forty analyses segments per mission segment. In the example mission used for Figure 2.37, this results in a total of 380 analyses segments with a computational time of approximately 0.017 s per mission analysis and an error of 10^{-6}.

From the aforementioned analysis routine, the state of charge at the end of the mission is known. For example, if this state of charge is lower than 15%, the battery is to small resulting in bad life-time performance. In this case, the battery capacity needs to be increased. The first new estimate is based on the average efficiency of the first analysis. After this, two capacities and their corresponding states of charge at the end of the mission are known. The capacities of all subsequent iterations are determined using a shape-preserving piecewise cu-

bic interpolation, translating a desired state of charge end to a required capacity, as can be seen in Figure 2.38. The database of reference points grows with every iteration, hence the accuracy of this method increases very rapidly.
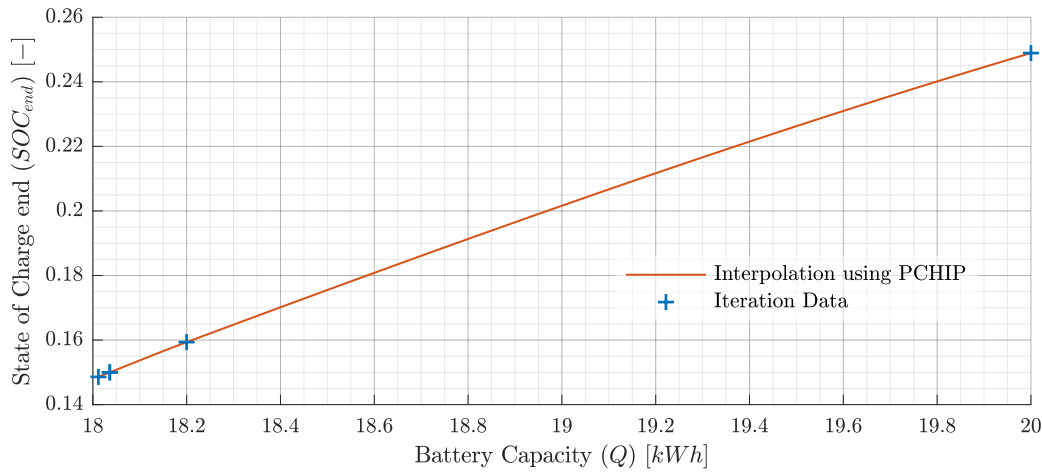
Figure 2.38: State of charge at the end of the sizing mission versus battery capacity for different iterations of the battery sizing. The interpolated line is used to determine the capacity of the next iteration until termination criteria are met.

To illustrate the convergence behaviour of the battery sizing module even better, the state of charge at the end of the mission and the error are plotted versus the iteration number in Figures 2.39 and 2.40 respectively. Clearly, it can be seen that the convergence behaviour is excellent. After only five iterations, the error of the final state of charge is almost 10^{-8}. Because the battery performance analysis is relatively cheap in terms of computational requirements and the sizing module show rapid convergence behaviour, the sizing termination criteria has been chosen such that the error in final state of charge is lower than 10^{-6}.

In addition to the state of charge, the battery voltage and current at every moment in time are calculated in the analysis module. Figure 2.41 shows the battery voltage and current for the first 4 minutes of an example mission. As can be seen, the battery voltage during takeoff drops significantly compared to the other segments. One of the other battery requirements, besides the final state of charge, is that the battery voltage may never drop lower than 2.7 V. Analog to the sizing strategy of the final state of charge, the battery is sized based on the minimum voltage at any point during the mission. The biggest battery according to the two requirements is selected for the next iteration.

Surrogate Battery Capacity

One of the goals of the optimization is to converge to one aircraft design, in which the mass used for the aerodynamic calculations is consistent with the actual aircraft mass. Since the battery mass is highly influenced by the operational variables and any variable that affects aircraft drag, it is a key link in the determination of the aircraft its mass. By decoupling this influence, as shown in the *DSM*'s in Figure 2.42 and 2.43, the optimizer can take more shortcuts through the infeasible design space. This leads to better optimization performance. Table 2.10 shows the quantified differences in terms of optimization performance between using and not using a surrogate variable for battery capacity. For both a range of 150 km and 600 km, the optimization is much smoother when using this surrogate variable for battery capacity. Interestingly, the difference in number of function calls for the optimization for a range of 150 km is much smaller compared with the difference in computational time. This is because more of the function calls are spend during the finite-difference process, which are performed
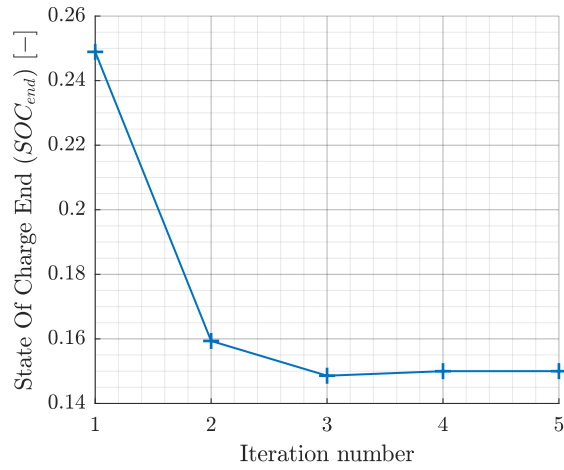
Figure 2.39: State of charge at the end of the sizing mission versus iteration number of the battery sizing.
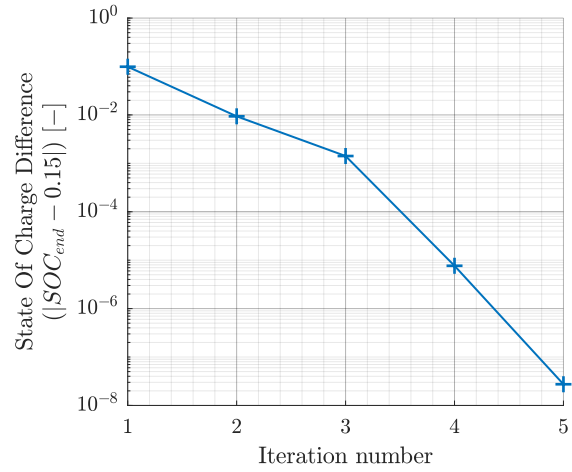
Figure 2.40: Difference in state of charge at the end of the sizing mission and the minimal required state of charge of 0.15 versus iteration number of the battery sizing.
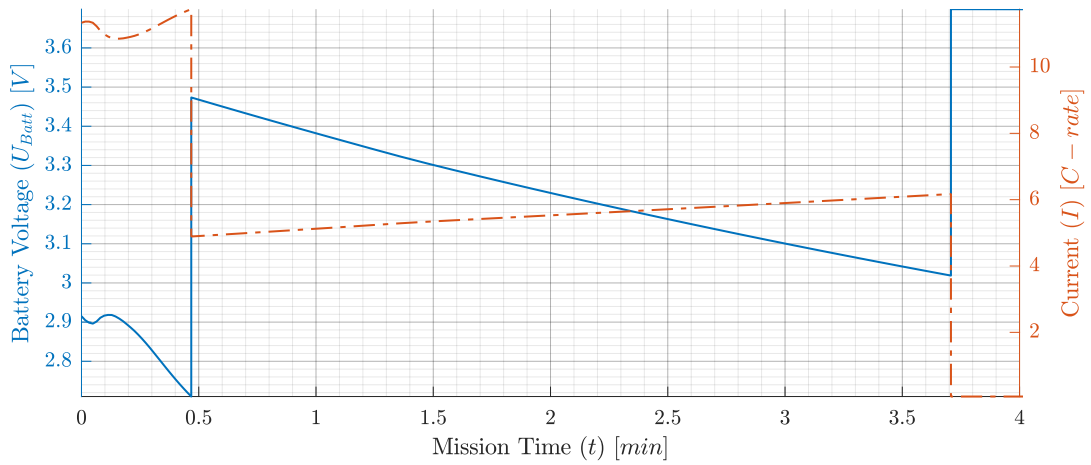
Figure 2.41: Battery voltage and current for the first 4 minutes of flight. Solid line (——) corresponds to the left axis, dashed-dotted line (— · — ·) corresponds to the right axis.

in parallel and hence require less computational time per call. It must be noted however that the optimization results can be optimistic when using a surrogate battery capacity since a difference between actual capacity and surrogate capacity is tolerated. By setting the tolerance on this particular constraint low, an accurate solution is obtained.
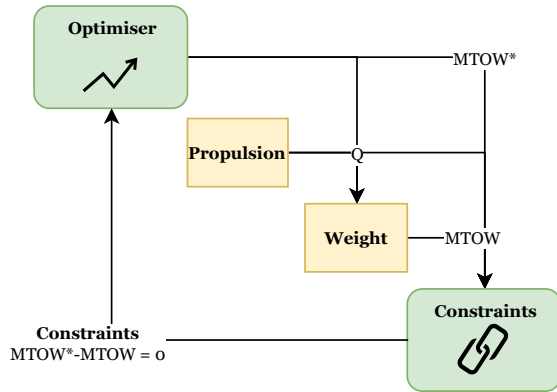
Figure 2.42: Simplified DSM without surrogate battery capacity
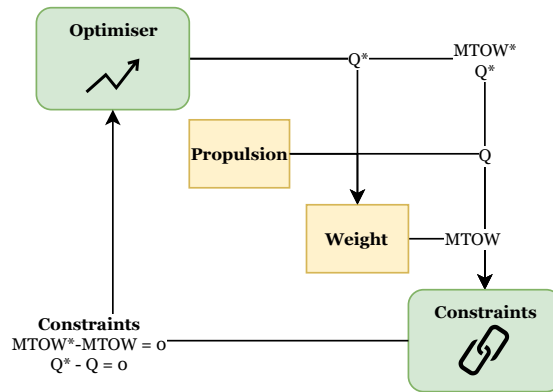
Figure 2.43: Simplified DSM with surrogate battery capacity

Table 2.10: Optimization performance difference between using a surrogate battery capacity or not.

		150 km			600 km		
		Without Q*	With Q*	Difference	Without Q*	With Q*	Difference
CPU Time	*Seconds*	202	121	40% faster	271	93	66% faster
$ESAR_{fuel}$	kWh/km	0.492	0.489	0.62% lower	N/A**	0.91	N/A**
Function count		83	76	8.4% less	86	54	37% less
Iterations		7	8	14% more	5	3	40% less

** Optimization did not converge

3

Results and Observations

To work towards the aim of this research, various optimization studies have been performed. In Section 3.1 a study that compares the influence of different objectives on the performance of aircraft is presented. The influence of throttle setting on the performance is presented in Section 3.3. The influence of cruise speed on the optimal design and performance is presented in Section 3.4. Lastly, the influence of battery specific energy density on the performance is presented in Section 3.5.

3.1. Minimization of Fuel and Energy Consumption for Different Ranges

In this section, the results of an optimization study in which two different objectives, namely minimization of fuel and total energy optimization, are presented for various ranges. The goal of this optimization study is to find the influence of objective and range on the optimal operation and design of a hybrid-electric aircraft. The following design variables have been used:

- Wing surface area
- Aspect ratio
- Taper ratio
- Rate of climb
- Electrification of the cruise

Furthermore, the range is varied from 50km up to 800km, in 50 steps. All the presented aircraft designs are the result of successful optimizations, as the infeasible designs and designs that where produced by optimizations that did not satisfy the first order optimality criteria are discarded.

Influence of Objective and Range on Energy and Efficiency

The results in terms of energy of the aforementioned optimization are shown in Figure 3.1. The total energy is a summation of the fuel and battery energy that is used in the design mission, i.e. the takeoff, climb, cruise, and descent. Furthermore, the energy dissipation through the mechanism of drag is shown in said figure. The fraction of energy dissipation through drag over the total energy equals the efficiency of the complete propulsion system. To clarify, the solid lines (———) represent the results of the fuel optimizations and the dash-dotted lines

($-\cdot-\cdot$) represent the results of the total energy optimizations. To reduce the clutter and allow for more precise readout of the figure, the markers of each result have not been included. However, to aid the identification of the various lines, the start and end of each line has been indicated with a marker.
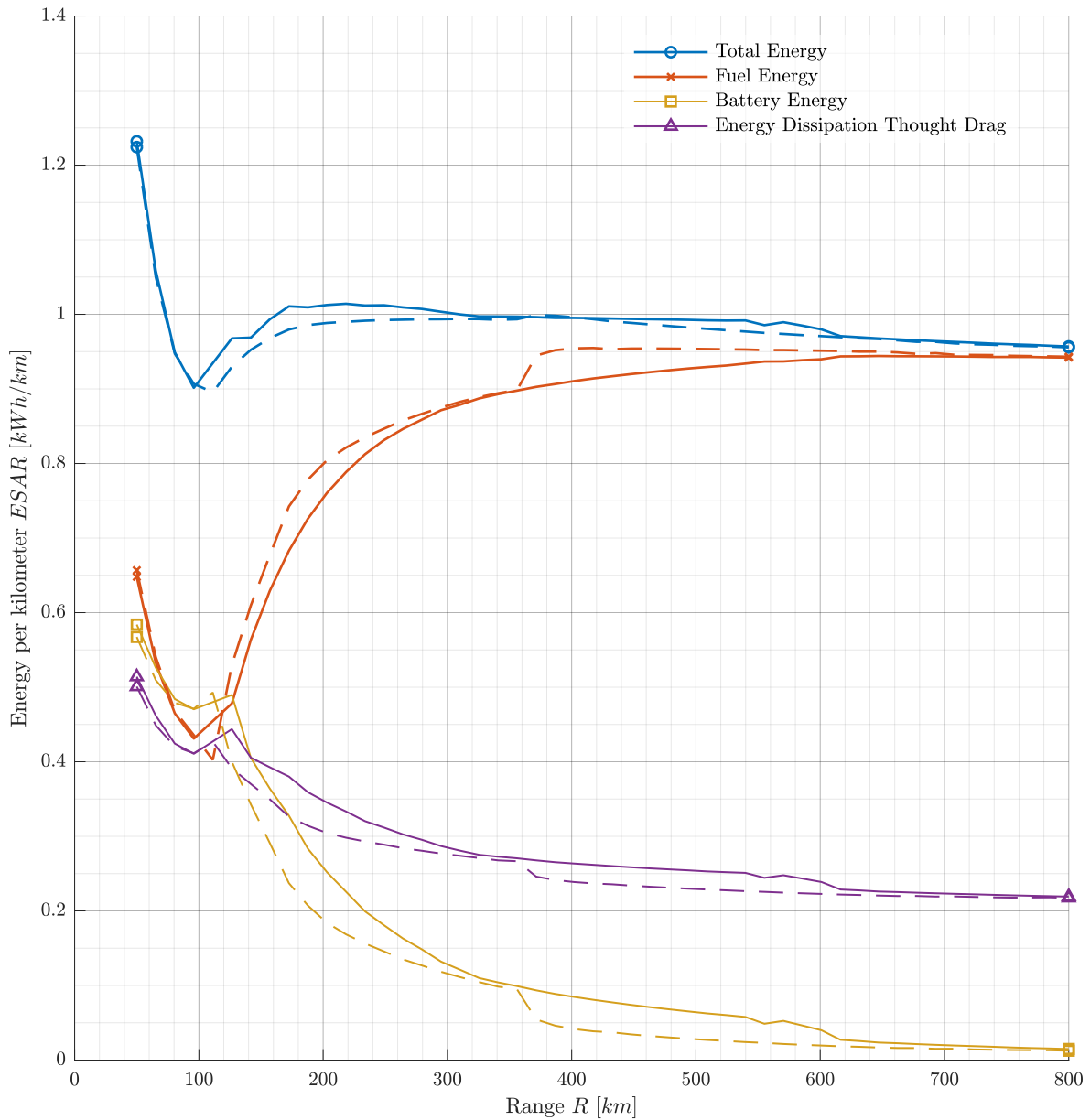
Figure 3.1: Comparison between total, fuel, battery, and in the air dissipated energy for fuel and total energy optimization versus the range. The solid lines (———) represent the results of the fuel optimizations and the dash-dotted lines ($-\cdot-\cdot$) represent the results of the total energy optimizations

The first and arguably most important observation made is regarding the difference in terms of energy consumption of both objectives. As can be seen clearly, there is a difference in terms of fuel and total energy consumption when comparing the two different objectives. The fuel consumption of aircraft specifically designed for minimal fuel consumption is consistently lower compared to that of aircraft designed for minimal total energy, and vice versa. This fact provides confidence that the optimization routine works since if this was not the

case, the optimization would certainly not work properly. At the short (100km) and the long end (800+km) of the ranges, the difference in energies for the two objectives are converged to zero.

Two general trends can be observed in the figure: for increasing design ranges, irrespective of objective, the amount of battery energy as well as the energy dissipation through drag decreases. These observations highlight a very important tradeoff which need to be made as part of the optimization: choosing between a design that is aerodynamically very efficient or a design that is able to carry a significant amount of batteries. The former reduces the aerodynamic drag and hence the energy dissipation through it, whereas the latter reduces the conversion losses within the propulsion system powertrain as the energy conversion within batteries is much higher compared to the conversion in combustion engines.

Again, aircraft optimized for fuel consumption require more total energy for their mission compared to aircraft optimized for total energy. The difference in energy between the total required energy and the energy stored in the fuel needs to be provided by the batteries. Since battery energy is not included in the objective value when minimizing the amount of fuel, the only downside of added batteries is the effect it indirectly has on the aerodynamic efficiency, i.e. the aforementioned tradeoff between aerodynamic and energy conversion efficiency needs to be made. If the increase in energy dissipation through drag, as a result of adding a certain amount of batteries, is so high that it leads to more fuel consumption compared to when no extra batteries are installed, it is better to not install them after all. As can be seen clearly in the figure, for moderate ranges between 100 and 700km it is actually beneficial to install more batteries at the cost of some aerodynamic drag. For ranges above 700km, however, the designs in terms of energy sources are converged: the optimal amount of batteries for either fuel or total energy optimization is the same.

When an aircraft with the least fuel energy per kilometer is desired, what is the best range to design this aircraft for? From this analysis, as can be clearly seen in the figure, the shorter the mission range the better. The most efficient aircraft design has a range of around 100km. It must noted this range can be decreased even more when adding the throttle of the internal combustion engine as a design variable. This particular aircraft carries quite a large amount of batteries, that reduces the need to burn fuel and provides an efficient power train conversion. Increasing the range from 100km, the fuel consumption spikes up and slowly approaches a convergence point around 800km. The difference in fuel consumption between 350km and 800km is only about 0.05 kWh/km whereas the difference between 350km and 200km is already 0.15 kWh/km. The difference between 100km and 800km is around 0.45 kWh/km. On the other hand, when not the least amount of fuel energy is the objective but the least amount of total energy, the picture looks completely different. Admitting, the most efficient range in terms of total energy lies also around 100km and spikes up when the range is increased. What is different, however, is that from ranges larger than 400km the total energy consumption per kilometer decreases steadily. Furthermore, the difference in the total required energy between 100km and 800km is only around 0.07 kWh/km. Therefore, although around 7.5% less efficient, it is much more attractive to design an aircraft for longer ranges when the objective is total energy compared to having fuel energy as objective.

Lastly, a note must be made regarding the selection of the optimal aircraft. When an aircraft is desired for a range of 400km with minimal total energy consumption as objective, it seems logical to specifically design that aircraft for its objective. As can be seen, the resulting total energy consumption will be slightly lower compared to an aircraft designed for minimal fuel consumption. However, although the aircraft is performing slightly better in terms of its objective, there is an opportunity to greatly reduce the fuel consumption at the cost of just a fraction of the total energy consumption.

Influence of Range and Objective on Optimal Design Variables

The earlier observed trends in the energy consumption and dissipation are the direct result of different aircraft designs. The values of the design variables leading to these trends are presented in Figure 3.3. Most closely related to the energy consumption relations that where found is the electrification of the cruise phase. At the very short end of the various ranges, up to around 100km, a full electric cruise is possible. For increasing ranges, the electrification drops quickly and converges slowly to approximately 15%. The reason why it does not converge to zero, is the following: since the internal combustion engine is not powerful enough to provide the required power for takeoff and climb, a minimal amount of batteries need to be installed in the aircraft. At a certain point, the aircraft design is such that the amount of power required by the power management system during cruise is less than what the internal combustion engine is capable of providing, leading to the possibility of recharging the batteries that where required for takeoff and climb.
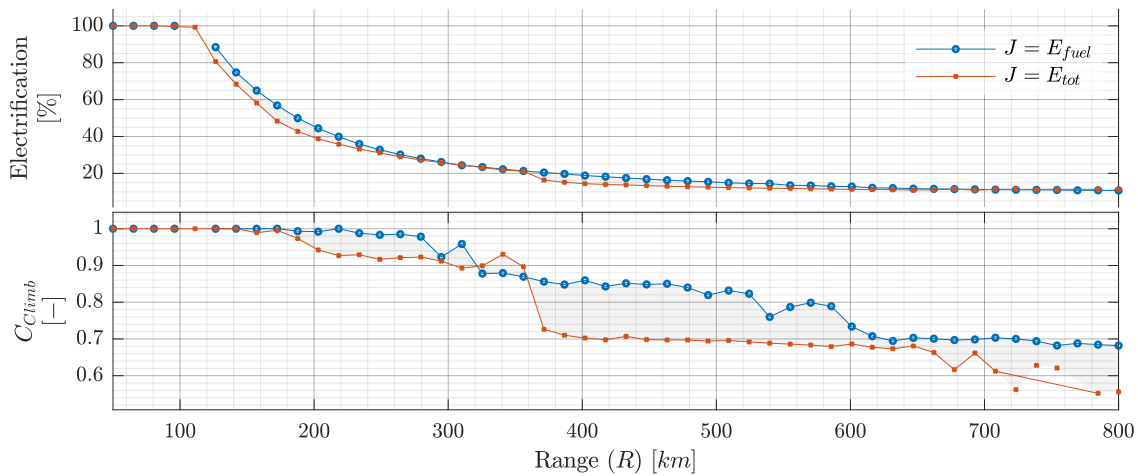
Figure 3.2: Influence of objective and range on optimal electrification of the cruise and relative rate of climb

Closely related to the electrification of the cruise phase, is the strategy on how to perform the climb. The required power for to climb depends on two terms: the power that is dissipated in the air through aerodynamic drag and the power that is required to gain potential energy. Since the measure of required energy takes into account the required energy for the complete mission, i.e. including climb and descent, the potential energy gain during climb cannot be seen as loss, but merely a change in state of useful energy. However, any decrease in the time to climb leads to a reduction of energy dissipation through drag. Therefore, the time to climb is tried to be minimized by maximizing the rate of climb. As mentioned earlier however, the internal combustion engine is not really powerful. This means that virtually all the power required to increase the rate of climb needs to be delivered by the batteries. As can be seen from the climb coefficient, the climb strategy for the shorter ranges is to maximize the rate of climb whereas the opposite is true for the longer ranges where the rate of climb is approximately 65% of the maximum rate of climb of the particular designs. Furthermore, aircraft designed for minimum total energy climb at an even lower fraction of their maximum rate of climb compared to aircraft designed for minimum fuel. This can be explained by the fact that these designs do not prioritize the usage of batteries as much.

The second observation made in the analysis of energies was regarding the aerodynamic efficiency of the designs, which is found to increases with increasing range. Also, the aerodynamic efficiency is prioritized over the utilization of batteries when designing for total energy minimization. One of the methods to increase the
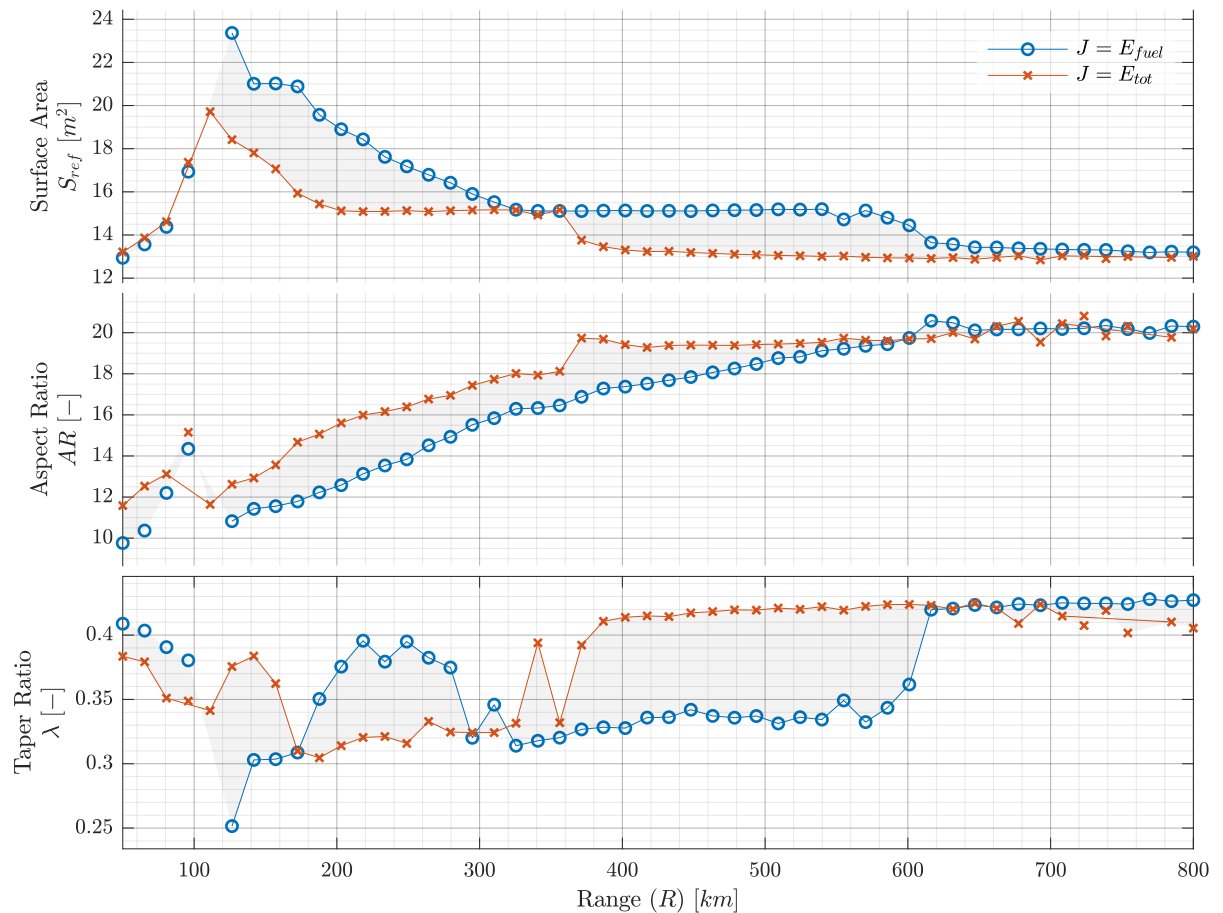
Figure 3.3: Influence of objective and range on optimal surface area, aspect ratio, and taper ratio

aerodynamic efficiency is reducing the lift induced drag. The most effective way to reduce the lift induced drag is to increase the wing span and consequently trying to approach the performance of an infinite wing. As can be seen, this is exactly the case. Furthermore, aircraft designed for minimal total energy have higher aspect ratios compared to aircraft designed for minimal fuel.

A higher maximum takeoff weight translates almost linearly into a larger wing surface area in order to maintain the same low speed performance. To enable the installation of more batteries, and hence a heavier aircraft, the wing surface area needs to be increased. As can be see in the figure, this is the case for shorter ranges and for designs optimized for fuel optimization.

Lastly, the taper ratio will be discussed, however, the trends here are less clear as with for example the electrification and aspect ratio. The taper ratio has several areas of influence. First of all, it influences the span-wise distribution of lift. The optimal, near elliptical, distribution is achieved with a taper ratio of around 0.3, and increasing the taper ratio from here will move the lift distribution away from the optimal one. Furthermore, decreasing the taper ratio up to 0 will decrease the wing root bending moment because more lift is produced inboard. This will influence the wing weight positively. Lastly, the taper ratio is highly connected to the location and moment of wing stall. For wings with extremely small taper ratios, the local Reynolds numbers at the tip will be so small that wing stall is easily initiated here. Increasing the taper ratio will prevent tip stall. What can be seen clearly is that the taper ratio seems to converge around 0.41 for designs for 800km. Between 400km

and 600km there is a distinct difference in taper ratio for the two objectives. Aircraft designed for minimal fuel energy have a lower taper ratio of around 0.33 here where as aircraft designed for minimal total energy have a taper ratio of around 0.41 in this region.

Further Investigation of the Aircraft Designs

Besides the energies and design variables, there are other interesting trends that can be identified by looking into parameters that are a consequence of the optimizations, namely the takeoff field length, stall speed, wing loading, power loading, maximum takeoff mass, aerodynamic efficiency, and amount of recharging. These parameters are plotted in Figure 3.4.

When comparing the maximum takeoff mass with the surface area as presented in Figure 3.3, it becomes clear that the two are highly correlated. This can be explained by looking at the stall speed and wing loading. To ensure low speed stall performance, a certain combination of wing loading and maximum lift coefficient is required. Since the airfoil shape is not changed during the optimization, the maximum wing lift coefficient remains approximately constant. Consequently, the wing loading needs to remain either constant or decrease to satisfy the stall speed constraint. To enable the installation of more batteries, and thus allow for a higher maximum takeoff mass, the wing surface area is increased. Furthermore, because the maximum power output of the electric motor is also kept constant during this optimization, the power loading correlates 100% with the maximum takeoff mass.

Interestingly, the lift over drag ratio for ranges shorter than 375km is higher for the aircraft designed for minimum total energy whereas for ranges longer than that it is higher for aircraft designed for minimum fuel energy. Although the lift over drag ratio is not consistently lower for either of the two objectives, the energy dissipated in the air is. This indicates that maximizing the lift over drag ratio does not necessarily results in an overall more efficient aircraft.

With increasing range, as explained earlier, the reduction of energy dissipation through drag becomes increasingly important. At a certain range, the power delivered by the internal combustion engine/generator combination is higher than the power required by the power management system during the cruise of that particular aircraft. From this range onwards, recharging of the batteries is possible in the aircraft optimized for the corresponding ranges. As can be clearly seen, this point is reached at shorter ranges for aircraft designed for minimal total energy.
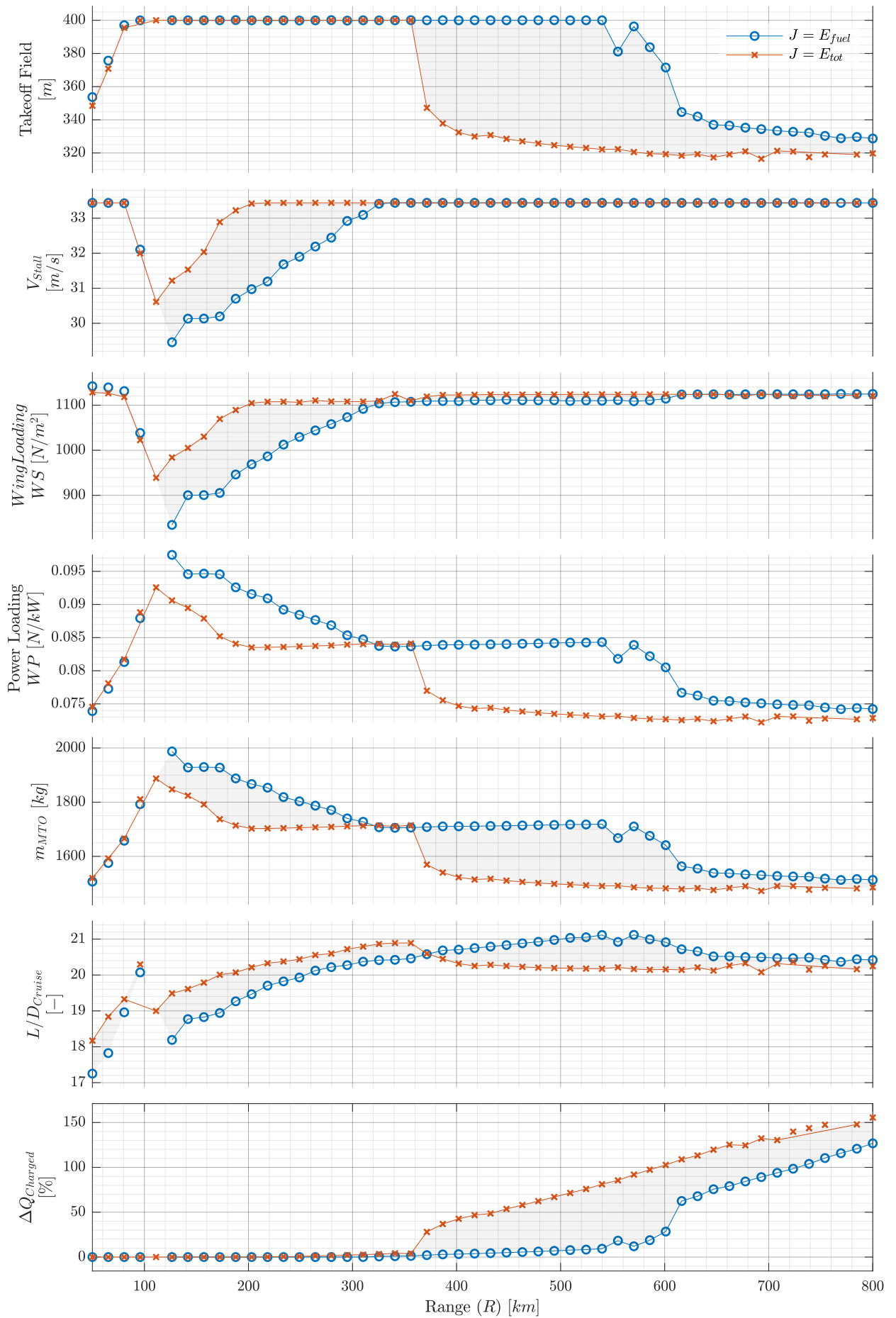
Figure 3.4: Influence of objective and range on various parameters

Influence of Range on Optimal Wing Planform

To visualize the implication of range on the optimal wing planform, the top view of the optimized wings for various ranges are plotted in Figure 3.5. The black contour line is the wing planform of the current Panthera. As can be seen, the span and aspect ratio are significantly higher for the new designs. To understand this trend better, the corresponding lift-drag polars are shown in Figure 3.6. The markers in these polars indicate the lift coefficient at which the cruise phase is flown. Since the cruise velocity used in the optimizations is lower compared to the cruise speed of the original Panthera, the lift coefficient during cruise is significantly higher. As can be seen, the lift-induced part of the cruise is consequently higher. Therefore, it is attractive for the optimizer to attempt to decrease the lift-induced drag by increasing the aspect ratio of the wing, and thus the wing span. This actually happens for most of the aircraft designs, since the slope of the lift-drag polar is lower compared to the original Panthera. What is difficult to explain, however, is why the design for 50km has such a short wing span and consequently such a high drag coefficient during cruise. It could be that the optimizer found that the increase in aerodynamic efficiency did not justify the corresponding increase in wing weight.
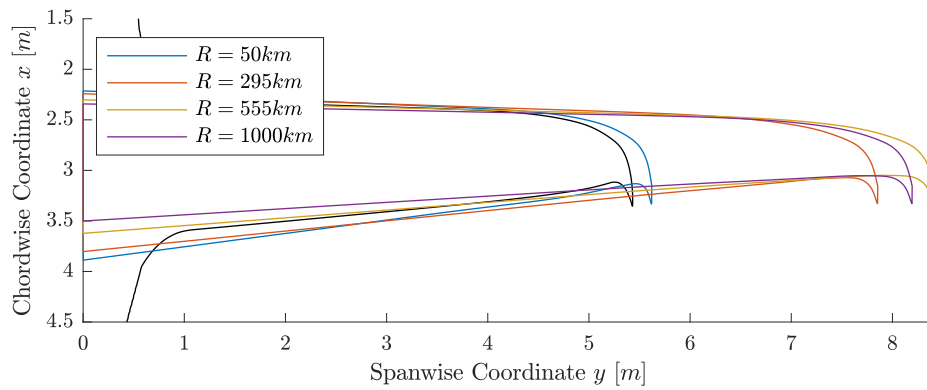
Figure 3.5: Comparison of the main wing planform between four aircraft optimized for minimal fuel consumption, each with a different design range.
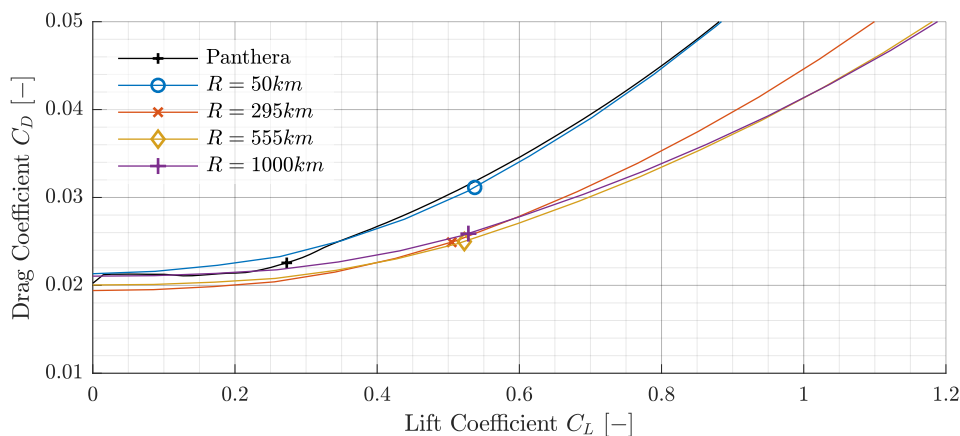
Figure 3.6: Comparison of the lift/drag polar between four aircraft optimized for minimal fuel consumption, each with a different design range. The marker indicate the cruise lift and drag coefficient.

Influence of Objective on Wing Planform

Aircraft designed for the two different objectives differ a lot in terms of energy consumption at a range of 200km, and differ significantly around a range of 550km. Therefore, the wing planform of two aircraft designed for the different objectives are shown for a design range of 200km and 550km in Figures 3.7 and 3.8 respectively. As can be seen, there is no significant difference in span for 200km. However, there is a pronounced difference in terms of surface area. The wingspan of the aircraft designed for minimal fuel consumption and a range of 550km is higher compared to the aircraft designed for minimal total energy.
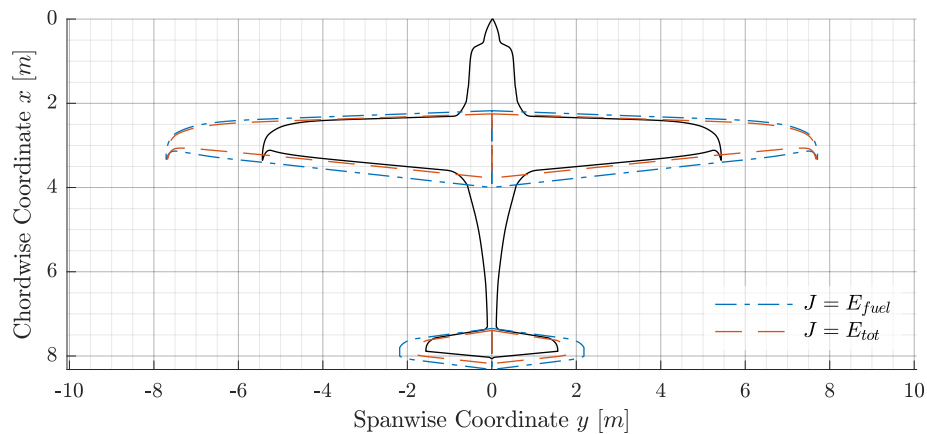
Figure 3.7: Comparison of the wing planform between aircraft either designed for minimal fuel or total energy consumption, both with a design range of 200 km.
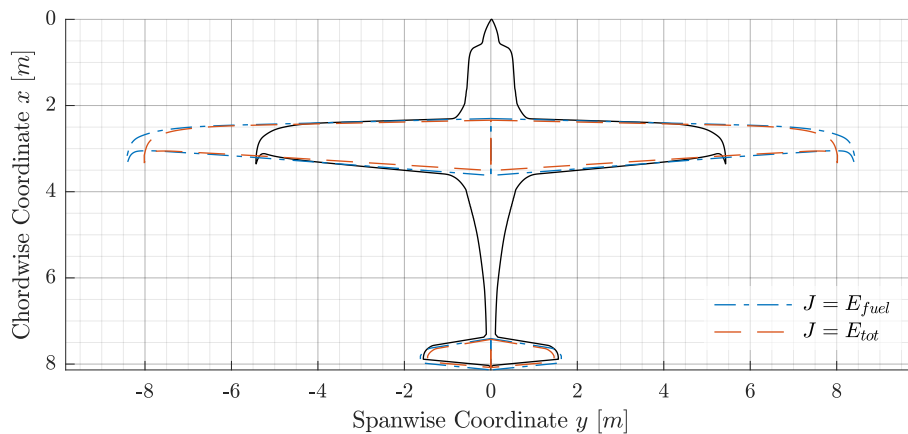
Figure 3.8: Comparison of the wing planform between aircraft either designed for minimal fuel or total energy consumption, both with a design range of 550 km.

Operating Points on Propeller and Electric Motor Performance Map for Various Ranges

As part of the optimization process, a specific combination of propeller shaft speed and torque is selected each iteration that leads to the minimization of required electrical power at the power management system for a certain thrust requirement. For the climb phase this is done in alignment with the optimal airspeed. In Figure 3.9 and 3.10 the operating points of respectively the propeller and electric motor are shown for 4 different ranges between 50 and 1000km of aircraft designed for minimal fuel consumption.
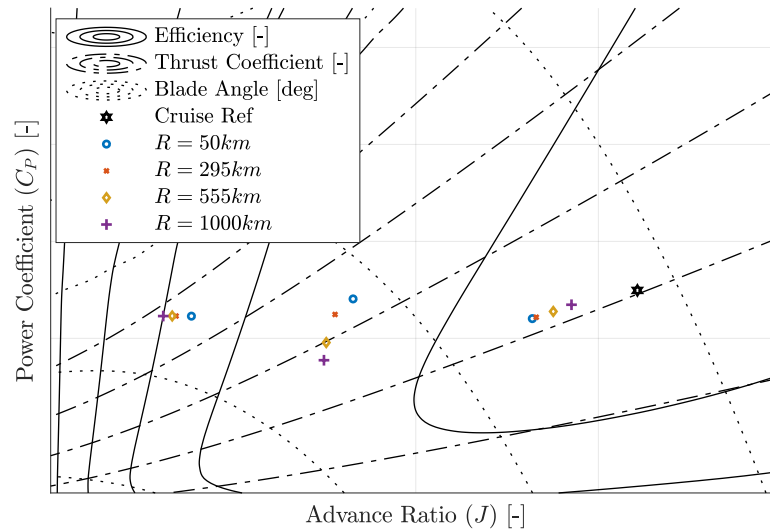
Figure 3.9: Operating points of 4 optimized aircraft on the propeller performance map
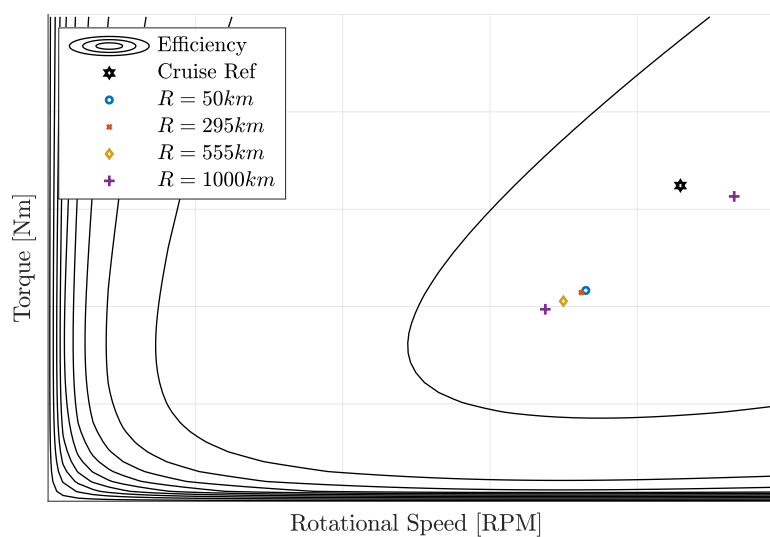
Figure 3.10: Takeoff, climb, and cruise of four aircraft on the electric motor performance map. Each aircraft is optimized for minimal fuel consumption at a certain design range.

The points at the left side of the propeller map, close to an advance ratio (J) of 0.35, are the average of the takeoff phase. In the middle of that figure, around an advance ratio of 0.8, are the points corresponding to the climb phase. Lastly, the 4 most right points represent the cruise phase. On the electric motor map these are the points in the upper right corner, the scattered points below that around a RPM of 2250, and the points around a RPM of 1600.

Several interesting trends can be identified from the performance maps. During takeoff, it is desired to have the maximum power output, hence the maximum rotational speed and torque of the electric motor. On the propeller map, as the airspeed is low during the acceleration phase of the aircraft these correspond to a low advance ratio. For the climb phase, generally the maximum rotational speed is desired in combination with a

decreasing torque for increasing ranges. The fact that the power output during climb reduces can be explained as the rate of climb and the maximum takeoff mass, and therefore the amount of thrust, decreases with increasing range. On the propeller map this can be seen as with an increasing range the operating points of the climb move towards a lower thrust and power coefficient.

As the drag decreases with increasing range, the amount of thrust and thus output power of the electric motor decreases. The electric motor simultaneously decreases the rotational speed and torque to produce the required power. The lower rotational speed translates to a higher advance ratio of the propeller. Since the propeller was designed for the original Panthera, which has a higher cruise speed, it is not surprising that the most efficient operating point is found at higher advance ratios.

It must be noted that for this study it is assumed that the propeller is completely variable in blade pitch, even during flight. Therefore, the operating points of the takeoff, climb and cruise can be at different blade pitch angles. If it is desired to remove the pitch control during flight, a specific blade pitch needs to be selected for all the flight segments. Since the efficiency of the electric motor is very high for a large area of operation, a certain shaft power can be delivered at almost the same high efficiency over a wide range of rotational speeds. This makes it very flexible to move the operating points over the propeller performance map, without sacrificing to much efficiency. Although this is verified in a quick analysis, it is recommended to further study the influence of fixing the blade pitch if that is desired.

Lastly, it is recommended to investigate the influence of redesigning the complete propeller as part of the optimization process. Especially for missions with a short range, where the climb phase is responsible for a large part of the total required energy, it could be beneficial to use a propeller that is more efficient at lower advance ratios.

Battery Performance

The influence of range on the required battery power, battery discharge current, and state of charge is shown in Figures 3.11, 3.12, and 3.13 for 4 different ranges of aircraft designed for minimal fuel consumption. The spike in power demand from the batteries at the beginning of the mission is the power that is required for takeoff. Although the power demand of the electric motor will never be higher than that of the takeoff phase, the power demand of the batteries can actually be slightly higher. This is the case for aircraft designed for short ranges. Since their climb strategy uses the maximum rate of climb, and the power delivered by the internal combustion engine suffers from a power lapse with altitude, the power that needs to be delivered by the batteries is the highest at the end of the climb phase for these aircraft.

The difference in power demand for the full electric cruise phase of the different aircraft is rather small. What is significantly different however, is the discharge rate. Aircraft designed for long ranges, such as 1000 km, carry relatively small batteries and therefore have a high discharge rate. To better investigate the battery usage and discharge rate, Table 3.1 has been produced. This table shows how much battery capacity is discharged at a certain rate for the four different aircraft designs. For example, 73% of the battery optimized for 50 km is discharged at rates between 1 and 2. As can be clearly seen, the majority of the batteries are discharged at rates lower than 4. The takeoff phase of the aircraft designed for 1000 km requires a discharge rates of around 10 and discharges the battery by approximately 7%, whereas the climb phase requires a rate of around 5.5 and is responsible for 58% of discharge. Furthermore it can be seen that during the cruise 125% of the battery is charged at a rate of -0.5 and this is discharged at a rate of 3.5.

Comparing the results presented in Table 3.1 with the Ragone plot (fig. 2.26) presented in Section 2.5.4, it must be concluded that adjusting the gravimetric energy density for maximum discharge rate has potentially a
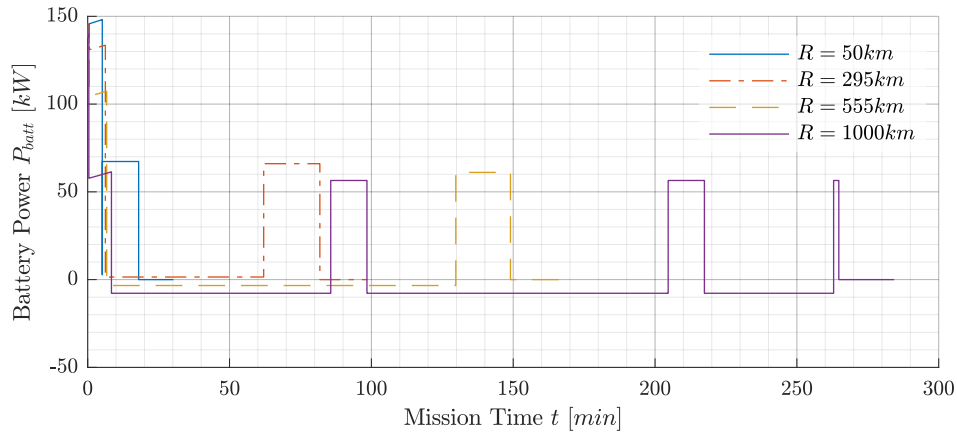
Figure 3.11: Comparison of battery power over the course of the mission between four aircraft optimized for minimal fuel consumption, each with a different design range.
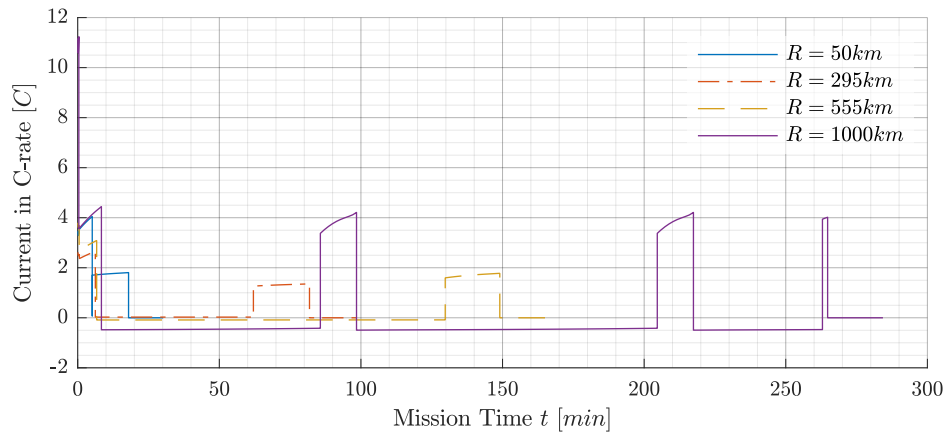
Figure 3.12: Comparison of discharge rate over the course of the mission between four aircraft optimized for minimal fuel consumption, each with a different design range.

significant influence on the battery mass.
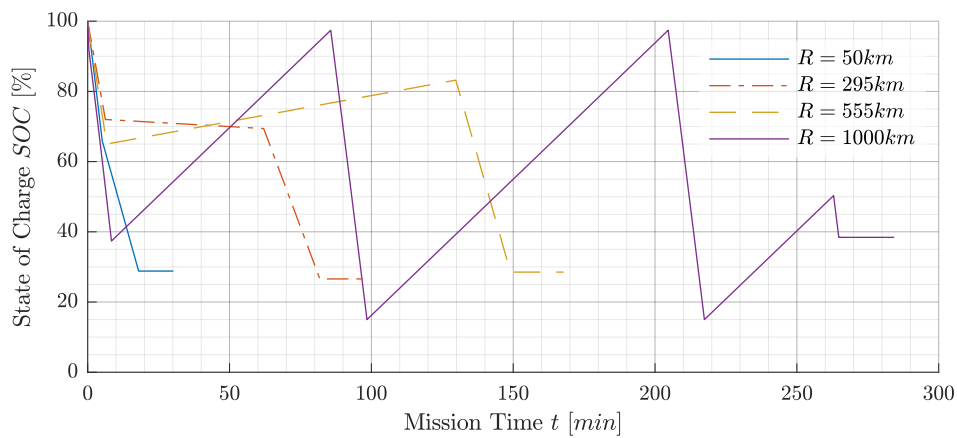
Figure 3.13: Comparison of state of charge over the course of the mission between four aircraft optimized for minimal fuel consumption, each with a different design range.

Table 3.1: Percentage of state of charge at various discharge rates and design ranges.

Discharge rate*	-0.5	0.5	1.5	2.5	3.5	4.5	5.5	6.5	7.5	8.5	9.5	10.5
50 km	-	2%	73%	-	-	-	-	-	-	-	-	-
295 km	-	3%	43%	28%	-	-	-	-	-	-	-	-
550 km	18%	-	55%	-	28%	4%	-	-	-	-	-	-
1000 km	125%	-	-	-	125%	-	58%	-	-	-	4%	3%

* Discharge rate = $\frac{d}{dt}(SOC)$ $[h^{-1}]$
Note 1 - percentages represent the amount of SOC that is discharged at a certain rate.
Note 2 - the discharge rates are averaged; e.g. a rate of 1.5 represents $1 \leq \frac{d}{dt}(SOC) < 2$
Note 3 - the SOC percentages do not add up to 100% because the safety segments (e.g. loiter) are excluded as they are not used in a typical mission.

As noted earlier, aircraft designed for long ranges are able to recharge the batteries during flight. In the last figure about the battery performance the variation of state of charge is shown over the mission time. This figure clearly shows the implemented recharge strategy, especially in the discharge profile of the aircraft designed for 1000km. At the beginning of the mission, the battery is discharged as power is required for takeoff and climb. The subsequent cruise starts with a hybrid segment in which the battery is recharged. At a certain point, when the battery is nearly full and cannot convert the all the provided power anymore to chemical energy, a switch is initiated to a full electric cruise segment. The next switch, back to a hybrid segment, is initiated when the state of charge of the battery is exactly 15%. This continues until the total cruise distance has been flown, after which the descent is initiated.

The definition for efficiency of the battery is shown in Equation 3.1. Figure 3.14 shows the battery efficiency as function of design range for the two different objectives. As the battery capacity increases, the C-rate decreases which in turn increases the efficiency. Since the total battery capacity is higher for aircraft designed for short ranges, the overall efficiency is higher as well.

$$\bar{\eta}_{batt} = \frac{\int P_{discharge}dt}{\Delta SOC \cdot Q + \int P_{charge}dt} \tag{3.1}$$
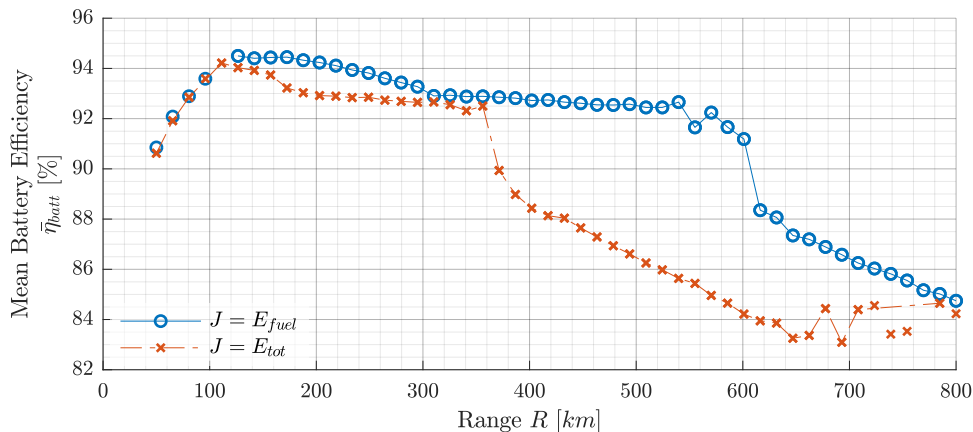
Figure 3.14: Comparison of mean battery efficiency between aircraft optimized for either minimal fuel or total energy and for ranges between 50 km to 800 km

Conclusions Drawn From the Minimization of Fuel and Energy Consumption for Different Ranges

In summary, several conclusions where drawn from the presented optimization study.

- The optimization routine works, as it produces systematically optimal designs that outperform designs made for a different objective.
- There is a difference in terms of performance and design when considering aircraft optimized for either minimal fuel or total energy consumption.
- At the long and short end of the ranges, the aircraft optimized for the two different objectives converge to the same design.
- During the optimization process, an important trade-off needs to be made: being aerodynamically efficient or being able to carry as much batteries to ensure an efficient power conversion.
- The most efficient range is the one where full electric cruise is possible. The fuel consumption only goes up for longer ranges, whereas the total energy consumption decreases for ranges longer than 200km.
- At some ranges, the gain in fuel economy of a different aircraft design is much higher compared to the associated loss in terms of total energy consumption.

3.2. Further study on objective influence

As introduced in the methodology, the objective of the optimization can be defined as a sum of fuel and battery energy, as again shown in Equation 3.2. Optimizing Equation 3.3 with $\beta = \frac{\alpha}{1-\alpha}$ leads to the same designs, however the function values are different as the ratio between fuel and battery energy are scaled different. The concept of α and β is further elaborated using Figures 3.15 and 3.16. When for example the price per kWh electrical energy is 0.2 €/kWh and the fuel price 4 €/L, the ratio α is 0.3 and β slightly lower than 0.5.

$$f(x) = \frac{E_{fuel}(x) + \beta \cdot E_{batt}(x)}{R} \tag{3.2}$$

$$f^*(x) = \frac{(1-\alpha) E_{fuel}(x) + \alpha \cdot E_{batt}(x)}{R} \tag{3.3}$$

In Figure 3.17 the results of various optimizations are shown in which the range and ratio between fuel and battery energy is varied using different values for α. As can be clearly seen, for long ranges the difference in objective value converges. This is because the minimum amount of batteries are carried and all priority is given to fuel as energy source. There is a certain α below which it is better to design for shorter ranges, and vice versa. To give more insight in the design, in Figures 3.18 and 3.18. As can be seen, batteries are less attractive to use when α increases; e.g. when the price of electricity goes up. Simultaneously the surface area decreases, as the total aircraft weight decreases and less maximum lift production is required.

Using a variation of multiple α's is very powerful for designers, as they can produce a limited number of aircraft designs and use that as a sort of lookup table for various interpretations of α.
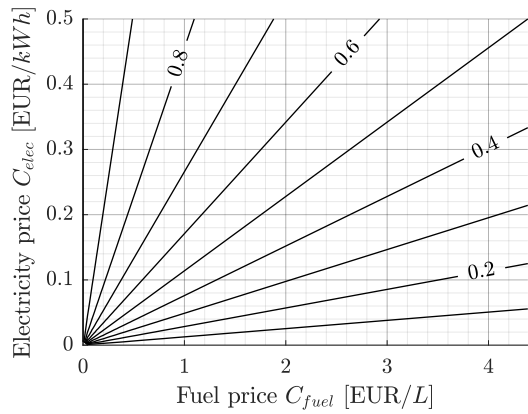
Figure 3.15: Influence of different fuel and electricity prices on the value of α
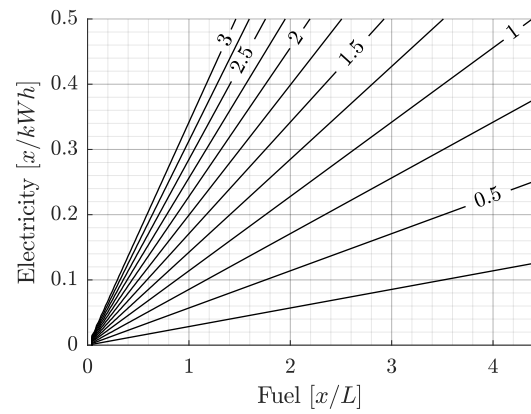
Figure 3.16: Influence of different fuel and electricity quantities on the value of β. The value x be cost, as in Figure 3.15, but also for example the amount of CO_2 that is emitted by the combustion of fuel and the production of electricity.
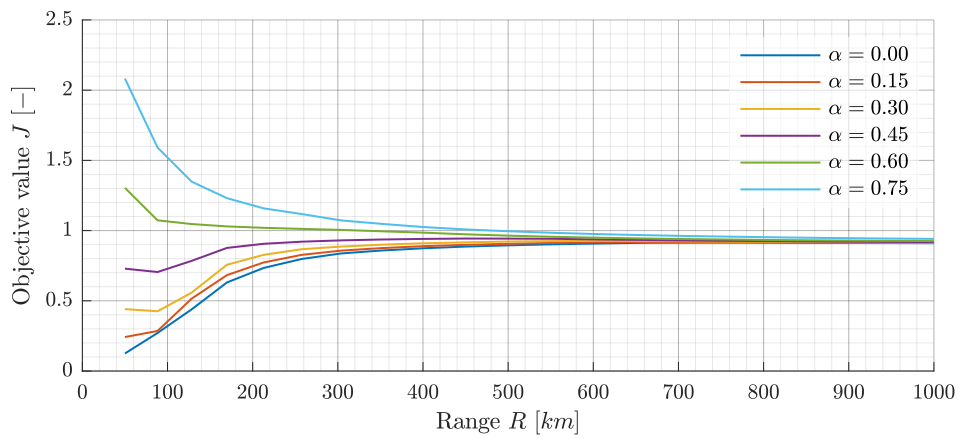
Figure 3.17: Influence of α on objective value J for different ranges.
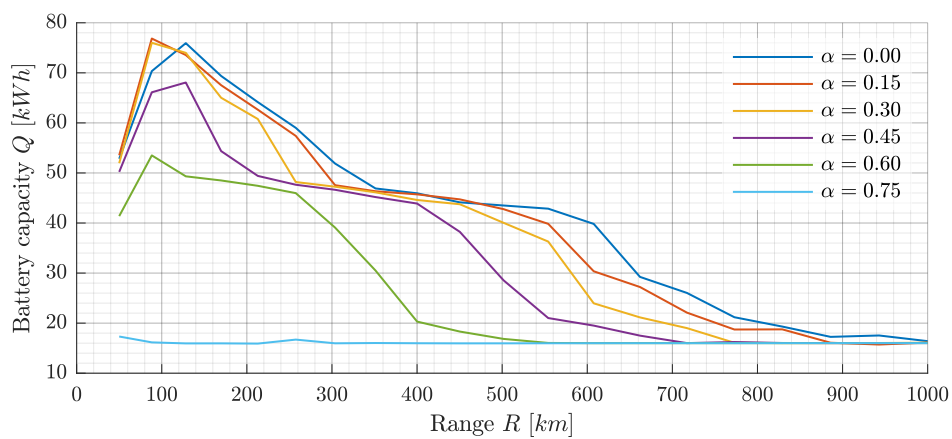
Figure 3.18: Influence of α on battery capacity Q for different ranges.
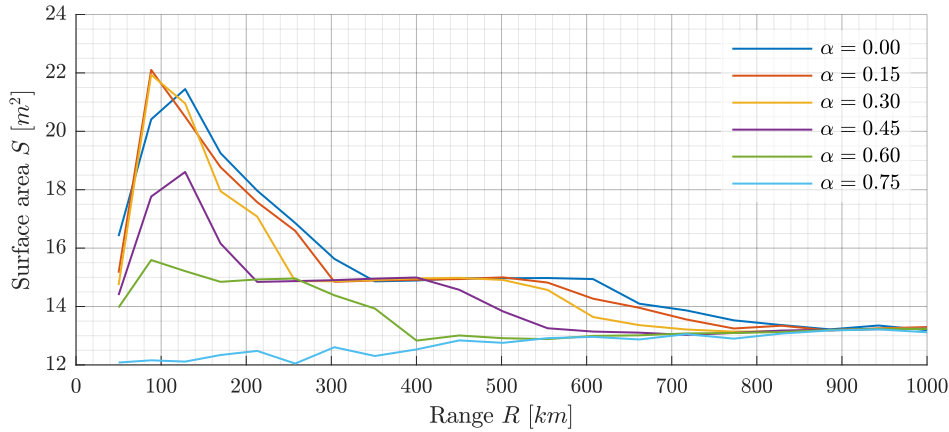
Figure 3.19: Influence of α on surface area S for different ranges.

3.3. Influence of Throttle During Hybrid Cruise on Performance

In the optimizations of section 3.1 the throttle of the internal combustion engine is either 100% during takeoff, climb, and the hybrid cruise, 0% during full electric cruise, or tuned exactly to the required power. However, it was found that the optimal throttle during any hybrid segment depends on the round trip efficiency of the battery and the actual power demand of the power management system. In summary, the following three throttle strategies are compared here: The baseline strategy (as used in section 3.1), is set to 100%. The adjustable throttle strategy: determined by the optimizer since it is added as design variable (recharging is possible here). Finally the strategy without recharging: the throttle is selected such that precisely enough power is delivered as required by the PMAD, without recharging. Figure 3.20 shows the throttle setting during hybrid cruise as result of multiple optimizations for different design ranges.
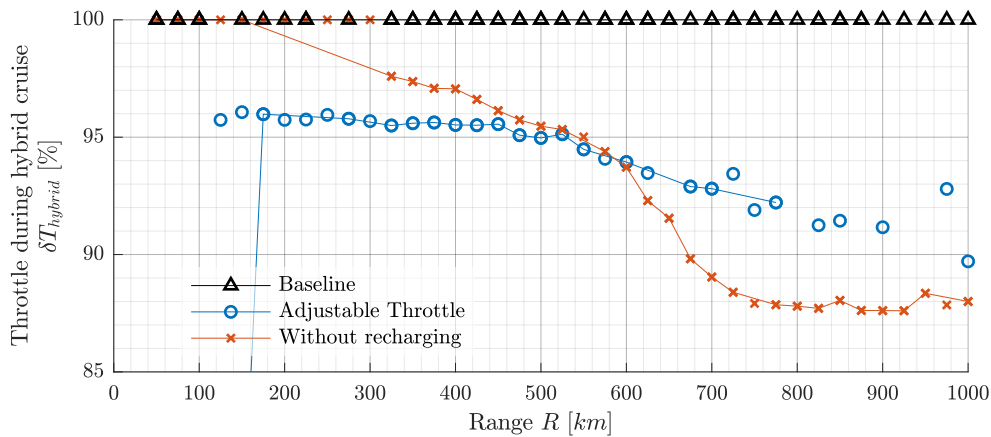
Figure 3.20: Comparison of internal combustion engine throttle during the hybrid cruise segment between aircraft optimized for minimal fuel consumption, using three different strategies, for ranges between 50 km and 1000 km. The baseline strategy (as used in section 3.1), is set to 100%. The adjustable throttle strategy: determined by the optimizer since it is added as design variable (recharging is possible here). Finally the strategy without recharging: the throttle is selected such that precisely enough power is delivered as required by the PMAD, without recharging.

As can be seen, the throttle selected by the optimizer for an adjustable throttle is slightly lower compared to the baseline runs. At the shortest ranges, a full electric operation of the aircraft is possible, hence the throttle is reduced to zero. For ranges close to 200 km the throttle that is selected is around 96%, which is very close to

the most optimal throttle of the internal combustion engine. For increasing ranges, the ideal throttle reduces towards approximately 92% for 1000 km. The reduction in throttle was to be expected, since the mean battery efficiency drops to approximately 85%, and hence the optimal throttle. The newly designed aircraft, with adjustable throttle, consume less fuel per kilometer compared to the optimal aircraft from the previous optimization with fixed full throttles, as can be seen in Figure 3.21. Logically, the relative fuel consumption drops drastically when a full electric climb is allowed, as is the case for the very short ranges. The improvement in terms of fuel consumption for ranges longer than 150 km are with only 1% relatively small. When no excess power is produced at all by the internal combustion engine, and hence when the battery is not recharged, the fuel economy improves as well compared to the baseline with a full throttle hybrid cruise. The improvements in this case are within 0.5%.
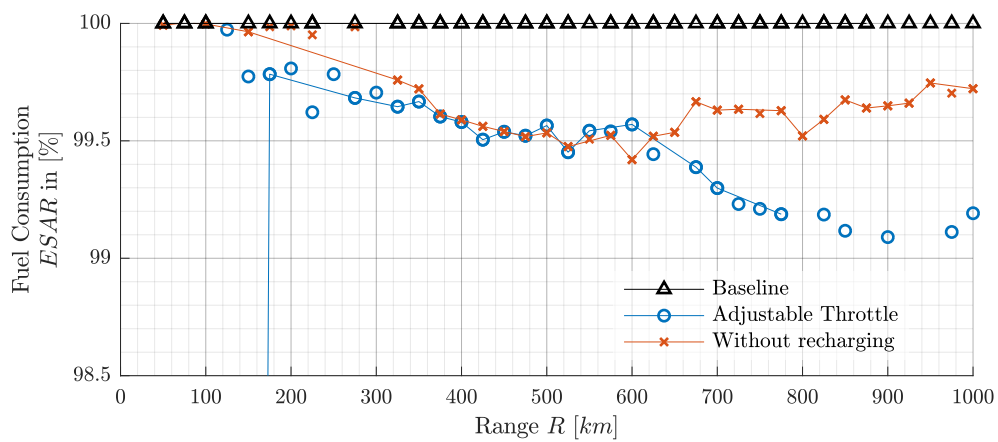
Figure 3.21: Comparison of fuel consumption between aircraft optimized for minimal fuel consumption, using three different strategies, for ranges between 50 km and 1000 km. The fuel consumption of the baseline has been set to 100%

The differences between the three investigated strategies are more pronounced when comparing the electrification of the cruise, as shown in Figure 3.22. The electrification of the cruise for aircraft with design ranges of ±900 km is around 10%, 5% and 0% for aircraft with a full throttle, optimized throttle, and no recharging respectively.
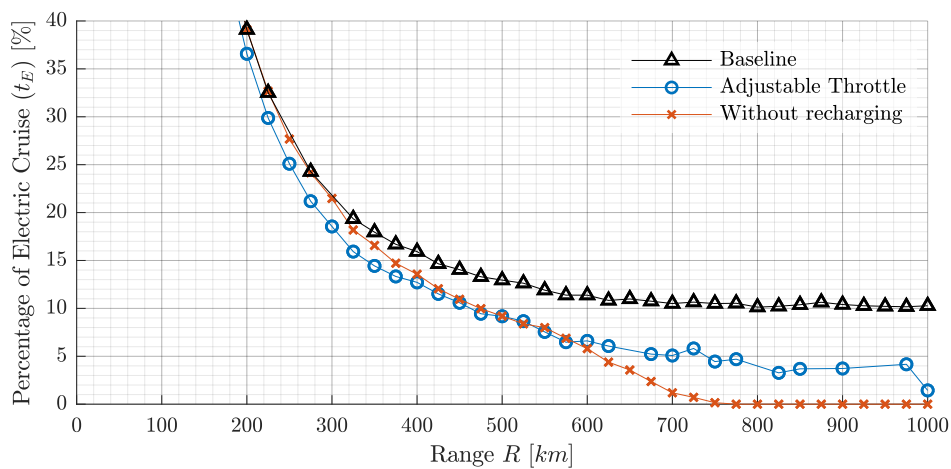
Figure 3.22: Comparison of electrification of the cruise phase between aircraft optimized for minimal fuel consumption, using three different strategies, for ranges between 50 km and 1000 km.

3.4. Influence of Cruise Speed on Optimal Design and Performance

In this section, the influence of cruise speed on the optimal design, operation, and performance is investigated. As the desired cruise speed increases, the drag and hence the power required by the power management system increases. When the power that is required by the power management system during cruise is higher than what the internal combustion engine is able to deliver, additional electrical power from batteries is required. Consequently, the minimal total battery capacity increases significantly with an increasing design range. In section 3.1 it was discovered that aerodynamic efficiency is preferred over batteries for longer ranges. At a certain point, the increase in required total energy due to the weight of additional batteries is more than the energy that can be stored in those batteries. When this is the case, no feasible combination of design variables exist that allow for the desired range. To illustrate this, the maximum range that can be flown is analyzed for different cruise velocities. The result of this study is presented in Figure 3.23.
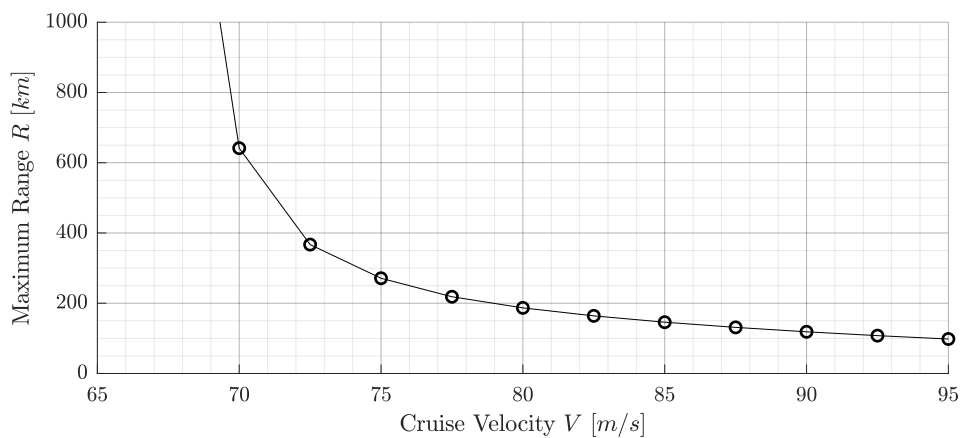
Figure 3.23: Influence of cruise speed on maximum range. Each data point has been obtained by optimizing for maximum range using the design variables used in section 3.1 for a range of cruise velocities at a cruise altitude of 2500 m.

Clearly, the maximum range decreases drastically with increasing cruise velocity. There are two main ways to solve the problem of maximum range at higher cruise velocities: increasing the maximum power of the internal combustion engine and increasing the battery gravimetric energy density. The latter is possible to some extend, however, there are two main drawbacks. Firstly, the price of batteries increase rapidly with increasing gravimetric energy density. Secondly, the maximum commercial gravimetric energy density is relatively close to currently selected value since state of the art batteries are assumed and this limit only increases with approximately 8% per year. Therefore, the maximum power output of the internal combustion engine has been introduced as additional design variable as part of the study in this section.

Furthermore, as the cruise velocity increases it becomes more and more beneficial to increase the cruise altitude. This is because the amount of drag decreases with increasing altitude. Increasing the cruise altitude could be especially interesting for longer design ranges since it is more likely that the benefits of increased aerodynamic efficiency outweigh the invested energy during the climb phase. Due to the multidisciplinary nature of this problem, the cruise altitude has also been included as a design variable.

Lastly, the maximum power output of the electric motor has been added to the design variables. By doing so, the power loading of the aircraft effectively becomes a design variable that increases the design space. Because not all effects of a more powerful electric motor are taken into account, this study is more conceptual

compared to the previous studies of this thesis. In summary, the following design variables have been added to the optimization:

- Maximum power of the internal combustion engine during cruise $P_{ICE,max}$
- Maximum power of the electric motor $P_{EM,max}$
- Cruise altitude h_{cruise}

It must be noted that the analysis modules of the internal combustion engine and the electric motor are rubberized to scale with maximum power output. Hence, the influence of a more powerful engine will reflect in added weight. This influence is assumed linear as the specific power of the baseline engine and motor is taken as constant.

The resulting energy specific air ranges are shown in Figure 3.24. As can be seen, the energy dissipation through drag increases with increasing cruise velocity. This was to be expected as drag increases with cruise speed. The fuel consumption also increases with cruise speed, as the largest fraction of energy comes from fuel. As the conversion efficiency from fuel to useful power is very low, the absolute difference in terms of fuel energy consumption is much higher compared to the absolute increase in energy dissipation through drag.
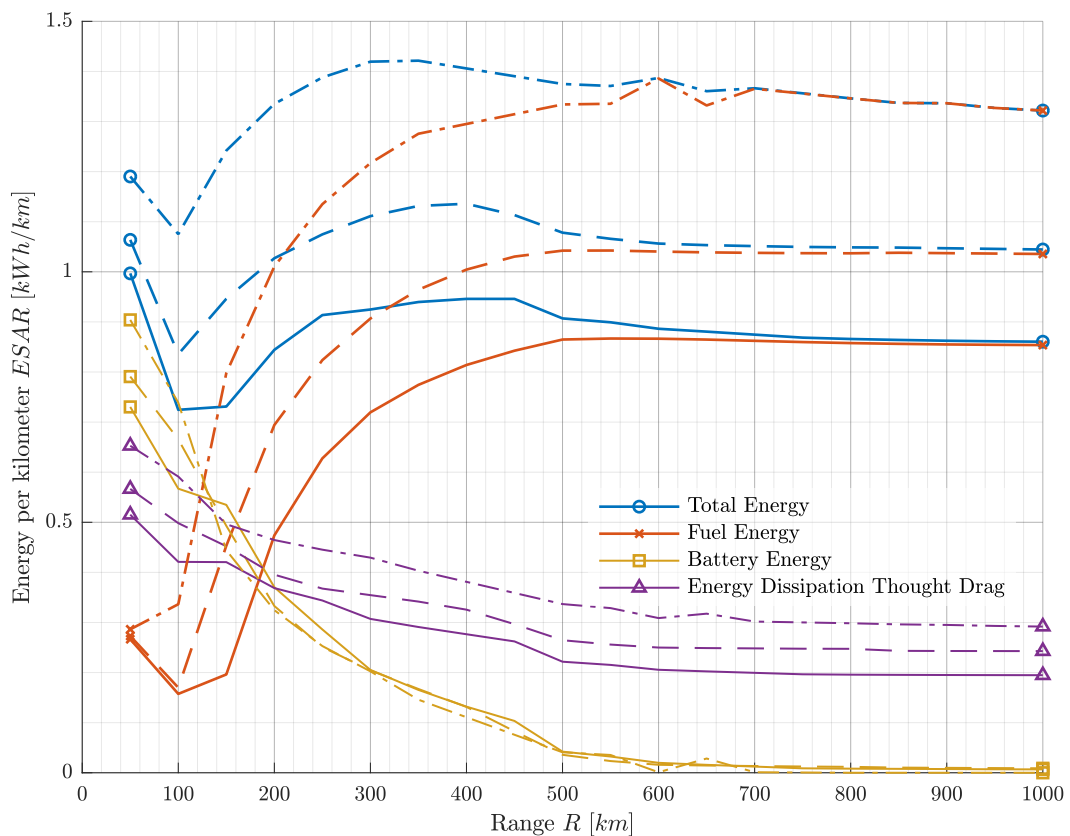
Figure 3.24: Comparison of total, fuel, battery, and in the air dissipated energy between aircraft optimized for minimal fuel consumption with three different cruise velocities at design ranges between 50 km and 1000 km. The different line styles represent different cruise velocities: ——is 60 m/s, — — — is 75 m/s, and — · — · is 90 m/s.

In Figure 3.25, the electrification of the cruise phase is shown. The electrification drops quickly with increasing design range. Furthermore, it drops quickly with increasing cruise velocity.
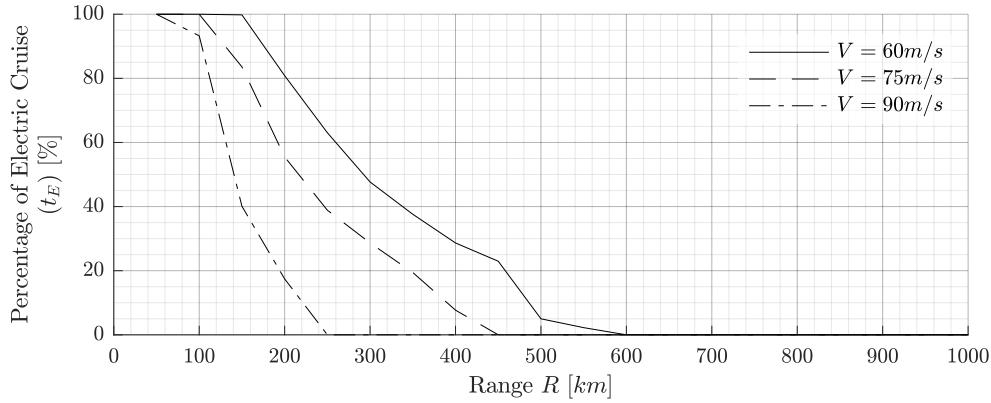
Figure 3.25: Comparison of electrification of the cruise phase between aircraft optimized for minimal fuel consumption with three different cruise velocities and ranges between 50 km and 1000 km.

The maximum power of the internal combustion engine is shown in Figure 3.26. At the very short end of the design ranges, the maximum power of the internal combustion engines drops to zero. This is because a full electric operation is possible, and there is no need for an internal combustion engine. With increasing design range, the maximum power increases and converges towards a specific value. The maximum power at 1000 km is approximately 56 kW, 85 kW, and 125 kW for cruise velocities of 60 m/s, 75 m/s, and 90 m/s respectively. Because the cruise phase of aircraft with design ranges longer than 500 km is performed solely on the internal combustion engine, the increase in drag is translated directly to an increase in maximum power of the internal combustion engine.
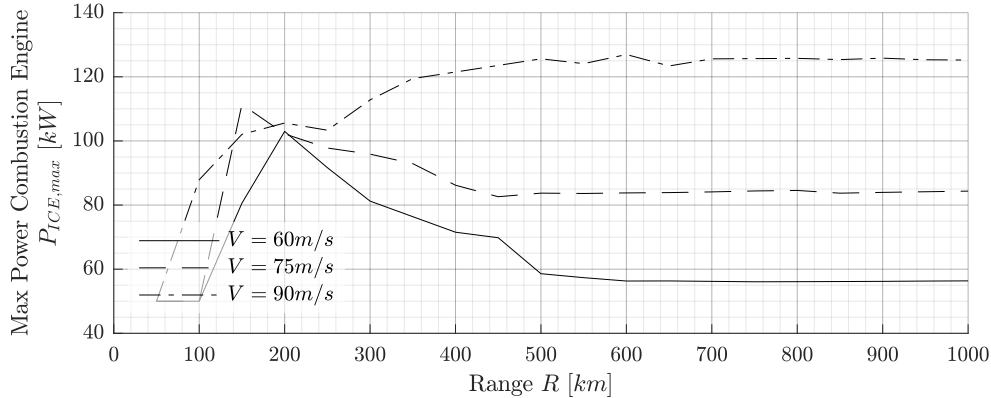
Figure 3.26: Comparison of maximum internal combustion engine power between aircraft optimized for minimal fuel consumption with three different cruise velocities and ranges between 50 km and 1000 km.

One of the hypothesis before performing the optimizations was that it is beneficial to increase the cruise altitude when flying with a higher velocity. However, it was also speculated that for this to happen, the range must be sufficiently large so that the energy invested during the climb phase are outweighed by the benefits of flying more efficient. As can be seen in Figure 3.27, this is exactly what is found during the optimization. The optimal cruise altitude increases with range as well as cruise velocity.

The last additional variable in the optimizations of this section is the maximum power output of the electric engine. By increasing the maximum power the aircraft mass can be increased while satisfying the takeoff constraint. Furthermore, when the takeoff field length at maximum power output is shorter than the maximum
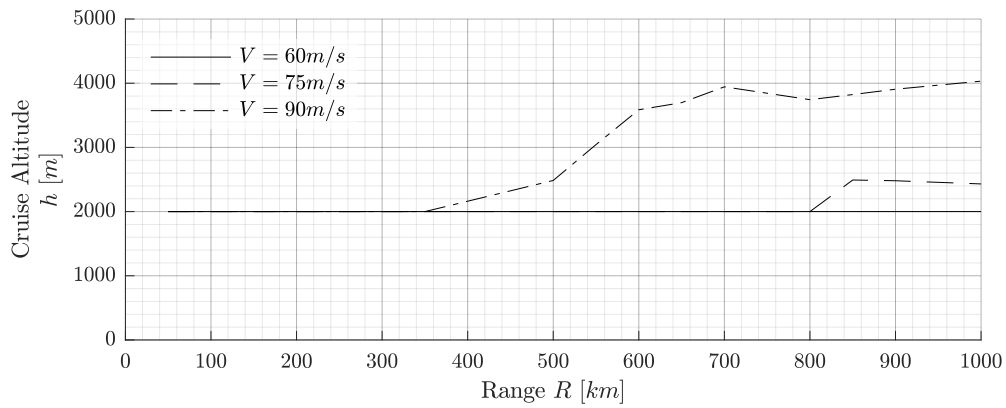
Figure 3.27: Comparison of cruise altitude between aircraft optimized for minimal fuel consumption with three different cruise velocities and ranges between 50 km and 1000 km.

required takeoff field length, it could be beneficial to reduce te maximum power since this yields a lighter engine. Any reduction in aircraft mass translates to less aerodynamic drag and therefore a more efficient aircraft. As can be seen in Figure 3.28, the maximum power output for short ranges is increased to the maximum value of 300 kW whereas it is decreased to approximately 165 kW for long design ranges. It is interesting to see that the optimal maximum power output of the electric motor is not really sensitive to cruise velocity.
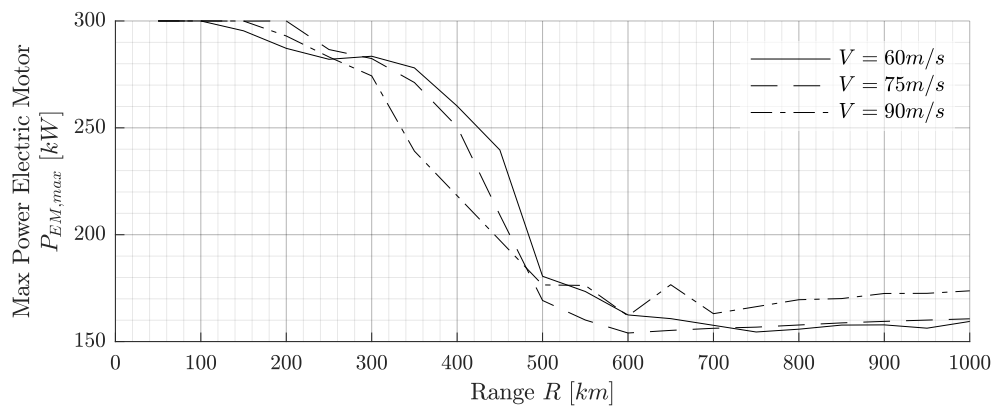
Figure 3.28: Comparison of maximum electric motor power between aircraft optimized for minimal fuel consumption with three different cruise velocities and ranges between 50 km and 1000 km.
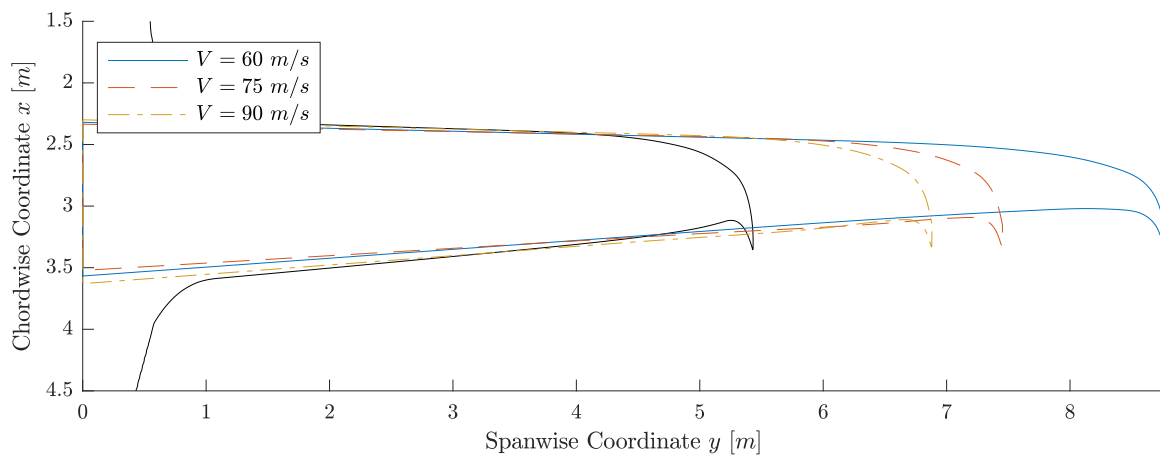
Figure 3.29: Wing planform of aircraft with a design range of 500 km and cruise velocities of 60 m/s, 75 m/s, and 90 m/s

3.5. Influence of Battery Specific Energy Density on Fuel Consumption

A large part of the conceptual design phase consists of solving the energy balance problem: the amount of energy that is required for flight needs to be stored somehow within the aircraft. For hybrid-electric aircraft, the solution to this energy balance problem involves a trade off between fuel and batteries. The conversion from energy to useful power is much more efficient for batteries compared to fuel, however, the major downside of batteries is their relatively low gravimetric energy density. As battery technology evolves, the energy density increases. Over the past 30 years, the energy density of batteries has increased with approximately 8% per year. Therefore, the downsides of using batteries as energy storage devices decreases each year. To analyze the effect of this increasing battery technology a set of optimizations have been performed in which the gravimetric energy density is increased. The densities that have been analyzed are 130, 175, 250, and 400 Wh/kg. Following the trend of the past 30 years, the energy density of 400 Wh/kg is expected to be reached within 15 years. The results in terms of energy are presented in Figure 3.30.

The fuel consumption decreases with increasing energy density. Because the overall power conversion is much more efficient when using more batteries, the total amount of required energy decreases as well. At a design range of 100 km, the amount of energy that is stored in batteries decreases with increasing battery energy density. For longer design ranges such as 500 km for example, the opposite is true. The reason for this lies in the fact that even with 130 Wh/kg a full electric cruise is possible for a design range of 100 km. Therefore, with increasing battery energy density the aircraft becomes lighter, produces less drag, and thus less energy is required for flight. Furthermore, the design range at which the lowest fuel consumption can be realized increases. As can be seen from Figure 3.31, the electrification of the cruise increases because the penalty of using batteries for energy storage decreases with increasing energy density.

To aid the comparison between Figures 3.30 and 3.31, some of the data has been presented in Table 3.2. The maximum full electric range coincides with the lowest fuel consumption per kilometer. It is always beneficial in terms of fuel (and total energy) consumption to install the best batteries possible, because their energy density is higher. Although this is true, the improvements that can be achieved when full electric cruise is already possible are significantly lower compared to when this is not the case.

Lastly, a small study has been performed in which the objective was set to maximize the full electric range and analyzed for various battery gravimetric energy densities ranging from 100 Wh/kg to 600 Wh/kg. As can be
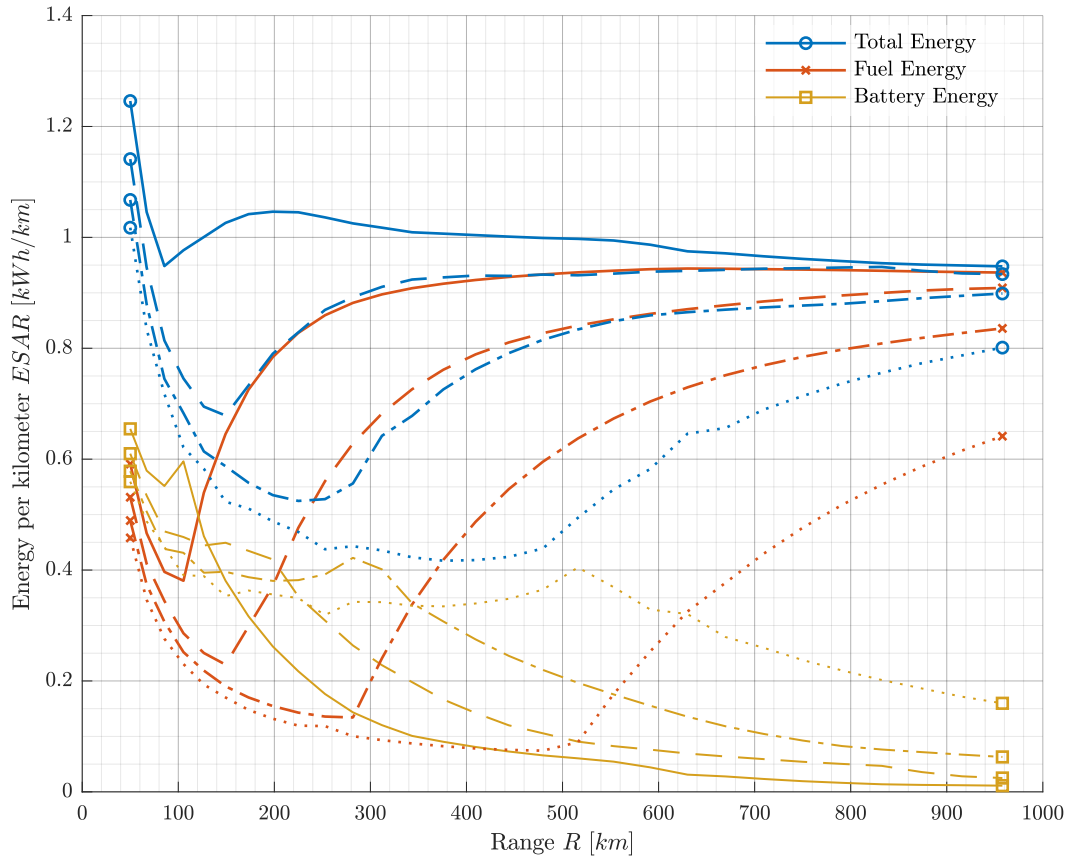
Figure 3.30: Energy sources per kilometer versus design range for different battery specific energy densities. The lines correspond to the following energy densities: ——130, $- - -$ 175, $- \cdot - \cdot$ 250, and $\cdots\cdots$ 400 in Wh/kg.
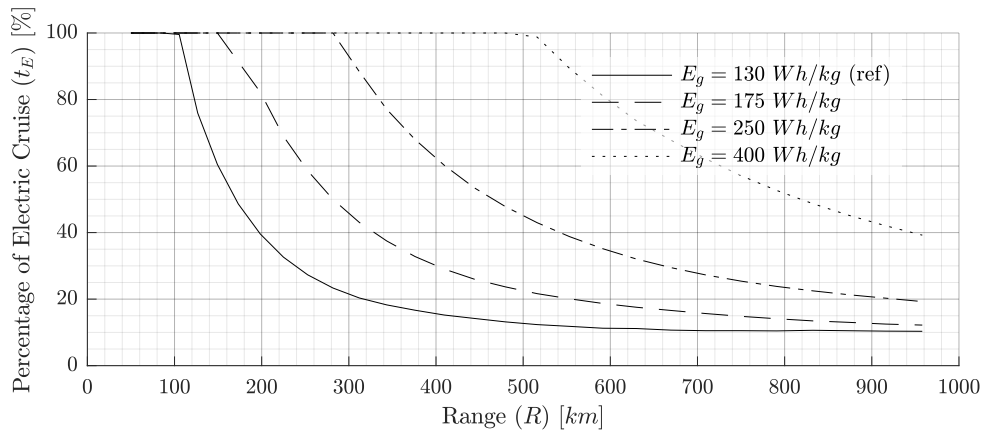
Figure 3.31: Electrification of the cruise phase versus design range for different battery specific energy densities. The lines correspond to the following energy densities: ——130, $- - -$ 175, $- \cdot - \cdot$ 250, and $\cdots\cdots$ 400 in Wh/kg.

seen from the results in Figure 3.32, the relation between the energy density and maximum full electric range is virtually linear. The linear fit through the optimization results, shown in Equation 3.4, has a RMSE of just 0.6564 km.

Table 3.2: Quantified differences between various battery technology levels

Case	1	2	3	4	Units
Battery Specific Energy	130	175	250	400	Wh/kg
Max Full Electric Range	98	169	285	512	km
Lowest $ESAR^*_{Fuel}$	370	230	134	76	Wh/km
$ESAR^*_{Fuel}$ at 200 km	784 (100%)	371 (47%)	155 (20%)	133 (17%)	Wh/km
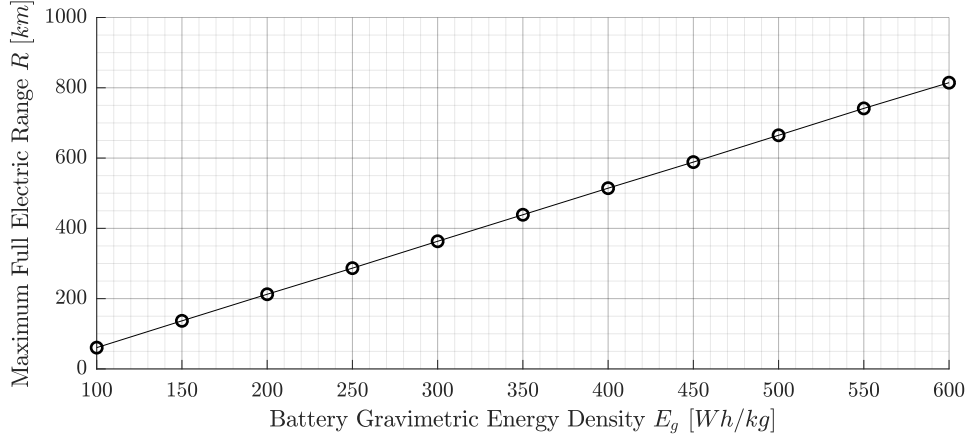
Figure 3.32: Influence of battery gravimetric energy density on the maximum full electric range

$$R_{max,E} = 1.5E_g - 90 \tag{3.4}$$

4

Conclusions and Recommendations

The goal of this research was to define the implications of using hybrid electric propulsion systems in general aviation aircraft, focusing on performance optimization. This is achieved by performing optimization studies of such an aircraft and by identifying what design and mission changes lead to better performance. The methodology that has been developed mainly consists of modeling tools for general aviation hybrid-electric propulsion aircraft. It focuses on the modeling of the hybrid propulsion system components since those are fundamentally different from the conventional systems. Every part of the tool is either verified with experimental data or has already been verified in literature.

4.1. Conclusions

Several conclusions can be drawn from the results of the multiple studies presented in this document. First, there is a difference in terms of optimal configuration and operation of aircraft when designed specifically for minimal fuel or for minimal total energy. The optimizations lead to a maximum difference in terms of energy consumption per kilometer of around 5% between ranges of 100 and 600 km. When varying the importance between minimizing fuel or battery energy, two interesting conclusions can be made; Firstly, for longer ranges, the objective values converge to same value. Secondly, flying short distances is most optimal for fuel minimization whereas flying long distances is most optimal for battery minimization.

Traditionally, aircraft designers always had to focus on the minimization of fuel consumption and thus arrive at aircraft designs that are aerodynamically most efficient and as light as possible. With hybrid-electric propulsion systems, as demonstrated, the best aircraft design is not necessarily one of these two. The developed modeling tool is capable of producing aircraft designs that are consistently most optimal in terms of their objectives.

An important trade off is part of the optimization routine: designing for aerodynamic efficiency versus the ability to carry batteries. It has been shown that aircraft optimized for fuel consumption carry systematically more batteries compared to aircraft optimized for total energy consumption, always leading to a heavier aircraft with larger wings. The opposite can be observed by aircraft designed for total energy consumption; they are always aerodynamically more efficient, lighter, and have smaller wings. Regardless of objective, the aerodynamic efficiency becomes more important for an increasing range while the ability to carry batteries decreases.

The fuel consumption per kilometer increases with range above the full electric range of 100 km, over all analyzed ranges, but approaches convergence around 1000 km. The total energy per kilometer steadily decreases for design ranges longer than 400 km.

Three variables to determine the amount of hybridization in terms of power and energy have been defined. Firstly, a climb coefficient that determines the rate of climb as a fraction of the maximum rate of climb at each moment during the climb. Secondly, the electrification, which determines the fraction of the cruise that is to be performed in a hybrid mode. Lastly, a hybridization factor that changes the throttle of the internal combustion engine from 0% to 100%. By using these three variables, there is no need for the use of constraint functions for the propulsion systems since any combination of these variables leads to an inherently feasible design. The required battery power at each moment in time, which is the result of these operational variables, leads to a certain minimal battery capacity and weight capable of delivering that power. It is shown that the following trade-off is made by the optimizer: consuming battery energy during climb to reduce the time to climb and hence the dissipation through drag or consuming battery energy during cruise to reduce fuel consumption.

Given a certain required power at the power management system, there exist one specific throttle that leads to the maximum effective efficiency of the internal combustion engine. This throttle depends on the round trip efficiency of the battery. With a given round trip efficiency of 95%, the effective efficiency increase of the internal combustion engine is 0.9% when the required throttle is 80%. This increase is relatively low for an internal combustion engine that is over sized by 20%. Optimizing the throttle during cruise for aircraft with an fixed internal combustion engine of 73 kW leads to a throttle of around 92% for ranges around 1000 km. The improvement in terms of fuel consumption is slightly less than 1% compared to a full-throttle optimization. Furthermore, the improvement when not recharging at all is around 0.5%. The percentages of electric cruise however are around 10%, 4%, and 0% for the full throttle, optimized throttle, and zero excess throttle strategies respectively. When the internal combustion engine is scalable, the optimizer always makes sure that the most optimal throttle matches the power requirements during cruise.

The maximum possible range is highly determined by the required cruise velocity, given a fixed internal combustion engine. By scaling the internal combustion engine such that it is powerful enough to deliver the required power for cruise, the maximum range can be significantly increased. The maximum power of the internal combustion engine in aircraft optimized for a design range of 1000 km at 60 m/s or 90 m/s is 56 kW and 125 kW respectively. Furthermore, the optimal cruise altitude is found to be increasing with range and cruise velocity. The optimal wingspan decreases with increasing cruise speeds. Also, increasing the maximum power output of the electric motor enables a higher battery capacity when the takeoff field length is constraining the design and decreasing it leads to weight and energy savings.

When increasing the battery specific energy, the energy consumption per kilometer decreases for all ranges. The battery specific energy leads to a certain maximum range that can be flown fully electric. This range corresponds with the lowest energy specific air range. Also, it correlates linearly with the specific energy. When designing a hybrid electric aircraft for a range of for example 250 km, it is beneficial to install batteries with an energy density of 225 Wh/kg. Installing batteries with higher energy densities does provide a slightly better fuel energy consumption, however, the difference is so low that it does not weigh against the increased cost of these better performing batteries. Since the lowest $ESAR^*_{Fuel}$ coincides with the maximum range at which a full elec-

tric cruise is possible, the linear relation between specific energy and maximum full electric range can be used to determine the most effective battery technology for the desired range. This relation is of great use for aircraft designers to very quickly explore design options.

Generalization of the Conclusions

All the results and conclusions that have been presented so far are specific for this reference aircraft, including its components. However, the same relations should hold true for different energy sources that share the same highly efficient power conversion at the cost of a low specific energy density.

4.2. Recommendations

The scope of this research was to investigate new conceptual design strategies leading to optimal performance of hybrid-electric general aviation aircraft. Due to the time constraints of this research, unfortunately not everything could be included and assumptions were required to make. Moreover, during this research, various ideas were generated that could be the basis of new research. Therefore, the following points are recommended to take into account in further research.

- First of all, it is recommended to include a detailed structural analysis of the wing in future research. Certain designs carry around 500 kg of batteries in the wing, which on one hand causes load relief during cruise, but it also increases the forces in gravity direction during landing and ground operations. The influence of the overall effect on the wing weight needs to be determined. Furthermore, aero-elastic effects should be taken into account since its importance will be more pronounced due to the heavy batteries in the wings.

- Several potential problems due to the placement of batteries could arise in the field of stability and control because the weight of batteries could shift the center of gravity and increase the inertia. Therefore, it is recommended that in future research these influences are investigated in more detail.

- Since the maximum lift that can be generated by the aircraft plays a large role in the performance of hybrid-electric aircraft, it is recommended to further investigate the high-lift characteristics of the aircraft. For example by using higher-fidelity methods for the determination of the influence of the flaps on the maximum lift coefficient and its influence on the aerodynamic efficiency of the complete wing.

- The airfoil shape should be included in the optimization to be more flexible in enhancing high-lift capabilities and adjust the optimal shape for different cruise speeds and flight altitudes.

- Lastly, it is recommended to investigate the influence of scalable models of all propulsion system components on their performance characteristics. A logical place to start is with the internal combustion engine and electric motor performance characteristics. Lastly, the influence of accurate performance modeling and scaling of the converters are recommended. When the loads on the battery increase, it could be the case that this affects the efficiency of the converters. It can be reasoned that the performance maps of the converters influence the design and control strategies; the magnitude, however, is fully unknown by now.

Bibliography

[1] Kevin R. Antcliff, Mark D. Guynn, Ty V. Marien, Douglas P. Wells, Steven J. Schneider, and Michael J. Tong. Mission Analysis and Aircraft Sizing of a Hybrid-Electric Regional Aircraft. In *54th AIAA Aerospace Sciences Meeting*, number January, pages 1–18, Reston, Virginia, jan 2016. American Institute of Aeronautics and Astronautics. ISBN 978-1-62410-393-3. doi: 10.2514/6.2016-1028. URL http://arc.aiaa.org/doi/10.2514/6.2016-1028.

[2] Marty K. Bradley and Christopher K. Droney. Subsonic Ultra Green Aircraft Research: Phase I Final Report. Technical Report April, Boeing Research & Technology, 2011.

[3] Min Chen and G.A. Rincon-Mora. Accurate Electrical Battery Model Capable of Predicting Runtime and I–V Performance. *IEEE Transactions on Energy Conversion*, 21(2):504–511, jun 2006. ISSN 0885-8969. doi: 10.1109/TEC.2006.874229. URL http://ieeexplore.ieee.org/document/1634598/.

[4] Gokcin Cinar, Dimitri N. Mavris, Mathias Emeneth, Alexander Schneegans, Carsten Riediger, Yann Fefermann, and Askin T Isikveren. Sizing, Integration and Performance Evaluation of Hybrid Electric Propulsion Subsystem Architectures. In *55th AIAA Aerospace Sciences Meeting*, number January, pages 1–18, Reston, Virginia, jan 2017. American Institute of Aeronautics and Astronautics. ISBN 978-1-62410-447-3. doi: 10.2514/6.2017-1183. URL http://arc.aiaa.org/doi/10.2514/6.2017-1183.

[5] Dennis Doerffel and Suleiman Abu Sharkh. A critical review of using the Peukert equation for determining the remaining capacity of lead-acid and lithium-ion batteries. 155:395–400, 2006. doi: 10.1016/j.jpowsour.2005.04.030.

[6] Mark Drela. XFOIL, . URL http://web.mit.edu/drela/Public/web/xfoil/.

[7] Mark Drela. AVL, .

[8] Mark Drela. *Two-dimensional transonic aerodynamic design and analysis using the Euler equations*. PhD thesis, Massachusetts Institute of Technology, 1985.

[9] Mark Drela. XFOIL: An analysis and design system for low Reynolds number airfoils. *Conference on Low Reynolds Number Airfoil Aerodynamics*, 54, 1989. ISSN 01765035. doi: 10.1007/978-3-642-84010-4_1. URL http://link.springer.com/chapter/10.1007/978-3-642-84010-4{_}1.

[10] Mark Drela. Integral boundary layer formulation for blunt trailing edges. *7th AIAA Applied Aerodynamics Conference*, pages 59–68, 1989. doi: doi:10.2514/6.1989-2166.

[11] Mark Drela. Implicit Implementation of the Full eˆn Transition Criterion. In *21st AIAA Applied Aerodynamics Conference*, number June, page 4066, Reston, Virigina, jun 2003. American Institute of Aeronautics and Astronautics. doi: 10.2514/6.2003-4066. URL http://arc.aiaa.org/doi/abs/10.2514/6.2003-4066.

[12] Mark Drela and Michael Bryce Giles. Viscous-inviscid analysis of transonic and low Reynolds number airfoils. *AIAA Journal*, 25(10):1347–1355, oct 1987. doi: 10.2514/3.9789. URL http://arc.aiaa.org/doi/abs/10.2514/3.9789.

[13] A Elham, G La Rocca, and M J L Van Tooren. Development and implementation of an advanced , design-sensitive method for wing weight estimation. *Aerospace Science and Technology*, 29(1):100–113, 2013. ISSN 1270-9638. doi: 10.1016/j.ast.2013.01.012. URL http://dx.doi.org/10.1016/j.ast.2013.01.012.

[14] Christian Friedrich and P. A. Robertson. Hybrid-electric propulsion for automotive and aviation applications. *CEAS Aeronautical Journal*, 6(2):279–290, jun 2015. ISSN 1869-5582. doi: 10.1007/s13272-014-0144-x. URL http://dx.doi.org/10.1007/s13272-014-0144-xhttp://link.springer.com/10.1007/s13272-014-0144-x.

[15] Christian Friedrich and P.A. Robertson. Hybrid-Electric Propulsion for Aircraft. *Journal of Aircraft*, 52(1): 176–189, jan 2015. ISSN 0021-8669. doi: 10.2514/1.C032660. URL `http://arc.aiaa.org/doi/10.2514/1.C032660`.

[16] Snorri Gudmundsson. *General Aviation Aircraft Design: Applied Methods and Procedures*. Elsevier Inc., 2014. ISBN 978-0-12-397308-5.

[17] O Gur and A Rosen. Comparison between blade-element models of propellers. *The Aeronautical Journal*, 112(1138):689–704, dec 2008. ISSN 0001-9240. doi: 10.1017/S0001924000002669. URL `https://www.cambridge.org/core/product/identifier/S0001924000002669/type/journal{_}article`.

[18] Frederick G Harmon, Andrew A Frank, and Jean-jacques Chattot. Conceptual Design and Simulation of a Small Hybrid-Electric Unmanned Aerial Vehicle. *Journal of Aircraft*, 43(5):1490–1498, sep 2006. ISSN 0021-8669. doi: 10.2514/1.15816. URL `http://arc.aiaa.org/doi/abs/10.2514/1.15816http://arc.aiaa.org/doi/10.2514/1.15816`.

[19] J Y Hung and L F Gonzalez. Progress in Aerospace Sciences On parallel hybrid-electric propulsion system for unmanned aerial vehicles. *Progress in Aerospace Sciences*, 51:1–17, 2012. ISSN 0376-0421. doi: 10.1016/j.paerosci.2011.12.001. URL `http://dx.doi.org/10.1016/j.paerosci.2011.12.001`.

[20] IPCC. Aviation and the Global Atmosphere - Summary for Policymakers. Technical report, 1999.

[21] Askin T Isikveren, Clément Pornet, Patrick Christoph Vratny, and Michael Schmidt. Conceptual studies of future hybrid-electric regional aircraft. Technical report, 2015.

[22] Kokam. Superior Lithium Polymer Battery Technical Specification: SLPB70460330, 2009.

[23] Brenda M Kulfan. "CST" Universal Parametric Geometry Representation Method With Applications to Supersonic Aircraft. In *International Conference on Flow Dynamics*, 2007.

[24] J. Mariens, A. Elham, and M. J. L. van Tooren. Quasi-Three-Dimensional Aerodynamic Solver for Multidisciplinary Design Optimization of Lifting Surfaces. *Journal of Aircraft*, 51(2):547–558, 2014. ISSN 0021-8669. doi: 10.2514/1.C032261. URL `http://arc.aiaa.org/doi/abs/10.2514/1.C032261`.

[25] Joaquim R R A Martins and Andrew B Lambe. Multidisciplinary Design Optimization: A Survey of Architectures. *AIAA Journal*, 51(9):2049–2075, sep 2013. ISSN 0001-1452. doi: 10.2514/1.J051895. URL `http://arc.aiaa.org/doi/10.2514/1.J051895`.

[26] Robert A. McDonald. Electric Propulsion Modeling for Conceptual Aircraft Design. In *52nd Aerospace Sciences Meeting*, number January, pages 1–19, Reston, Virginia, jan 2014. American Institute of Aeronautics and Astronautics. ISBN 978-1-62410-256-1. doi: 10.2514/6.2014-0536. URL `http://arc.aiaa.org/doi/10.2514/6.2014-0536`.

[27] Jan Middel. *Development of a computer assisted toolbox for aerodynamic design of aircraft at subcritical conditions with applications to three-surface and canard aircraft*. Phd, Technical University of Delft, 1992.

[28] Tomas Moller. A Fast Triangle-Triangle Intersection Test. *Journal of Graphics Tools*, 2(2), 1997.

[29] Taewoo Nam. *A generalized sizing method for revolutionary concepts under probabilistic design constraints*. PhD thesis, Georgia Institute of Technology, 2007.

[30] Taewoo Nam, Danielle Soban, and Dimitri Mavris. Power Based Sizing Method for Aircraft Consuming Unconventional Energy. In *43rd AIAA Aerospace Sciences Meeting and Exhibit*, number January, pages 1–14, Reston, Virigina, jan 2005. American Institute of Aeronautics and Astronautics. ISBN 978-1-62410-064-2. doi: 10.2514/6.2005-818. URL `http://arc.aiaa.org/doi/10.2514/6.2005-818`.

[31] Taewoo Nam, Danielle Soban, and Dimitri Mavris. A Generalized Aircraft Sizing Method and Application to Electric Aircraft. In *3rd International Energy Conversion Engineering Conference*, number August, page 18, Reston, Virigina, aug 2005. American Institute of Aeronautics and Astronautics. ISBN 978-1-62410-062-8. doi: 10.2514/6.2005-5574. URL `http://arc.aiaa.org/doi/abs/10.2514/6.2005-5574http://arc.aiaa.org/doi/10.2514/6.2005-5574`.

[32] Jorge Nocedal and Stephen J Wright. *Numerical Optimization.* Springer-Verlag, 1999. ISBN 0387987932.

[33] Christopher Perullo and Dimitri Mavris. A review of hybrid-electric energy management and its inclusion in vehicle sizing. *Aircraft Engineering and Aerospace Technology*, 86(6):550–557, sep 2014. ISSN 0002-2667. doi: 10.1108/AEAT-04-2014-0041. URL http://www.scopus.com/inward/record.url?eid=2-s2.0-84913552386{&}partnerID=tZOtx3y1{%}5Cnhttp://www.emeraldinsight.com/doi/abs/10.1108/AEAT-04-2014-0041http://www.emeraldinsight.com/doi/10.1108/AEAT-04-2014-0041.

[34] Christopher A Perullo, David R Trawick, and Dimitri N Mavris. Assessment of Engine and Vehicle Performance Using Integrated Hybrid-Electric Propulsion Models. *Journal of Propulsion and Power*, 32(6):1305–1314, nov 2016. ISSN 0748-4658. doi: 10.2514/1.B35744. URL http://arc.aiaa.org/doi/10.2514/1.B35744.

[35] Pipistrel. Proprietary information obtained from Pipistrel, 2018.

[36] C. Pornet and A. T. Isikveren. Conceptual design of hybrid-electric transport aircraft. *Progress in Aerospace Sciences*, 79:114–135, 2015. ISSN 03760421. doi: 10.1016/j.paerosci.2015.09.002. URL http://dx.doi.org/10.1016/j.paerosci.2015.09.002.

[37] Clément Pornet, Corin Gologan, Patrick C. Vratny, Arne Seitz, Oliver Schmitz, Askin T Isikveren, and Mirko Hornung. Methodology for Sizing and Performance Assessment of Hybrid Energy Aircraft. *Journal of Aircraft*, 52(1):341–352, jan 2015. ISSN 0021-8669. doi: 10.2514/1.C032716. URL http://arc.aiaa.org/doi/10.2514/1.C032716.

[38] Daniel P. Raymer. Aircraft Design: A Conceptual Approach, 2004.

[39] Kevin Reynolds. Trajectory Optimization of a Battery-Powered Competition Aircraft. In *51st AIAA Aerospace Sciences Meeting including the New Horizons Forum and Aerospace Exposition*, number January, pages 1–15, Reston, Virigina, jan 2013. American Institute of Aeronautics and Astronautics. ISBN 978-1-62410-181-6. doi: 10.2514/6.2013-1155. URL http://arc.aiaa.org/doi/10.2514/6.2013-1155.

[40] Jan Roskam. *Airplane Design.* Roskam Aviation and Engineering Corporation, 1985.

[41] Rotax. Operators Manual For Rotax Engine Type 914 Series. Technical report, Rotax Aircraft Engines, 2015.

[42] K Schittkowski. Nlpql: a fortran subroutine solving constrained nonlinear programming problems. 5:485–500, 1985.

[43] Joachim Schoemann and Mirko Hornung. Modeling of Hybrid Electric Propulsion Systems for Small Unmanned Aerial Vehicles. In *12th AIAA Aviation Technology, Integration, and Operations (ATIO) Conference and 14th AIAA/ISSMO Multidisciplinary Analysis and Optimization Conference*, number September, pages 1–19, Reston, Virigina, sep 2012. American Institute of Aeronautics and Astronautics. ISBN 978-1-60086-930-3. doi: 10.2514/6.2012-5610. URL http://arc.aiaa.org/doi/10.2514/6.2012-5610.

[44] Siemens. Internal Document: Propulsion Systems Features, 2017.

[45] Egbert Torenbeek. *Synthesis of Subsonic Airplane Design.* 1976. ISBN 978-94-009-9582-6. doi: 10.1007/978-94-009-9580-2.

[46] UBER. UBER Elevate - Fast-Forwarding to a Future of On-Demand Urban Air Transportation. Technical report, 2016.

[47] Philippe Ulrich. Energy Storage Systems - Li-ion, 2015.

[48] UNFCCC. United Nations Climate Change (UNFCCC): Climate Change Threatens National Security Says Pentagon, 2014. URL https://unfccc.int/news/climate-change-threatens-national-security-says-pentagon.

[49] Caihao Weng, Jing Sun, and Huei Peng. A uni fi ed open-circuit-voltage model of lithium-ion batteries for state-of-charge estimation and state-of-health monitoring q. *Journal of Power Sources*, 258:228–237, 2014. ISSN 0378-7753. doi: 10.1016/j.jpowsour.2014.02.026. URL http://dx.doi.org/10.1016/j.jpowsour.2014.02.026.